Plate fin heat exchanger design optimization and mass-specific performance assessment for aerospace applications

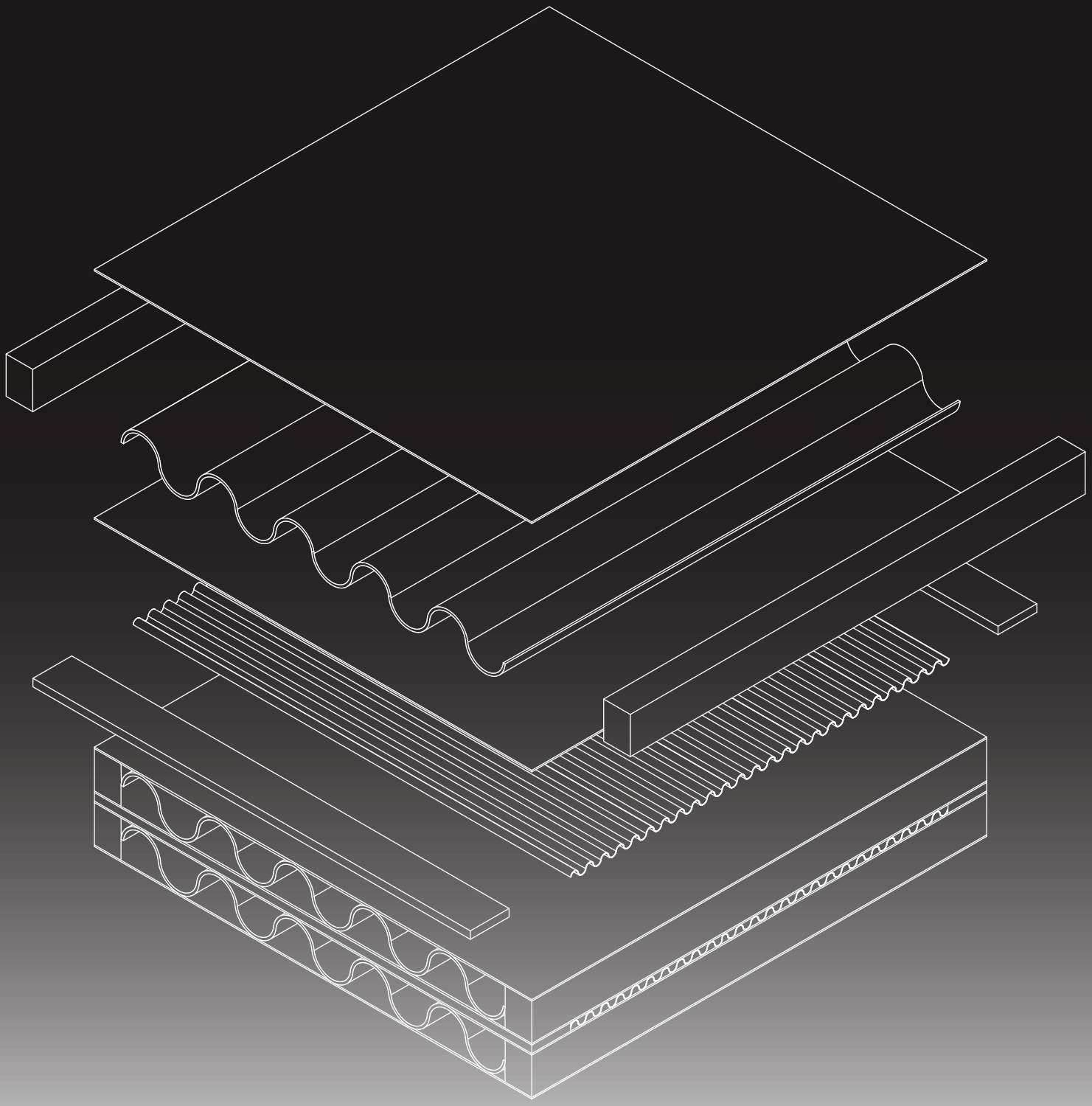

Andrea Baglieri

Politecnico di Torino

TU Delft

Politecnico di Torino

Politecnico di Torino

Thesis for the Master of Science degree in Aerospace Engineering

Plate fin heat exchanger design optimization and mass-specific performance assessment for aerospace applications

Supervisor:
Prof. Dario Pastrone (Politecnico di Torino)

Academic tutor:
Ir. Fabio Beltrame (TU Delft)

Author:
Andrea Baglieri
288789

M.Sc Thesis pursued at TECHNISCHE UNIVERSITEIT DELFT

Oct. 2022 - Mar. 2023

TU Delft

Abstract

Efficient heat exchanger design is crucial for cost, sustainability, and energy conservation. Due to its importance, the research interest in optimal HX design has increased across various industries, especially in the aerospace sector. Here, compact heat exchangers with a heat transfer area compactness $\beta > 400$ are of high interest, mainly the plate-fin ones. These topologies are characterized by vertically stacked plates that separate the two fluids, and several ducts in which many different fin geometries can be employed. Selecting the right fin type and its geometric parameters to use in each fluid side is a fundamental and complicated step. Although optimal HX selection and design have been relying on the expertise and past choices of experts, over the years, several methods have been proposed to compare the performance of different surface geometries. These performance valuation methods aim to help the designer make informed decisions about the optimal fin topology. In the aerospace sector, where the HX mass plays a key role, few design guidelines on optimal HX selection and design are present. For this reason, this work analyzes the mass-specific performance of optimally designed compact plate-fin HXs and defines general guidelines for the assessment of different optimal fin topologies.

Two models of plate-fin HXs in crossflow arrangement compatible with several fin geometries have been developed. The sizing determines the dimensions and pressure drops ΔP of the HX given the inlet conditions on both sides and the heat duty. While the rating determines the heat duty and pressure drops of a given HX. The models have been validated by comparing their predictions with those of test cases from the scientific literature. In order to obtain optimized maps of the HXs, four optimization algorithms have been implemented: the Particle Swarm Optimization (PSO) and the Differential Evolutionary Algorithm (DEA) are single-objective, while the NSGA-II and the NSGA-III are multi-objective algorithms. The objective function for the single objective algorithms is the exchanger mass, which needs to be minimized, while the objective function for the other two is to minimize the exchanger mass and the pressure drop on either just the cold side, or both. The single objective optimizations have been used to generate optimized design maps in two different ways: first by varying the heat duty $\dot{Q}$ and keeping constant all the constraints, and then by varying the constraint of the ΔP on the hot side at constant $\dot{Q}$. An air to air balanced HX (C^*=1) is chosen as a first case study. The optimization has been performed with three fin types, in order to compare their performances. The three fin surfaces adopted are the same for both fluid sides: the offset-strip fins, the louvered fins, and the triangular wavy fins. The mass-specific power $MSP = \dot{Q}/M_{hex}$, the ΔP, and the two Bejan numbers are chosen as performance metrics.

The MSP showed no clear trend with ΔP, but a trend with Bej was found. By decreasing the heat duty, the HX mass and the Bej both decrease following a $1/x^n$ trend. On the other hand, increasing the constraints on the ΔP_h, at constant heat duty, allows us to define some working ranges. The multi-objective optimization showed that by increasing the MSP, the ΔP_h increases as well, while, the ΔP_c does not follow a clear trend, and the Bej_c decreases. Finally, the three-objective optimization showed that, as expected, by increasing the allowed ΔP the designer can achieve significantly lower masses.

Acknowledgements

During six months at TU Delft Propulsion Power & Group I had the opportunity to work hard on this thesis. Developing this project in a very stimulating environment I explored new topics and improved in managing my work and in tackling new projects. It has been a very intensive and rewarding experience.
I want to thank Dr. Carlo Maria De Servi for accepting my request and for putting me in contact with my supervisor Fabio Beltrame: this work could not have been possible without his guidance and help.

This thesis represents not just the end of my experience at TU Delft but, mainly, the end of my long journey at the Polytechnic of Turin. These years have not been easy but the time spent at the Polito Sailing Team is one of the best experiences I had. I met a lot of great people and friends who have enabled me to improve myself as an engineer and, more importantly, as a person. Thanks to all of them.
I want to thank my long-time friends from Ragusa who always helped me with patience and by bringing joy into my life. A big thank you to my new friends in Turin as well, with whom I shared anxiety and fun. I would let know to my family in Ragusa that this goal is because of them too. A big hug to my aunts and uncles, my grandparents, and my cousins: you have always taken an interest in me and have supported me with affection and kindness.
I want to express my gratitude to my sister Martina who helped me to fix some images and to create my presentation. To my parents Enzo and Claudia, you helped me more than everyone else. Thank you for your support during these years. You and Martina embraced my tears and anxieties, guided me, and did not let me give up. Even if you did not understand the topics I was studying, you always wanted to help me with my exams and, in this thesis, there is also your contribution, Dad. You always believed in me, even when I did not. Thanks.

Finally, this thesis is for my zia Stefania. To you who have done so much for me. You listened to me and woke me up. You taught me to value only the beautiful things. Thank you for everything from the bottom of my heart, Atà.

Mura a siccu.

Andrea Baglieri,

October 2023

Contents

List of Figures

List of Tables

Nomenclature

$2A$	wavy amplitude	[m]
A	total heat transfer surface area on one side of an exchanger	[m^2]
A_0	minimum free flow area	[m^2]
A_f	fin/extended/secondary heat transfer surface area on one side of an exchanger	[m^2]
A_k	fin cross-sectional area for heat conduction	[m^2]
A_p	primary heat transfer surface area on one side of an exchanger	[m^2]
A_w	wall area	[m^2]
A_{fr}	frontal surface area on one side of an exchanger	[m^2]
C	flow stream heat capacity rate	[$W\,K^{-1}$]
C_{min}	minimum heat capacity	[$W\,K^{-1}$]
E	dissipated power of the fluid per unit area P/A	[$W\,m^{-2}$]
F_d	fin depth	[m]
F_h	fin height	[m]
F_p	fin pitch, has different definitions for different fin geometries (see Ch.2)	[m]
G	fluid mass velocity based on the minimum free area, $\dot{m}/A_0$	[$kg\,m^{-2}\,s^{-1}$]
L	flow length	[m^2]
L_l	louver length	[m]
L_p	louver pitch	[m]
L_α	louver angle	[°]
M	mass	[kg]
N_{LB}	number of louver banks	
N_p	number of passages	
P	flow-friction/dissipated power	[W]
P	fluid pressure	[Pa]
P_w	wetted perimeter	[m]

R	resistance	
Ra	ducts roughness	[m]
T	fluid temperature	[K]
T_p	tube pitch	[m]
U	overall heat transfer coefficient	$[\mathrm{W\,m^{-2}\,K^{-1}}]$
V	total volume of an heat exchanger	$[\mathrm{m^3}]$
V_p	volume between two plates on one fluid side	$[\mathrm{m^3}]$
$\dot{Q}$	heat duty/heat transfer rate of heat exchanger	[W]
$\dot{m}$	mass flow rate	$[\mathrm{kg\,s^{-1}}]$
c_p	specific heat of fluid at constant pressure	$[\mathrm{J\,kg^{-1}\,K^{-1}}]$
d_h	hydraulic diameter	[m]
f	Fanning friction factor	
h	heat transfer coefficient	$[\mathrm{W\,m^{-2}\,K^{-1}}]$
j	Colburn factor	
k	fluid thermal conductivity	$[\mathrm{W\,m^{-1}\,K^{-1}}]$
k_f	fin conductivity	$[\mathrm{W\,m^{-1}\,K^{-1}}]$
k_w	wall conductivity	$[\mathrm{W\,m^{-1}\,K^{-1}}]$
l	fin length for heat conduction from primary surface to midpoint between plates for symmetric heating	[m]
l_s	fin length (for offset-strip fins)	[m]
m	fin parameter	$[\mathrm{m^{-1}}]$
n_p	number of plates	
n_gen	maximum number of generations for optimization problem	
nv	number of optimum variables for optimization problem	
p	number of partitions for optimization problem with NSGA-III	
pop_size	population size of optimization problem	
s_f	fin spacing	[m]
t_f	fin thickness	[m]
t_w	thickness plate	[m]
u	fluid velocity	$[\mathrm{m\,s^{-1}}]$
x	hot stream fluid length, heat exchanger width	[m]
y	no-flow length, heat exchanger height	[m]

z	cold stream fluid length, heat exchanger length	[m]

Acronyms

AGF Area Goodness Factor

CR Crossover rate

DEA Differential Evolution Algorithm

HX heat exchanger

LF Louvered Fin

MR Mutation rate

MSP Mass-specific power $[kW/kg]$

NSGA-II Non Sorted Genetic Algorithm II

NSGA-III Non Sorted Genetic Algorithm III

OSF offset-strip Fin

PEC Performance Evaluation Criteria

PFHX Plate-fin Heat Exchanger

PSO Particle Swarm Optimization

RPF Rectangular Plain Fin

RWF Rectangula Wavy Fin

TPF Triangular Plain Fin

TWF Triangular Wavy Fin

VGF Volume Goodness Factor

Dimensionless Groups

C^* heat capacity ratio, $C_{\min}/C_{\max}$

NTU number of transfer units

Nu Nusselt number

Pe Peclet number

Pr Prandtl number

Re Reynolds number

St Stanton number

Greek Letter Symbols

α	compactness	$[\mathrm{m^2\,m^{-3}}]$
α_d	fluid thermal diffusivity	$[\mathrm{m^2\,s^{-1}}]$
β	heat transfer surface area density	$[\mathrm{m^2\,m^{-3}}]$

ϵ	effectiveness	
η_0	extended surface efficiency	
η_f	fin efficiency	
λ	wavelength	[m]
μ	fluid dynamic viscosity	[Pa s]
ν	fluid kinematic viscosity	[$\mathrm{m^2\,s}$]
ϕ	structure porosity	
ρ	fluid density	[$\mathrm{kg\,m^{-3}}$]
σ	ratio of free flow to frontal area	
τ_w	wall shear stress	[Pa]

Subscripts

1	fluid 1; one section (inlet or outlet) of the exchanger
2	fluid 2; other section (inlet or outlet) of the exchanger
b	bulk
c	cold-fluid side
diss	dissipated
f	fouling
h	hot-fluid side
hex	heat exchanger
i	inlet to the exchanger
m	mean
max	maximum
min	minimum
o	outlet to the exchanger
st	structure
std	arbitrarily selected standard temperature and pressure conditions
tot	total
w	properties at the wall temperature

Chapter 1

Introduction

Over the past century, the importance of heat exchanger design has increased significantly. The escalating concern for environmental and climate issues, coupled with the necessity to reduce production costs, has directed the industry's attention to designing smaller heat exchangers with superior performance. A heat exchanger has the purpose to transfer thermal energy between two fluids (gas or liquid) separated by heat transfer surfaces. The heat transfer takes place by convection[1] and gasses may have a heat transfer coefficient 10 to 50 times smaller than that of liquids [Stone, 1996]. The use of enhanced surfaces enables the reduction of the gas-side thermal resistance and, consequently, of the heat exchanger size. This category of heat exchangers is commonly referred to as compact heat exchangers. Compact heat exchangers are typically characterized by extended surfaces with a high area density β, which means a high ratio of heat transfer area over volume. It is crucial to emphasize that 'compact' and 'small' are not equivalent, as heat exchangers with high area density do not necessarily possess small mass and volume.
Compact heat exchangers can be grouped in multiple categories and one of the most important is the plate-fin heat exchanger. This work will focus only on the design of this category. Plate-fin heat exchangers have different geometry fins between parallel plates and sidebars along the outer edges (Fig.1.1).

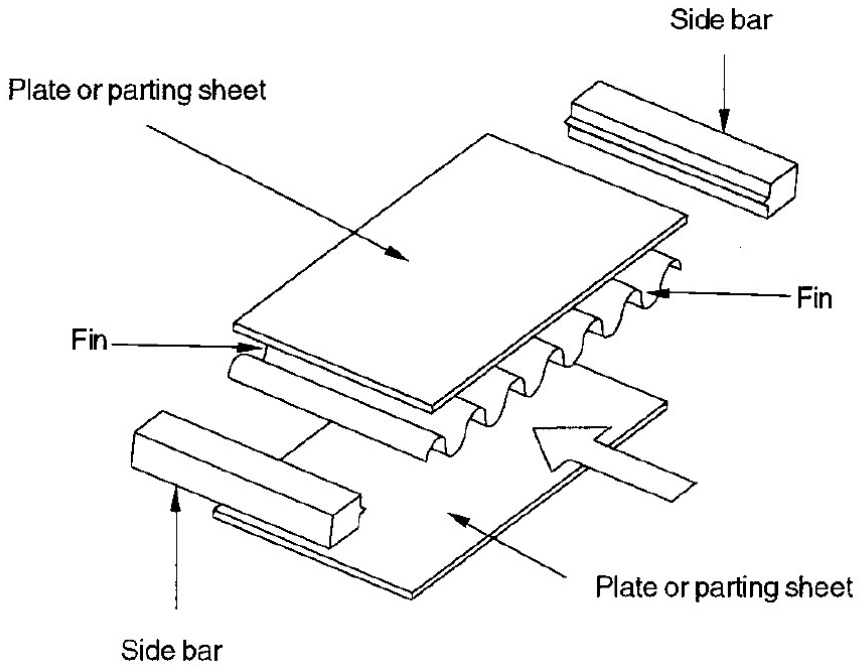

Figure 1.1: Basic components of a plate-fin heat exchanger. Taken from Shah and Webb [1983]

[1] According to Shah and Sekulić [2003], this category of the heat exchanger may be referred to as *recuperator*.

This type of heat exchanger can be categorized on flow arrangement. The initial differentiation is determined by the number of flow passes. In the case of a single-pass heat exchanger, fluids flow the entire length of a heat exchanger section only once. On the other hand, if the flow direction is reversed and fluid flows through an equal- or different-size section, it is considered to have made a second pass [Shah and Sekulić, 2003]. Consequently, such a heat exchanger is referred to as a multi-pass heat exchanger.
Conventionally, every pass can be characterized by a specific fluid path: counterflow, parallel-flow, and crossflow. The first operates with two fluids that flow in parallel but in opposite directions, while for the second the fluids flow in the same direction. Lastly, in a crossflow exchanger, the two fluid streams flow in directions perpendicular to each other.

A wide variety of fin geometries can be employed in the design of compact heat exchangers in order to improve their performance. The selection of optimal fin type is not trivial and is based on a trade-off between heat transfer improvement and pressure losses on both fluid sides. The present work will focus on defining some selection criteria for aerospace applications, in order to compare the performance improvement provided by the various geometries.

1.1 Performance assessment of compact heat exchangers

For many years, the process of selecting and designing heat exchangers relied heavily on the expertise and past choices of manufacturers. The determination of performance metrics, conditions, and initial assumptions, upon which the iterative process is based, necessitated the guidance of experienced professionals in the field. The challenges involved in heat exchanger design selection and sizing are far from simple, as they require the consideration of numerous variables and conditions while striving to strike a balance in performance. Several methods have been proposed to assess performance and compare the performance of heat exchanger geometries with the aim of helping the designer make an informed choice. These methodologies for performance assessment are called Performance Evaluation Criteria (PEC) and are discussed below.

The Colburn factor j and fanning friction factor f are key parameters in heat exchanger design and are strongly employed in defining performance criteria for surface selection, as shown below.
The f factor is defined as the ratio of wall shear stress τ_w to the flow kinetic energy per unit volume and quantifies the frictional component of the pressure drop. In other words, the f factor characterizes the resistance to fluid flow within heat exchanger.

$$f = \frac{\tau_w}{\rho \; {u_m}^2/2} \tag{1.1}$$

The friction factor depends on the flow regimes and on the flow passage geometry: the flow passage geometry influences strongly in a laminar flow and weakly in a turbulent flow. Moreover, the friction factor can also depend on fluid properties, phase conditions, and plate structural properties.
The j factor, on the other hand, represents the convective heat transfer performance of the heat exchanger. It relates the heat transfer coefficient to the fluid flow characteristics, taking into account the convective heat transfer enhancement due to the geometry and surface properties of the heat exchanger. Therefore, this parameter may be defined as a modified Stanton number St to take into account the moderate variations in the Prandtl number Pr in turbulent flow and, for this, is defined as

$$j = St \; Pr^{2/3} = \frac{Nu \; Pr^{-1/3}}{Re}. \tag{1.2}$$

The Stanton number St represents the ratio of convectional heat transferred to the thermal capacity of the fluid and is defined as $St = h/Gc_{\mathrm{p}}$. The Nusselt number Nu represents the ratio of convective to conductive heat transfer and is expressed as $Nu = h/lk$, where h denotes the convective heat transfer coefficient, l represents the characteristic length, and k is the thermal conductivity of the fluid. Lastly, the Prandtl number Pr represents the ratio of fluid kinematic viscosity to thermal

diffusivity of the fluid $Pr = \nu/\alpha_{\mathrm{d}}$. However, these three quantities can be related to each other and the Stanton number can be expressed as a function of Nu, Pr, and Re as follows:

$$St = \frac{h}{G\ c_{\mathrm{p}}} = \frac{Nu}{Re\ Pr}. \tag{1.3}$$

Using this last relation, it is possible to express the j factor as shown in Eq.1.2.

As depicted above, the j and f factors are helpful in defining the thermal characteristics of the HX, but the study of these factors alone is not enough to compare the final HX performance. Over the years, several methods for the evaluation of new performance criteria have been developed, here the main approaches will be presented highlighting their advantages and drawbacks.

1.1.1 j-f VS Re curves

The first method for the design selection proposed here involves the utilization of j and f curves plotted against the Reynolds number Re. In their work, Kays and London [2018] provided numerous $j-f$ versus Re plots for various enhanced surfaces (Fig.1.2). However, these curves do not represent an effective tool for the assessment of the performance of the geometry when employed in a heat exchanger, as they are insufficient for determining the heat exchanger size or weight as well as the pressure drop. Moreover, the curves exhibit a wide range of magnitudes and slopes, making it challenging to compare different geometries against each other.

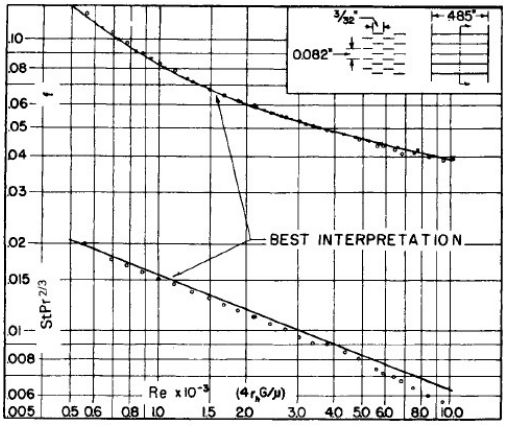

Fin pitch = 12.22 per in = 480 per m
Plate spacing, b = 0.485 in = 12.3 x 10^{-3} m
Fin length = 0.094 in = 2.4 x 10^{-3} m
Fins staggered symmetrically
Flow passage hydraulic diameter, $4r_h$ = 0.01120 ft = 3.41 x 10^{-3} m
Fin metal thickness = 0.004 in, copper = 0.102 x 10^{-3} m
Total heat transfer area/volume between plates, β = 340 ft^2/ft^3 = 1,115 m^2/m^3
Fin area/total area = 0.862

(a)

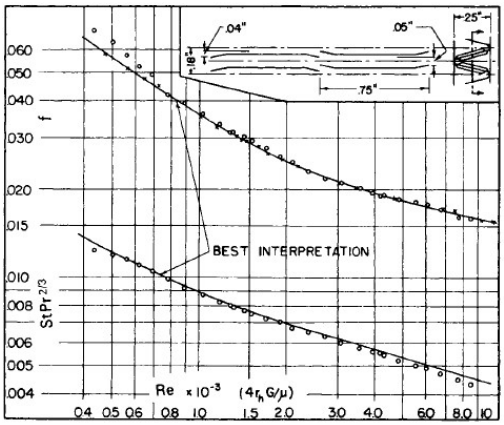

Fin pitch = 11.1 per in = 437 per m
Plate spacing, b = 0.250 in = 6.35 x 10^{-3} m
Louver spacing = 0.55 in = 19.05 x 10^{-3} m
Fin gap = 0.05 in = 1.27 x 10^{-3} m
Louver gap = 0.04 in = 1.02 x 10^{-3} m
Flow passage hydraulic diameter, $4r_h$ = 0.01012 ft = 3.084 x 10^{-3} m
Fin metal thickness = 0.006 in, aluminum = 0.152 x 10^{-3} m
Total heat transfer area/volume between plates, β = 367 ft^2/ft^3 = 1,204 m^2/m^3
Fin area/total area = 0.756

(b)

Figure 1.2: Example plots of j and f curves vs. Re for (a) offset-strip fins, (b) Triangular louvered fins. Taken from Kays and London [2018]

1.1.2 Area Goodness Factor comparison

The failure of the previous method led to the development of a comparison method based on the area goodness factor [Shah and Sekulić, 2003]. The Area Goodness Factor (AGF) is defined as the ratio of j over f and, in order to compare different enhanced surfaces, is plotted versus the Re number. The AGF can be write following Eq.1.2, as:

$$AGF = \frac{j}{f} = \frac{Nu\ Pr^{-1/3}}{f\ Re}. \tag{1.4}$$

Then, this equation can be rearranged in order to show all the parameters that influence this factor. The friction factor plays an important role in pressure drop evaluation:

$$\Delta P = \frac{G^2\ 4\ f\ L}{2\ \rho\ d_\mathrm{h}\ \rho}$$

where the hydraulic diameter is $d_\mathrm{h} = \frac{4\ A_0\ L}{A}$ and $G = \frac{\dot{m}}{A_0}$. These two definitions can be replaced into the ΔP formula that enables to definition of the friction factor. Then, the f factor equation is replaced in Eq.1.4:

$$AGF = \frac{Nu\ Pr^{-1/3}}{Re}\frac{\dot{m}^2\ A}{2\ \Delta P\ A_0^3\ \rho}. \tag{1.5}$$

The heat transfer area is defined as $A = \frac{NTU\ \dot{m}\ c_\mathrm{p}}{h\ \eta_0}$, the Nusselt number as $Nu = \frac{h\ d_\mathrm{h}}{k}$ and, since $G = \frac{Re\ \mu}{d_\mathrm{h}} = \frac{\dot{m}}{A_0}$, the AGF can be rewritten as

$$AGF = \frac{\dot{m}^2\ NTU}{2\ \Delta\ P\ A_0^2\ \rho\ \eta_0}\frac{\mu\ c_\mathrm{p}\ Pr^{-1/3}}{k}.$$

Finally keeping into account that $Pr = \frac{\mu\ c_\mathrm{p}}{k}$, Eq.1.4 can be rearranged as:

$$AGF = \frac{1}{A_0^2\ \eta_0}\left[\frac{Pr^{2/3}\ NTU\ \dot{m}^2}{2\ \rho\ \Delta P}\right] \tag{1.6}$$

The enclosed in parentheses in Eq.1.6 are strongly dependant by the the operational parameters. Consequently, the Area Goodness Factor is not dependent on geometric parameters (d_h or β) and is inversely proportional to the square of the free-flow A_0. This means that, by keeping the pressure drop and the NTU constant, a greater AGF is desirable as it implies a lower free-flow area and, hence, a lower frontal area. Differently, with a constant pressure drop and a constant free-flow area, a lower AGF is better since a small NTU value means a small heat transfer area and, thus, a lower frontal area. Nevertheless, the AGF alone still does not provide information about dissipated power and detailed fin geometry.

1.1.3 Volume Goodness Factor comparison

The inference of HX volume cannot be derived through the application of the area goodness factor comparison. Consequently, an alternative method called the volume goodness factor (VGF) approach has been developed [Shah and Sekulić, 2003]. This method enables two distinct types of comparisons:

$$h_\mathrm{std} \text{ vs } E_\mathrm{std} \qquad \text{and} \qquad \eta_0 h_\mathrm{std}\beta \text{ vs } E_\mathrm{std}\beta.$$

Here the heat transfer coefficient h and the fluid pumping power per unit area E are defined as follows:

$$h = \left(\frac{c_\mathrm{p}\ \mu}{Pr^{2/3}\ d_\mathrm{h}}\right) j\ Re, \tag{1.7}$$

$$E = \frac{P}{A} = \left(\frac{\mu^3}{2\ \rho^2\ d_\mathrm{h}^3}\right) f\ Re^3. \tag{1.8}$$

In both comparisons, in order to find the geometry with the minimum volume, it is supposed that the surfaces exhibit identical thermal performance. Therefore, the values for the heat duty, pressure drop, the temperature difference between the wall and the fluid, and fluid flow rate are kept constant. The plotting h_std vs E_std disregards the extended surface ($\eta_0 = 1$) while maintaining the same values for E, area density β, and the ratio of free flow to frontal area σ. Thus, since

$$\dot{Q} = \eta_0 h \beta V\left(T_\mathrm{w} - T_\mathrm{m}\right), \tag{1.9}$$

the heat transfer coefficient is inversely proportional to the HX volume. A higher position on the plot, corresponds to a lower value of the core volume, indicating a more favorable or desirable geometry.
On the other hand, the $\eta_0 h_{\text{std}}\beta$ vs $E_{\text{std}}\beta$ comparison takes into account the effect of extended surface in heat exchangers by considering the η_0. In this context, the term $\eta_0 h_{\text{std}}\beta$ represents the heat transfer power per unit temperature difference and unit core volume, meanwhile, $E_{\text{std}}\beta$ is the friction power per unit core volume [Shah and Sekulić, 2003]. The equations for these quantities are as follows:

$$\eta_0 h_{\text{std}}\beta = \left(\frac{c_{\text{p}}\ \mu}{Pr^{2/3}}\eta_0\frac{4\sigma}{d_{\text{h}}^2}\right) j\ Re, \tag{1.10}$$

$$E_{\text{std}}\beta = \left(\frac{4\mu^3\ \sigma}{2\rho^2\ d_{\text{h}}^4}\right) f\ Re^3. \tag{1.11}$$

Consequently, for Eq.1.9, it is evident that $\eta_0 h_{\text{std}}\beta \propto 1/V$, implying that the optimal point for the HX volume is attained with higher values of $\eta_0 h_{\text{std}}\beta$ while maintaining $E_{\text{std}}\beta$ constant. One limitation of this method is the requirement to fix a specific set of fluid properties for a valid comparison and this restricts the applicability of the method to specific operating conditions. Nonetheless, the use of these goodness factors can still offer valuable insights and preliminary information for comparing the performance of different surfaces.

1.1.4 Fixed geometry, fixed flow area, and variable geometry criteria

Webb [1981] proposed a comparison method based on different parameters, which are used to assess the thermal performance without taking into account the flow losses. The design objectives to reach in this study are:

1. minimum heat transfer area for equal pumping power P and heat duty $\dot{Q}$;
2. higher UA for equal pumping power P and fixed flow length;
3. lower pumping power P for equal heat transfer rate $\dot{Q}$ and flow length.

"A PEC is established by selecting one of the operating variables for the performance objective subject to design constraints on the remaining variables" [Shah and Sekulić, 2003] and is defined as a ratio comparing the same variable of different heat transfer surfaces. The operating variables include geometry (flow length), mass flow rate $\dot{m}$, fluid pumping power P, heat duty $\dot{Q}$, and fluid inlet temperature difference ΔT_{max}.
The methods are categorized into Fixed Geometry (FG), Fixed flow area (FN), and Variable Geometry (VG) based on the design objectives. For fixed-geometry criteria, a plain surface is compared with an enhanced surface of the same length, which reaches a higher heat transfer rate and pumping power. For criteria with fixed flow area, the pumping power P is reduced while maintaining constant $\dot{Q}$ and $\dot{m}$, or the $\dot{m}$ is reduced keeping constant P and $\dot{Q}$. For variable-geometry criteria, the heat transfer surface is reduced and the frontal area is increased for fixed $\dot{m}$, P, and $\dot{Q}$.
The advantages of this comparison method are threefold: first, the designer can choose his or her own criteria for comparison, second, the opportunity to compare the performance of a surface with that of a reference surface, and third, does not need to evaluate fluid properties as they are not considered. The disadvantages, on the other hand, are that, according to the criteria selected, several key variables must be kept constant. Given that several variables must be kept constant, as has been highlighted before, it can be difficult to study the mutual interaction of these parameters.

1.1.5 Heat transfer and pumping power factors

The methods proposed by LaHaye et al. [1974] and Soland [1975] aimed to overcome the limitations of previous methods for evaluating heat transfer performance in terms of heat transfer coefficient

and pumping power.
LaHaye et al. [1974] introduced two new factors, the heat transfer performance factor $J = j\ Re$ and the pumping power factor $F = f\ Re^3$, defined respectively as follows:

$$J = h\frac{Pr^{2/3}\ d_\mathrm{h}}{c_\mathrm{p}\ \mu} = j\ Re, \tag{1.12}$$

$$F = \frac{P}{V}\frac{2\ \rho^2 d_\mathrm{h}^3}{\beta\ \mu^3} = f\ Re^3. \tag{1.13}$$

By plotting these factors against each other, clear trends of the curves can be observed, allowing for a comparative analysis of different surfaces. However, this method does not consider the influence of fin thickness and thermal conductivity and, for this reason, should be used only as "an approximate presentation which guides the designer in the vicinity of optimum solutions" [LaHaye et al., 1974].

Soland [1975] extended the previous method by studying $\frac{NTU}{V}$, which represents the heat transfer rate per unit volume, and the pumping power per unit volume $\frac{P}{V}$ as performance parameters. In particular

$$\frac{NTU}{V} = \frac{h\ A}{V} = \frac{4\ \mu\ j\ Re}{Pr^{2/3}\ \dot{m}\ d_\mathrm{h}^2}, \tag{1.14}$$

while the pumping power per unit volume is expressed as

$$\frac{P}{V} = \frac{\dot{m}\ \Delta P}{\rho V} = \frac{2\mu^3\ f\ Re^3}{\rho^2\ d_\mathrm{h}^4}. \tag{1.15}$$

This comparison method is made by keeping the mass flow rate and the two inlet temperatures constant and using the same fluid also c_p, μ, and Pr are constant. Thus, the performance parameters proportional to Eq.1.14 and 1.15 are defined as

$$\frac{j\ Re}{d_\mathrm{h}^2} \qquad \text{and} \qquad \frac{f\ Re^3}{d_\mathrm{h}^4}.$$

These parameters are plotted against each other and four different comparisons can be made, with the following conditions:

a. same heat exchanger shape and volume;

b. same heat exchanger volume and pumping power;

c. same pumping power and number of transfer units;

d. same volume and number of transfer units.

The advantage of this approach is that it allows for a relative comparison between surfaces with different nominal diameters. However, it still lacks the inclusion of fin efficiency.

1.1.6 Energy, mass and volume efficiency

In a study published by Fugmann et al. [2019], a method was presented to establish a connection between thermal performance and energy, volume, and mass considerations. The key figures introduced in this method do not rely on a characteristic length, enabling a straightforward comparison among different heat transfer surfaces. It is worth noting that Fugmann et al. [2019] concentrated their investigation on a single fluid side and imposed certain constraints on the performance evaluation:

1. the same heat transfer fluids ;

2. the same mean fluid temperatures T_m and pressures P_m;
3. the same mass flow rates $\dot{m}$;
4. the same heat transfer rates $\dot{Q}$;
5. the same small thermal resistances on the second fluid side.

The heat duty $\dot{Q}$ can be expressed as

$$\dot{Q} = \eta_0 \; h \; A \; \Delta T_\mathrm{m} \tag{1.16}$$

and, for the given restrictions, ΔT_m is constant allowing for the comparison of different HX at the same $\eta_0 \; h \; A$, instead of $\dot{Q}$. This term is defined as benefit of the heat transfer process and is related to different design costs:

- dissipated power P_diss;
- structure volume V_st;
- structure mass M_st.

The P_diss is defined as $P_\mathrm{diss} = \Delta P \; \dot{V}_\mathrm{air,st}$ and is proportional to the electric power consumption P_el, meanwhile the V_st is equal to the product of the frontal area A_fr and the structure length L_st. However, the dimensional key figures which relate the benefit to different performances are:

- energy efficiency $\epsilon_\mathrm{E} = \frac{\eta_0 \; h \; A}{\Delta P \; \dot{V}_\mathrm{air,st}} = \frac{\dot{Q}}{P_\mathrm{diss} \; \Delta T_\mathrm{m}}$;
- volume efficiency $\epsilon_\mathrm{V} = \frac{\eta_0 \; h \; A}{V_\mathrm{st}} = \frac{\dot{Q}}{V_\mathrm{st} \; \Delta T_\mathrm{m}}$;
- mass efficiency $\epsilon_\mathrm{M} = \frac{\eta_0 \; h \; A}{M_\mathrm{st}} = \frac{\dot{Q}}{M_\mathrm{st} \; \Delta T_\mathrm{m}}$.

These dimensional criteria are limited by the assumption (1) to (5), which may be difficult to achieve during measurements. Therefore, non-dimensional key figures have been defined to allow for a better comparison, even though they have less accessible outputs. The definition of the non-dimensional key figures is based on viewing the term $\epsilon \Delta T_\mathrm{m}$ as the product of the driving parameter F_driving and the dimensionless efficiency ϵ^*. Using the Buckingham π theorem, the driving parameter can generally be expressed as:

$$F_\mathrm{driving} = 1/Br, \tag{1.17}$$

where Br is the Brinkman number which defines the ratio of the viscous dissipation power over the heat transfer by conduction. The driving force is different for the different dimensionless efficiency ϵ^*, and they are shown in Tab.1.1 with the corresponding efficiency expressions.

Key Figure	F_driving	**Definition**	**Reduced Expression**
Energy efficiency ϵ^*_E	$\frac{k_\mathrm{air} \; \Delta T_\mathrm{m}}{\mu_\mathrm{air} \; \nu^2_\mathrm{st}}$	$\frac{\dot{Q}}{P_{diss}} \frac{k_\mathrm{air} \; \Delta T_\mathrm{m}}{\mu_\mathrm{air} \; \nu^2_\mathrm{st}}$	$\frac{Nu \; \eta_0 \; d_\mathrm{h} \; \beta}{2 \; f \; Re}$
Volume efficiency ϵ^*_V	$\frac{\nu^2_\mathrm{st} \; k_\mathrm{air} \; \Delta T_\mathrm{m}}{\nu^2_\mathrm{air}}$	$\frac{\dot{Q}}{V_\mathrm{st}} \frac{\nu^2_\mathrm{st} \; k_\mathrm{air} \; \Delta T_\mathrm{m}}{\nu^2_\mathrm{air}}$	$\frac{Nu \; \eta_0 \; d_\mathrm{h} \; \beta}{Re^2}$
Mass efficiency ϵ^*_M	$\frac{\nu^2_\mathrm{st} \; k_\mathrm{air} \; \Delta T_\mathrm{m}}{\nu^2_\mathrm{air} \; \rho_\mathrm{air}}$	$\frac{\dot{Q}}{m_\mathrm{st}} \frac{\nu^2_\mathrm{st} \; k_\mathrm{air} \; \Delta T_\mathrm{m}}{\nu^2_\mathrm{air} \; \rho_\mathrm{air}}$	$\frac{Nu \; \eta_0 \; d_\mathrm{h} \; \beta \; \rho_\mathrm{air}}{Re^2 \; \rho_\mathrm{st}(1-\phi_s t)}$

Table 1.1: Non-dimensional key figures for extended performance evaluation

It can be seen that the three key efficiencies ϵ^* depend on the Reynolds number Re, on the thermal conductivities, on the Prandtl number Pr and the mass efficiency ϵ^*_M is dependent on the densities. Moreover, it is important to highlight that the three non-dimensional efficiencies have been generated without the restrictions (1) to (5), but the comparison has to keep these assumptions into account.

Based on the performance parameters outlined by Fugmann et al. [2019] it is possible to generate efficiency curves that establish the connection between key efficiencies and the Reynolds number Re: a higher value of ϵ^* denotes a low cost in terms of energy, volume, or mass (while maintaining the same $\dot{Q}$). These curves enable the comparison of multiple heat exchangers equipped with different types of fins, helping identify the optimal choice at equivalent Reynolds numbers. Furthermore, it is also feasible to create comparative maps for two distinct efficiencies, while specifying the Reynolds number. In both scenarios, selecting the most suitable surface requires striking a balance between various performance factors.

This study presents a valuable approach for conducting a comprehensive comparison of heat exchangers. However, it should be noted that this approach solely compares the performances of one fluid side, without considering the mutual interaction with the other fluid side. This means that the optimum surface selected by this method, for one fluid side, may not be optimum in a heat exchanger. Nevertheless, the method proposed by Fugmann et al. [2019] remains a valid tool for the preliminary design of a heat exchanger, providing detailed insights into the relationship between efficiencies.

1.2 Scope of this work

In order to identify the most suitable surface for a specific application, it is essential to have a reliable and effective method for comparison. Over the years, various methods have been proposed and discussed, some of which have been outlined in the preceding section. These traditional Performance Evaluation criteria (PEC) have several limitations that are highlighted when the designer needs to choose optimal geometries on both sides of the heat exchanger, with minimal pressure drops and minimum weight. These methods compare performance parameters, such as the j and f factor, that do not fully reflect the pressure losses, strongly influenced by the flow length. Furthermore, all of these methods provide information about the performances of just one fluid side, meanwhile, a good surface comparison needs to study the behaviour of both fluid sides to understand how they work together. The optimal outcomes achieved for the two individual fluid sides studied separately, may not necessarily be the optimum for a heat exchanger. This is because the mutual interaction between both sides may give different results. The PEC have also other drawbacks to overcome. The curves of j-f versus Reynolds for a fin surface change according to its sizes. The methods based on the AGF and the VGF need to fix the pressure drop and a set of fluid properties, in order to evaluate the sizes of the exchanger. Then, the method proposed by Webb [1981] compares different fin surfaces keeping constant some key parameters (according to the criteria selected), such as outlined above in the section 1.1.4. Lastly, the methods studied by LaHaye et al. [1974], Soland [1975], and Fugmann et al. [2019] adopt several constraints.

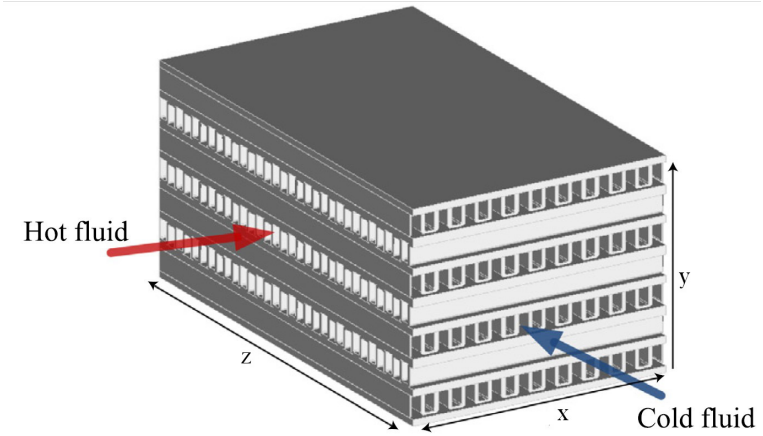

Figure 1.3: Typical plate-fin heat exchangers (PFHX), single-pass with crossflow and offset-strip fins. Adapted from Khan and Li [2017]

In order to facilitate the design process of compact heat exchangers, this work presents a new performance comparison methodology. This approach facilitates the comparison of multiple fin types, studying the behaviour of both fluid sides. Consequently, through the method studied here, it is possible to analyze different fin combinations in order to select the optimal surfaces to have the lightest exchanger with the lowest possible losses. Thus, the aim of the design of a compact heat exchanger is to achieve a trade-off between low mass and minimal pressure drop. This research aims to achieve the following objectives:

- Development and verification of a sizing tool that evaluates the heat exchanger mass M_{hex} and pressure drops ΔP, using as input the mean Reynolds numbers on both fluid sides;
- Definition of new performance metrics for exchanger mass and pressure drops, that facilitate the comparison of different fin geometries;
- Construction of optimized design maps that test the defined performance assessment methodology.

To achieve the objectives of this study, the following steps will be undertaken:

1. modeling of fin geometries: each fin type will be thoroughly analyzed by establishing their respective j and f correlations as well as their geometry equations (Ch.2);
2. verification of equations and correlations: the equations and correlations developed in step 1 will be validated by comparing them against experimental results reported in the relevant literature (Ch.2.5);
3. design approach implementation: a comprehensive design approach (Ch.3) including rating (Ch.4.1) and sizing (Ch.5.1) will be formulated and implemented as tools in a Python code specifically developed for recuperator design. The results obtained from these tools will be validated (Chs.4.2, and 5.2) by comparing them with similar test cases from the scientific literature and the commercial software *EchTherm* by Greth;
4. implementation of multiple optimization algorithms: various optimization algorithms (single, multi, and many objectives) will be presented and integrated into the design tool (Ch.6.1);
5. application of optimization algorithms: the optimization algorithms will be applied to an air-air, balanced ($C^* = 1$) test case, comparing three different fin combinations (offset-strip fins - offset-strip fins, louvered fins - louvered fins, triangular wavy fins - triangular wavy fins), in order to generate design-optimized maps (Ch.6.3);

6. analysis of the final maps: the resulting design-optimized maps will be examined, and their trends will be enlightened. The obtained results will provide insights into the behavior of performance factors and, consequently, guide the selection of the optimal fin geometry (Ch.7).

The design method used in this study is specifically focused on single-pass plate-fin heat exchangers (PFHX) with crossflow arrangement (see Fig.1.3). More in detail, the optimized trends of the performance metrics for the three fin combinations adopted in the test case of step 5 have been plotted. The obtained optimal design maps are specific to the chosen test case, though the trends of the overall performance can be extrapolated to HXs operating in similar conditions. In order to apply the proposed performance evaluation method, it is necessary to generate optimized design maps for the types of HXs that the designer needs to investigate.

Chapter 2

Modeling of finned geometries

The configuration of plate-fin heat exchangers (PFHX) has been introduced in Ch.1, emphasizing the crucial role of finned channels in enhancing heat transfer. As mentioned earlier, different fin geometries exhibit different performances. This study aims to investigate and analyze the following fin types, shown in Fig.2.1:

1. Plain Fins (PF)
2. Wavy Fins (WF)
3. Offset-strip Fins (OSF)
4. Louvered Fins (LF).

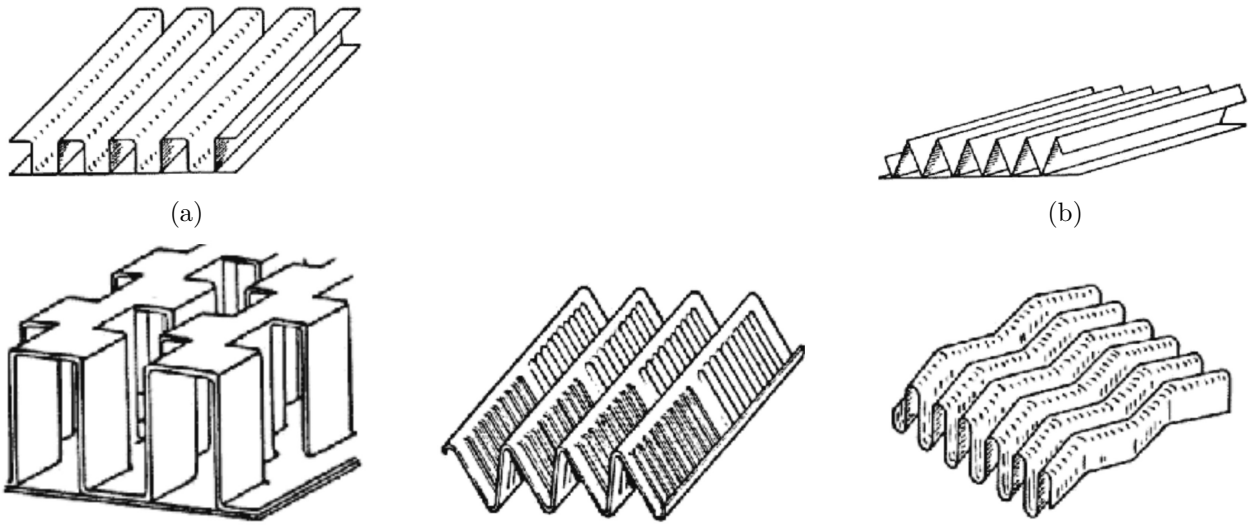

Figure 2.1: Types of enhanced surface: (a) Rectangular Plain Fin RPF, (b) Triangular Plain Fin TPF, (c) offset-strip Fin OSF, (d) Triangular Louvered Fins TCLF, (e) Wavy Fin WF. Taken from Webb and Kim [2005]

Each fin type will be modeled, and the equations defining their respective geometric surfaces will be developed. Furthermore, j and f correlations (see Ch.1) specific to each fin type, obtained from existing literature, will be presented. The fin geometry is characterized by multiple geometric features and specific parameters. Prior to assessing the geometric equations, it is essential to introduce the following surface areas:

- the primary heat transfer area A_p is the area of the channel that directly transfer the heat from one fluid to the other;
- the extended heat transfer area A_f is the surface area of the fins which are added to the channels and transfer the heat;
- the total heat transfer area A is the sum of the A_p and A_f and represent the total area that exchanges the heat;
- the minimum free flow area A_0 is the free flow area of a single passage of the fin;
- the frontal area A_fr refers to the cross-sectional area of the fin assembly.

To analyze a specific fin type, it is necessary to evaluate two surface-specific key parameters which define the geometry: the hydraulic diameter d_h and the heat transfer surface area density β. The hydraulic diameter d_h represents the equivalent diameter of circular tubes that would yield similar flow characteristics, and it is defined as

$$d_\mathrm{h} = \frac{4\ A_0\ L}{A} = \frac{4\ A_0}{P_\mathrm{w}}, \tag{2.1}$$

where P_w is the wetted perimeter. The heat transfer surface area density β is defined as the ratio between the total heat transfer area and the total volume between plates

$$\beta = \frac{A}{V_\mathrm{p}}, \tag{2.2}$$

where V_p is the total volume between two plates. These two surface-specific key parameters play a significant role in defining the fin geometry, for example, they are employed to evaluate other geometric parameters such as the compactness α and the ratio of free flow to frontal area σ. Furthermore, the hydraulic diameter d_h will be used in certain flow correlations.
The compactness α is defined as the ratio of the total heat transfer area on one fluid side to the total volume of a heat exchanger $\alpha = A/V$, meanwhile, the σ ratio is calculated as $\sigma = A_0/A_\mathrm{fr}$. According to Shah and Sekulić [2003], there are general relationships that connect these three parameters β, α, and σ. By developing the equation of volume of passages, and through the definition of hydraulic diameter (Eq. 2.1) and of β (Eq. 2.2), it has been determined that

$$\sigma_1 = \frac{A_{0,1}}{A_{fr,1}} = \frac{F_{h,1}\ \beta_1\ d_{h,1}/4}{F_{h,1} + F_{h,2} + 2t_\mathrm{w}}. \tag{2.3}$$

Here subscript 1 refers to one fluid side, meanwhile, subscript 2 refers to the other one, and the σ_2 is defined similarly. Furthermore, by examining the equation for the compactness α, a general relationship with σ and, thus, with β, can be established:

$$\alpha = \frac{A}{V} = \frac{A}{L\ A_\mathrm{fr}} = \frac{4A_0/d_\mathrm{h}}{A_\mathrm{fr}} = \frac{4\sigma}{d_\mathrm{h}}. \tag{2.4}$$

To evaluate all the specific key parameters mentioned above, it is necessary to know the geometrical characteristics that define the unit element [1] of each fin type. Each fin type has a unit element that is different from that one of the other geometries and, sometimes, is also defined by different parameters.

[1] In the context of this work, the term 'unit element' refers to the fundamental building block that defines a particular fin type. By replicating this unit element across the width and length of the channel, the overall geometry of the channel is established.

2.1 Plain Fins

One of the simplest geometries is the plain fins. These fins are made of uninterrupted channels that possess different cross-sections. In these configurations, the flow can progress and evolve smoothly, but this does not facilitate heat transfer enhancement, even though the presence of fins increases the heat transfer surface area. The geometric characteristics that define these geometries are outlined in the following table:

Geometrical characteristics	
t_f	fin thickness
F_p	fin pitch
F_h	plate spacing
s_f	fin spacing
h	fin height

Table 2.1: Geometrical characteristics of PF.

It is worth noting that these geometries lack a characteristic length, so all geometric parameters are calculated per unit length.

2.1.1 Rectangular Plain Fins

The Rectangular Plain Fins (RPF) are uninterrupted channels with a rectangular cross-section (see Fig.2.2). In the case of RPF, the unit element considered is two F_p wide. The following geometrical characteristics are evaluated by the geometric parameters of Tab.2.1:

$$A_0 = 2\ h\ s_\mathrm{f}, \tag{2.5}$$

$$A_\mathrm{p} = 2 s_\mathrm{f}, \tag{2.6}$$

$$A_\mathrm{f} = 4h + 2 s_\mathrm{f}, \tag{2.7}$$

$$V_\mathrm{p} = 2\ F_\mathrm{h}\ F_\mathrm{p}. \tag{2.8}$$

The key parameters d_h and β can be evaluated replacing the equations above (Eqs. 2.5-2.8) in Eq.2.1 and Eq.2.2.

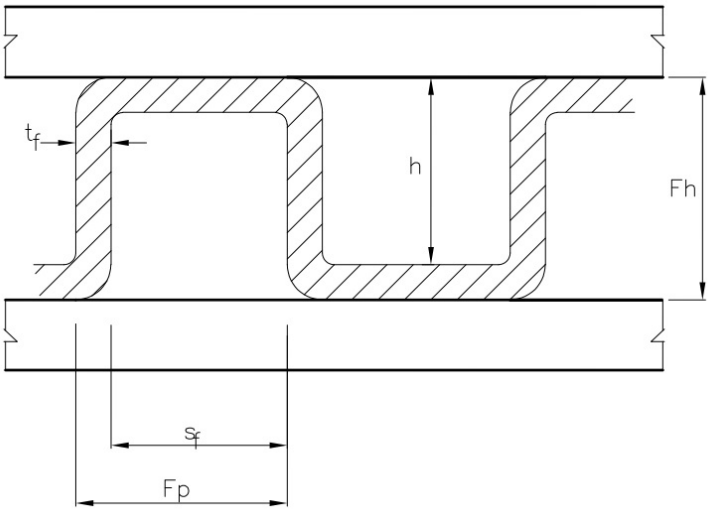

Figure 2.2: Typical geometry of rectangular plain fin and its geometric parameters

Then, several j and f correlations have been developed for the RPF.
Gnielinski [2010] proposed three Nu correlations for three different flow regimes described by the Reynolds number Re.

Laminar regime $Re \leq 2300$

$$Nu_{\text{lam}} = \left(Nu_1^3 + (Nu_2 - 1)^3 + Nu_3^3\right)^{\frac{1}{3}} \tag{2.9}$$

- Hydrodynamically and thermally developing

$$Nu_1 = 0.462 Pr^{\frac{1}{3}} \sqrt{\frac{Re\ d_{\text{h}}}{x}} \tag{2.10}$$

- Hydrodynamically developed and thermally developing

$$Nu_2 = 1.302 \left(\frac{Re\ Pr\ d_{\text{h}}}{x}\right)^{\frac{1}{3}} \tag{2.11}$$

- Hydrodynamically and thermally developed

$$Nu_3 = 4.354 \tag{2.12}$$

where x is the characteristic length considered.

Turbulent regime $Re \geq 10000$

$$Nu_{\text{turb}} = \frac{(\xi/8)\, Re\ Pr}{1 + 12.7\sqrt{(\xi/8)}\left(Pr^{\frac{2}{3}} - 1\right)} \left[1 + \frac{\left(\frac{d_{\text{h}}}{x}\right)^{\frac{2}{3}}}{3}\right] \tag{2.13}$$

where

$$\xi = \left(1.8 \log_{10}(Re) - 1.5\right)^{-2}.$$

Transition regime $2300 \leq Re \leq 10000$

$$Nu_{\text{trans}} = (1 - \gamma)\, Nu_{\text{lam},2300} + \gamma\ Nu_{\text{turb},10^4} \tag{2.14}$$

with

$$\gamma = \frac{Re - 2300}{10^4 - 2300}.$$

It is important to note the presence of the term d_{h}/x which represents the entrance effect. The typical values of d_{h}/x, for aerospace applications, are sufficiently low (around 10^{-3}) and this effect is negligible. With this assumption, the flow is considered fully developed, and the error introduced is minimal [Shah and Sekulić, 2003] if

$$L/d_{\text{h}} > 0.2 RePr.$$

Once the Nusselt number Nu has been evaluated with Eqs.2.9-2.14, it is then possible to calculate the j factor using Eq.1.2. For the friction factor Churchill [1977] proposed the following correlation

$$f = \left[\left(\frac{8}{Re}\right)^{12} + (X + Y)^{-1.5}\right]^{\frac{1}{12}}, \tag{2.15}$$

where,

$$X = \left[2.457 \log\left(\left(\frac{7}{Re}\right)^{0.9} + \frac{0.27 R_a}{d_{\text{h}}}\right)^{-1}\right]^{16},$$

and

$$Y = \left(\frac{37530}{Re}\right)^{16}.$$

The term R_a represents the roughness of the channels in the heat exchanger. Typical values for R_a are $27\mu m$ for the aluminum and $13\mu m$ for the Inconel 718 [Ascione et al., 2020]. Several experimental studies have been conducted to develop correlations for the j factor and f factor. The correlations from Shah and Sekulić [2003] depend on the fin geometry as follows:

- if $\left(\frac{h}{s_\mathrm{f}}\right) \leq 1$

$$f = \frac{24}{Re}\left[1 - 1.3553\left(\frac{h}{s_\mathrm{f}}\right) + 1.9467\left(\frac{h}{s_\mathrm{f}}\right)^2 - 1.7012\left(\frac{h}{s_\mathrm{f}}\right)^3 + \right.$$
$$\left. - 0.9564\left(\frac{h}{s_\mathrm{f}}\right)^4 - 0.2537\left(\frac{h}{s_\mathrm{f}}\right)^5\right] \tag{2.16}$$

$$j = 8.235\left[1 - 10.6044\left(\frac{h}{s_\mathrm{f}}\right) + 61.1755\left(\frac{h}{s_\mathrm{f}}\right)^2 - 155.1803\left(\frac{h}{s_\mathrm{f}}\right)^3 + \right.$$
$$\left. + 176.9203\left(\frac{h}{s_\mathrm{f}}\right)^4 - 72.9236\left(\frac{h}{s_\mathrm{f}}\right)^5\right]\left(\frac{Pr^{-1/3}}{Re}\right) \tag{2.17}$$

- if $1 < \left(\frac{h}{s_\mathrm{f}}\right) < 8$

$$f = \left(\frac{12}{Re}\right)\left[\left(\frac{h}{s_\mathrm{f}}\right)^3 + 0.2595\left(\frac{h}{s_\mathrm{f}}\right)^2 - 0.2046\left(\frac{h}{s_\mathrm{f}}\right) + 0.0552\right]\left(\frac{s_\mathrm{f}}{h}\right)^3 \tag{2.18}$$

$$j = 0.912\left[\left(\frac{h}{s_\mathrm{f}}\right)^3 - 13.3739\left(\frac{h}{s_\mathrm{f}}\right)^2 + 78.9211\left(\frac{h}{s_\mathrm{f}}\right) - 46.6239\right]\left(\frac{s_\mathrm{f}}{h}\right)^3\left(\frac{Pr^{-1/3}}{Re}\right) \tag{2.19}$$

- if $\left(\frac{h}{s_\mathrm{f}}\right) \geq 8$

$$f \text{ as Eq.2.18}$$

$$j = 0.312\left(\frac{s_\mathrm{f}}{h}\right)\left(\frac{Pr^{-1/3}}{Re}\right) \tag{2.20}$$

2.1.2 Triangular Plain Fins

Triangular Plain Fins (TPF) are constructed from uninterrupted triangular channels and their unit element being two F_p wide. It is essential to note that the fin pitch F_p in the case of TPF differs from that in rectangular plain configurations (see Fig.2.3). By employing Eq.2.1 and 2.2 the surface key parameters can be evaluated replacing the following equation:

$$A_0 = (2\ Fp\ Fh) - 2t_\mathrm{f}\left(\sqrt{Fh^2 + Fp^2} - t_\mathrm{f}\right), \tag{2.21}$$

$$A_\mathrm{p} = 4\left(Fp - t_\mathrm{f}\right), \tag{2.22}$$

$$A_\mathrm{f} = 4\left(\sqrt{Fh^2 + Fp^2} - t_\mathrm{f}\right), \tag{2.23}$$

$$V_\mathrm{p} = 2\ F_\mathrm{h}\ F_\mathrm{p}. \tag{2.24}$$

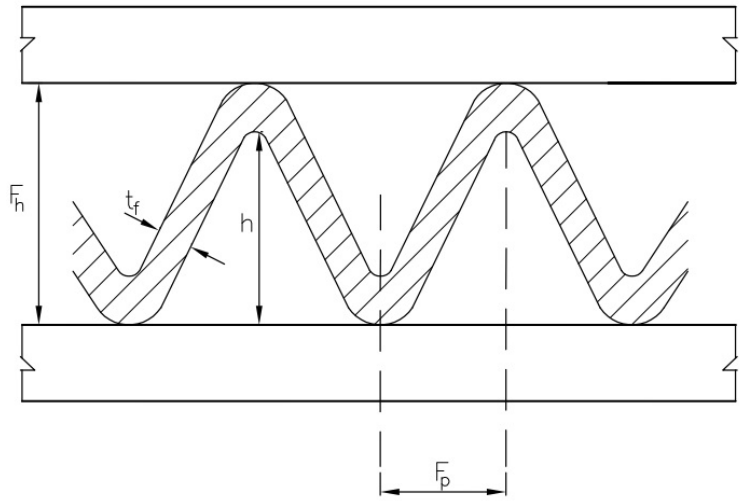

Figure 2.3: Typical geometry of triangular plain fin and its geometric parameters

In this work, for TPF two different j and f correlations will be used. The first was proposed by García-Castillo and Picón-Núñez [2021] for two Reynolds number range:
$100 < Re < 1000$

$$j = 0.718 Re^{-0.625} \left(\frac{F_\mathrm{h}}{2F_\mathrm{p}}\right)^{0.765} \left(\frac{t_\mathrm{f}}{2F_\mathrm{p}}\right)^{0.765} \tag{2.25}$$

$$f = 3.12 Re^{-0.852} \left(\frac{F_\mathrm{h}}{2F_\mathrm{p}}\right)^{0.156} \left(\frac{t_\mathrm{f}}{2F_\mathrm{p}}\right)^{-0.184} \tag{2.26}$$

$1000 \leq Re < 10000$

$$j = 0.789 Re^{-1.1218} \left(\frac{F_\mathrm{h}}{2F_\mathrm{p}}\right)^{1.235} \left(\frac{t_\mathrm{f}}{2F_\mathrm{p}}\right)^{-0.764} \tag{2.27}$$

$$f = 2.69 Re^{-0.918} \left(\frac{F_\mathrm{h}}{2F_\mathrm{p}}\right)^{0.355} \left(\frac{t_\mathrm{f}}{2F_\mathrm{p}}\right)^{-0.175} \tag{2.28}$$

On the other hand, Shah and Sekulić [2003] proposed correlations depending on the geometry. For these correlations, the term $s_\mathrm{f} = F_\mathrm{p} - t_\mathrm{f}$ is introduced.

- If $\left(\frac{h}{2s_\mathrm{f}}\right) < 0.125$:

$$f = \left(\frac{12}{Re}\right)\left(1 - 0.0115\left(\frac{h}{2s_\mathrm{f}}\right) + 1.7099\left(\frac{h}{2s_\mathrm{f}}\right)^2 - 4.3394\left(\frac{h}{2s_\mathrm{f}}\right)^3 + 4.2732\left(\frac{h}{2s_\mathrm{f}}\right)^4 + \right.$$
$$\left. - 1.5817\left(\frac{h}{2s_\mathrm{f}}\right)^5 + 0.0599\left(\frac{h}{2s_\mathrm{f}}\right)^6\right) \tag{2.29}$$

$$j = 1.088\left(\frac{h}{2s_\mathrm{f}}\right)\left(\frac{Pr^{-1/3}}{Re}\right) \tag{2.30}$$

- If $0.125 \leq \left(\frac{h}{2s_\mathrm{f}}\right) \leq 1$:

$$f \text{ as Eq.2.29}$$

$$j = -0.2113\left(1 - 10.9962\left(\frac{h}{2s_\mathrm{f}}\right) - 15.1301\left(\frac{h}{2s_\mathrm{f}}\right)^2 + 16.5921\left(\frac{h}{2s_\mathrm{f}}\right)^3\right)\left(\frac{Pr^{-1/3}}{Re}\right) \tag{2.31}$$

- If $\left(\frac{h}{2s_\mathrm{f}}\right) > 1$ same equations of Eq.2.18 and 2.20, replacing $\frac{h}{s_\mathrm{f}}$ with $\frac{h}{2s_\mathrm{f}}$

2.2 Wavy Fins

Extensive research has been conducted to enhance heat transfer in compact heat exchangers, leading to the study of wavy geometries. These surfaces are constructed using uninterrupted channels with a wavy pattern and are referred to as Wavy Fins (WF) (see Fig.2.4). Wavy fins are particularly appealing due to their ease of manufacturing and potential for improved thermal-hydraulic performance. Similar to previous sections, the channels utilizing this geometry can have varying cross-sections, and since they lack a characteristic length, all geometric parameters are calculated per unit length. The geometric parameters that define the wavy fin geometry (as shown in Fig.2.4) include:

Geometrical characteristics	
t_f	fin thickness
F_p	fin pitch
F_h	plate spacing
$2A$	wavy amplitude
λ	wavelength

Table 2.2: Geometrical characteristics of WF.

In this section, we will discuss the rectangular and triangular wavy fins that have the same cross-section of Plain Fins presented in Ch.2.1. For this reason, the unit elements and the geometric parameters that define these cross-sectional geometries are the same as those presented for the RPF (see Eq.2.5 to 2.8), and for TPF (see Eq.2.21 to 2.24). Consequently, the equations for surface key parameters are also the same.

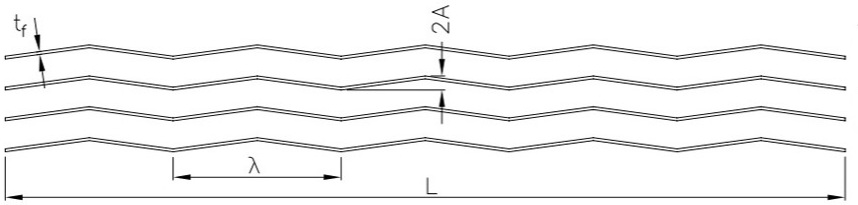

Figure 2.4: Typical geometry of wavy fin core. Adapted from Junqi et al. [2007]

2.2.1 Rectangular Wavy Fins

In the case of Rectangular Wavy Fins (RWF), Aliabadi et al. [2014] conducted experimental investigations to develop correlations for the Colburn factor and the friction factor specifically applicable to these surfaces. The experimental measurements to develop new correlations have been conducted with three different fluids: air, water, and ethylene glycol. It is interesting to note that the fluid does not affect the friction factor correlation which is always the same. On the other hand, the j factor correlation changes for each fluid analyzed. The j and f factors have the same root equation (see Eq.2.32) but with different coefficients, such as depicted in Tab.2.3.

$$F = \mathrm{A}_1 \; Re^{\mathrm{A}_2} \left(\frac{F_\mathrm{p}}{d_\mathrm{h}}\right)^{\mathrm{A}_3} \left(\frac{F_\mathrm{h}}{d_\mathrm{h}}\right)^{\mathrm{A}_4} \left(\frac{\lambda}{d_\mathrm{h}}\right)^{\mathrm{A}_5} \left(\frac{t_\mathrm{f}}{d_\mathrm{h}}\right)^{\mathrm{A}_6} \left(\frac{2A}{d_\mathrm{h}}\right)^{\mathrm{A}_7} \left(\frac{L}{d_\mathrm{h}}\right)^{\mathrm{A}_8} \tag{2.32}$$

	$Re < 1900$				$Re \geq 1900$			
F	j **factor**			f **factor**	j **factor**			f **factor**
	air	water	ethylene glycol		air	water	ethylene glycol	
A_1	0.2951	1.9603	11.1239	38.7488	0.7293	0.9001	1.2135	52.2375
A_2	-0.1908	-0.3969	-0.7509	-0.3840	-0.3637	-0.3813	-0.4461	-0.3524
A_3	0.7356	1.5063	1.7221	-1.4790	0.7966	1.5558	1.3368	-1.6277
A_4	0.1378	0.1519	0.1997	-0.3696	0.2398	0.2422	0.1825	-0.3529
A_5	-0.3171	-0.4551	-0.5022	-1.4542	-0.4979	-0.3361	-0.2929	-1.7484
A_6	0.0485	0.0699	0.0484	0.1016	0.0402	0.1081	0.1119	0.1034
A_7	0.2467	0.3892	0.3449	1.0903	0.2012	0.1587	0.1832	1.2294
A_8	-0.4976	-0.3171	-0.2193	-0.1549	-0.3026	-0.2128	-0.1707	-0.2371

Table 2.3: Constants of correlations label from Aliabadi et al. [2014].

2.2.2 Triangular Wavy Fins

For the Triangular Wavy Fins (TWF) Junqi et al. [2007] proposed two correlations for j and f factor which are valid just for $800 \leq Re \leq 6500$:

$$j = 0.0836 Re^{-0.2309} \left(\frac{F_\mathrm{p}}{F_\mathrm{h}}\right)^{0.1284} \left(\frac{F_\mathrm{p}}{2A}\right)^{-0.153} \left(\frac{L}{\lambda}\right)^{-0.326}, \tag{2.33}$$

$$f = 1.16 Re^{-0.309} \left(\frac{F_\mathrm{p}}{F_\mathrm{h}}\right)^{0.3703} \left(\frac{F_\mathrm{p}}{2A}\right)^{-0.25} \left(\frac{L}{\lambda}\right)^{-0.1152}. \tag{2.34}$$

In the sizing process (see Ch.4 and 5), the term $\frac{L}{\lambda}$ will be treated as only parameter ζ since the flow length is an output.

2.3 Offset-strip Fins

The need for improved heat exchanger performance has led to the development of various compact surfaces that differ from traditional plain and triangular fins. Among these, the offset-strip fin (OSF) has emerged as one of the most widely employed finned surfaces.
offset-strip fins, as depicted schematically in Fig.2.5, are constructed using multiple interrupted channels, enabling efficient heat transfer. The continuous starting and development of laminar boundary layers contribute to improved heat transfer performance. However, this also results in higher friction factors, leading to increased pressure drop within the heat exchanger.

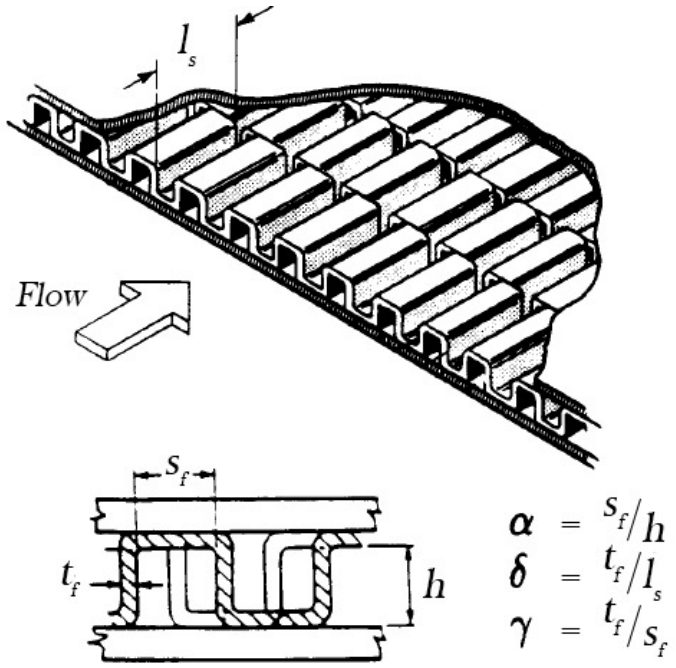

Figure 2.5: Typical geometry of an offset-strip fin core. Adapted from Manglik and Bergles [1995]

The Fig.2.5 shows the geometric parameters which describe the OSF:

Geometrical characteristics	
t_f	fin thickness
F_p	fin pitch
F_h	plate spacing
s_f	fin spacing
h	fin height
l_s	fin length

Table 2.4: Geometrical characteristics of OSF

The fin pitch is defined as $F_\mathrm{p} = s_\mathrm{f} + t_\mathrm{f}$, meanwhile ,the plate spacing is $F_\mathrm{h} = h + t_\mathrm{f}$.
For this surface geometry, the unit element considered is two F_p wide and one l_s long and the geometric characteristic are evaluated as:

$$A_0 = 2\ h\ s_\mathrm{f}, \tag{2.35}$$

$$A_\mathrm{p} = 4\ l_\mathrm{s}\ s_\mathrm{f}, \tag{2.36}$$

$$A_\mathrm{f} = (4\ h\ l_\mathrm{s}) + (4\ t_\mathrm{f}\ h) + (2\ s_\mathrm{f}\ t_\mathrm{f})\,. \tag{2.37}$$

Now, is possible to evaluate the key parameters using Eq.2.1 and Eq.2.2

Within the scientific literature, numerous experimental correlations can be found that relate the j factor and the f factor. In the present study, the correlations proposed by Manglik and Bergles [1995] will be employed. These correlations are outlined below.

$$j = 0.6522Re^{-0.5403}\alpha^{-0.1541}\delta^{0.1499}\gamma^{-0.0678}(1 + 5.259 \cdot 10^{-5}Re^{1.340}\alpha^{0.504}\delta^{0.456}\gamma^{-1.055})^{0.1} \tag{2.38}$$

$$f = 9.6243Re^{-0.7422}\alpha^{-0.1856}\delta^{0.3053}\gamma^{-0.2659}(1 + 7.669 \cdot 10^{-8}Re^{4.429}\alpha^{0.920}\delta^{3.767}\gamma^{0.236})^{0.1} \tag{2.39}$$

where $\alpha = s_\mathrm{f}/h$, $\delta = t_\mathrm{f}/l_\mathrm{s}$, $\gamma = t_\mathrm{f}/s_\mathrm{f}$. The correlations proposed above can be used just if the three parameters α, δ, and γ respect their validity bounds: $[0.134 \leq \alpha \leq 0.997\ ]$, $[0.012 \leq \delta \leq 0.048]$, $[0.021 \leq \gamma \leq 0.121]$.

2.4 Louvered Fins

Louvered Fins (LF) have been extensively studied as an alternative to offset-strip Fins (OSF) to achieve higher compactness and improved performance. Louvered fins are formed by cutting the metal and pushing out the cut parts from the plane, creating louvers that alter the flow path. When the flow enters the fin channel from the leading edge, it can follow two distinct paths: through the louvers or through the fins themselves. The presence of louvers serves to disrupt the boundary layer of the flow passing through them, similar to the function of OSF structures. In the case of louvers, the boundary layers exist on both the upper and lower surfaces of the louvers. The parameters that define the geometry of louvers are illustrated in Fig.2.6 and Tab.2.5, specifically for a triangular case with a flat tube configuration, where F_{h} is the plate spacing. Furthermore, it is worth to note that the tube pitch T_{p} indicates the distance between a plate and the flat tube. Consequently, if the louvered fins are coupled not with flat tubes but with other fin type, the tube pitch represents the distance from the top of a channel to the bottom of the next one, and is defined as

$$T_{\mathrm{p}} = F_{h_1} + F_{h_2} + t_{\mathrm{w}}.$$

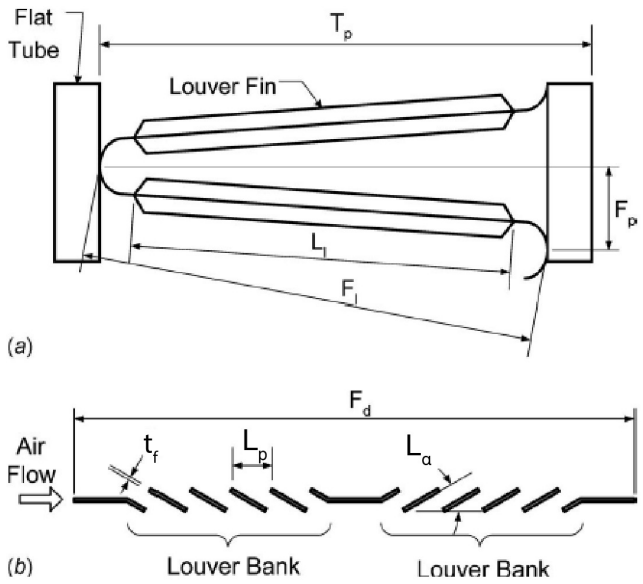

Figure 2.6: Schematic of a flat-tube louver-fin heat exchanger: (a)close-up frontal view; (b)cross-sectional view of louver fin. Adapted from Park and Jacobi [2009]

Geometrical characteristics	
F_l	fin length
L_l	louver length
T_p	tube pitch
F_p	fin pitch
F_h	fin height
L_p	louver pitch
t_f	fin thickness
F_d	fin depth
L_α	louver angle
N_LB	number of louver banks

Table 2.5: Geometrical characteristics of LF.

By knowing the values of F_l and F_p, it is possible to approximate the plate spacing as

$$F_\mathrm{h} = \sqrt{{F_\mathrm{l}}^2 - {F_\mathrm{p}}^2}.$$

This approach enables the use of triangular cross-sections with various fin angles, as well as sinusoidal cross-sections for which $F_\mathrm{l} \cong F_\mathrm{h}$ (see Fig.2.7).

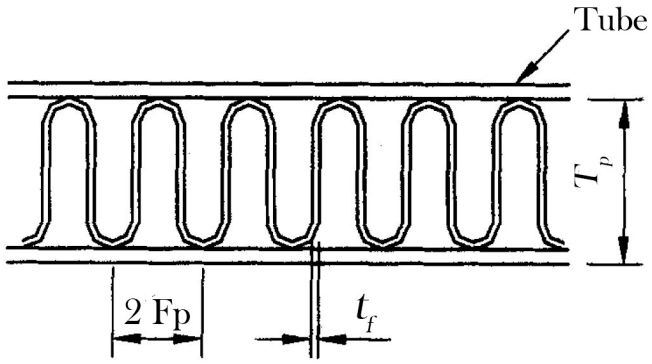

Figure 2.7: Louvered Fins with sinusoidal cross-section. Adapted from Chang and Wang [1997]

For the purpose of studying this geometry, a unit element with a width of two fin pitches and a length of one fin depth is considered. This unit element serves as a representative section for analyzing the geometric characteristics and evaluating the heat transfer and fluid flow parameters of the Louvered Fins configuration. The surface key parameters for LF, are calculated following Eq.2.1 and Eq.2.2:

$$d_\mathrm{h} = \frac{4\ A_0\ F_\mathrm{d}}{A} = \frac{4\ 2\,(F_\mathrm{p}\ F_\mathrm{h}) - 2t_\mathrm{f}(F_\mathrm{l} - t_\mathrm{f})\ F_\mathrm{d}}{4\ F_\mathrm{d}\ [(F_\mathrm{l} - t_\mathrm{f}) + (F_\mathrm{p} - t_\mathrm{f})]} \tag{2.40}$$

$$\beta = \frac{A}{V_\mathrm{p}} = \frac{4\ F_\mathrm{d}\ [(F_\mathrm{l} - t_\mathrm{f}) + (F_\mathrm{p} - t_\mathrm{f})]}{2\ F_\mathrm{p}\ F_\mathrm{h}\ F_\mathrm{d}} \tag{2.41}$$

Louvered Fins have been extensively studied to determine correlations for the Colburn factor and the friction factor. In the scientific literature, several correlations have been developed, but here just two of them will be reported. These correlations are based on Re_{lp}, which is the Reynolds number based on the louver pitch and is defined as

$$Re_{lp} = (Re\ Lp)\,/d_\mathrm{h}.$$

Chang and Wang [1997] proposed the following correlations, which can be used just in a well-defined

Re_{lp} range:

$$j = Re_{\mathrm{lp}}^{-0.49} \left(\frac{L_\alpha}{90}\right)^{0.27} \left(\frac{F_\mathrm{p}}{L_\mathrm{p}}\right)^{-0.14} \left(\frac{F_\mathrm{h}}{L_\mathrm{p}}\right)^{-0.29} \left(\frac{F_\mathrm{d}}{L_\mathrm{p}}\right)^{-0.23} \left(\frac{L_\mathrm{l}}{L_\mathrm{p}}\right)^{0.68} \left(\frac{T_\mathrm{p}}{L_\mathrm{p}}\right)^{-0.28} \left(\frac{t_\mathrm{f}}{L_\mathrm{p}}\right)^{-0.05} \tag{2.42}$$

$$f = f_1 \; f_2 \; f_3 \tag{2.43}$$

if $Re_{\mathrm{lp}} < 150$

$$f_1 = 14.39 Re_{\mathrm{lp}}^{\frac{-0.805 F_\mathrm{p}}{F_\mathrm{h}}} \log\left(1 + \frac{F_\mathrm{p}}{L_\mathrm{p}}\right)^{3.04}$$

$$f_2 = \log\left(\left(\frac{t_\mathrm{f}}{F_\mathrm{p}}\right)^{0.48} + 0.9\right)^{-1.435} \left(\frac{d_\mathrm{h}}{L_\mathrm{p}}\right)^{-3.01} \log\left(0.5 Re_{\mathrm{lp}}\right)^{-3.01}$$

$$f_3 = \left(\frac{F_\mathrm{p}}{L_\mathrm{l}}\right)^{-0.308} \left(\frac{F_\mathrm{d}}{L_\mathrm{l}}\right)^{-0.308} \exp\left(\frac{-0.1167 T_\mathrm{p}}{H_\mathrm{t}}\right) L_\alpha^{0.35}$$

if $150 \leq Re_{\mathrm{lp}} \leq 5000$

$$f_1 = 4.97 Re_{\mathrm{lp}}^{0.6049 - \frac{1.064}{L_\alpha^{0.2}}} \log\left(0.9 + \left(\frac{t_\mathrm{f}}{F_\mathrm{p}}\right)^{0.5}\right)^{-0.527}$$

$$f_2 = \left(\frac{d_\mathrm{h}}{L_\mathrm{p}} \log\left(0.3 Re_{\mathrm{lp}}\right)\right)^{-2.966} \left(\frac{F_\mathrm{p}}{L_\mathrm{l}}\right)^{\frac{-0.7931 F_\mathrm{p}}{F_\mathrm{h}}}$$

$$f_3 = \left(\frac{F_\mathrm{p}}{H_\mathrm{t}}\right)^{-0.0446} \log\left(1.2 + \left(\frac{L_\mathrm{p}}{F_\mathrm{p}}\right)^{1.4}\right)^{-3.553} L_\alpha^{-0.477}$$

Here the term H_t represents the height of the other fluid side duct.
The second correlations have been taken from Park and Jacobi [2009]:

$$\begin{aligned} j = 0.872 j_{\mathrm{Re}} \; j_{\mathrm{low}} \; j_{\mathrm{louver}} \; L_\alpha^{0.219} N_{\mathrm{LB}}^{-0.0881} \left(\frac{F_\mathrm{l}}{L_\mathrm{p}}\right)^{0.149} \left(\frac{F_\mathrm{d}}{F_\mathrm{p}}\right)^{-0.259} \left(\frac{L_\mathrm{l}}{F_\mathrm{l}}\right)^{0.54} \\ \left(\frac{F_\mathrm{l}}{T_\mathrm{p}}\right)^{-0.902} \left(1 - \frac{t_\mathrm{f}}{L_\mathrm{p}}\right)^{2.62} \left(\frac{F_\mathrm{p}}{L_\mathrm{p}}\right)^{-0.301} \end{aligned} \tag{2.44}$$

where

$$j_{\mathrm{Re}} = Re_{\mathrm{lp}}^{-0.458 - 0.00874 \cosh\left(\frac{F_\mathrm{p}}{L_\mathrm{p}} - 1\right)}$$

$$j_{\mathrm{low}} = 1 - \sin\left(\frac{L_\mathrm{p} L_\alpha}{F_\mathrm{p}}\right) \cosh\left(0.049 Re_{\mathrm{lp}} - \frac{0.142 F_\mathrm{d}/F_\mathrm{p}}{N_{\mathrm{LB}}}\right)^{-1}$$

$$j_{\mathrm{louver}} = 1 + 0.0065 \tan\left(L_\alpha\right) \frac{F_\mathrm{d}/F_\mathrm{p}}{N_{\mathrm{LB}}} \cos\left(2\pi \left(\frac{F_\mathrm{p}}{L_\mathrm{p} \tan\left(L_\alpha\right)} - 1.8\right)\right)$$

Meanwhile, the f factor correlation is

$$\begin{aligned} f = 3.69 \; f_{\mathrm{Re}} \; N_{\mathrm{LB}}^{-0.256} \left(\frac{F_\mathrm{p}}{L_\mathrm{p}}\right)^{0.904} \sin\left(L_\alpha + 0.2\right) \left(1 - \frac{F_\mathrm{l}}{T_\mathrm{p}}\right)^{0.733} \left(\frac{L_\mathrm{l}}{F_\mathrm{l}}\right)^{0.648} \\ \left(\frac{t_\mathrm{f}}{L_\mathrm{p}}\right)^{-0.647} \left(\frac{F_\mathrm{l}}{F_\mathrm{p}}\right)^{0.799} \end{aligned} \tag{2.45}$$

where

$$f_{\mathrm{Re}} = \left(Re_{\mathrm{lp}} \frac{F_{\mathrm{p}}}{L_{\mathrm{p}}} \right)^{-0.845} + 0.0013 Re_{\mathrm{lp}}^{1.26 \frac{t_{\mathrm{f}}}{F_{\mathrm{p}}}}$$

It is important to note that these equations should be used only within the specified parameter range listed in Tab.2.6, to ensure accurate results and reliable correlations for the j and f factors in Louvered Fins.

Dimensional geometric parameters									
	L_{p} [mm]	L_{p} [mm]	F_{l} [mm]	L_{l} [mm]	L_{α} [°]	F_{d} [mm]	T_{p} [mm]	t_{f} [mm]	N_{LB}
Min	0.5	0.51	2.84	2.13	8.4	15.6	3.76	0.0254	1
Max	3	5.08	20	18.5	35.9	57.4	25	0.16	4

Nondimensional parameters						
	$F_{\mathrm{p}}/L_{\mathrm{p}}$	$F_{\mathrm{l}}/F_{\mathrm{p}}$	$L_{\mathrm{l}}/F_{\mathrm{l}}$	$F_{\mathrm{d}}/F_{\mathrm{p}}$	$T_{\mathrm{p}}/F_{\mathrm{l}}$	$t_{\mathrm{f}}/L_{\mathrm{p}}$
Min	0.45	2.6	0.63	5	1.12	0.025
Max	4.44	16	0.96	40	1.37	0.155

Table 2.6: Validity bounds of geometric parameters for LF

2.5 Verification of Geometries and Correlations

This chapter presents the verification of the geometry models and of the correlations using the experimental data from Kays and London [2018][2].
The verification of the geometry models has been conducted focusing on just two key-surface parameters: the hydraulic diameter d_{h} and the area density β. These two geometric parameters have been evaluated with the equation introduced and developed in the previous sections and, then, they have been compared with the experimental data of Kays and London [2018]. The deviation of the current geometric results from the reference data is evaluated as:

$$\%dev_{\mathrm{x}} = \frac{x_{\mathrm{cur}} - x_{\mathrm{ref}}}{x_{\mathrm{ref}}} \, 100. \tag{2.46}$$

Here, x represents the generic variable, the subscript 'cur' denotes the current values, and the subscript 'ref' refers to the reference values. The results are shown in Fig.2.8.
It is worth noting that the errors observed were generally very small, with a few cases reaching a maximum of about 3%. These results indicate that the geometry equations derived in Chs.2.1 - 2.4 are reliable and can be effectively used in this work.

The verification of the j and f equations (Figs.2.9 and 2.10), have been made comparing the correlations proposed in the previous sections with experimental results of a single comparative case provided by Kays and London [2018] (see Tab.2.7). The error from the reference case was calculated using Eq.2.46.
Upon analysis, it can be observed that the j and f correlations for the OSF and TWF cases yield results that are relatively close to the experimental data, with a maximum deviation of approximately 5%. However, for the plain fins, it is evident that the correlations proposed for TPF significantly differ from the experimental data. The comparison of j factors reveals a substantial difference, and in the case of f factors, only the correlation by García-Castillo and Picón-Núñez [2021] somewhat fits the experimental data for low Reynolds numbers (up to approximately 800).

[2]In this verification the offset-strip fins with surface designation (D) have not been considered since this geometry is a bit different from the one analyzed here and the errors are high. Additionally, for triangular louvered fins, only three cases are listed in Kays and London [2018].

fin geometry	**surface designation from [15]**
RPF	6.2
TPF	10.27T
TWF	11.44-3/8W and 11.5-3/8W
OSF	1/8-15.61
LF	3/4-11.1

Table 2.7: Selected surface designations of fin geometry for correlations verification

The equations from Gnielinski [2010] for the prediction of the j factor has a good level of accuracy for the RPF. Though, at the time of writing, it hasn't been found an accurate correlation for the prediction of the friction factor. This may be attributed to the fact that in f correlation by Churchill [1977], the Prandtl number Pr and the roughness Ra are involved and, since their values are not given for reference case, for this comparison have been assumed to be $Pr = 0.8$ and $Ra = 1.3e{-}5mm$.
For the LF, it is worth noting that the correlations proposed by Chang and Wang [1997] exhibit the lowest deviation from the reference case and are the most accurate. The deviation from the reference case is, mainly, given by the fact that the correlations proposed in Ch.2.4 have been developed for triangular louvered fins with flat tubes, while the experimental data from Kays and London [2018] refer only to triangular louvered fins. Consequently, some of the parameters required in the correlations had to be assumed in order to facilitate the comparison since they are not provided in the reference ($L_\alpha = 28°$, $T_\mathrm{p}/F_\mathrm{l} = 1.37$, $N_\mathrm{LB} = 2$).
The j and f correlations of RWF have been compared with several experimental data for this fin type, and the Figs.2.9(d) and 2.10(d) show that the correlations proposed by Aliabadi et al. [2014] give good results with deviation from experimental results within 12%.

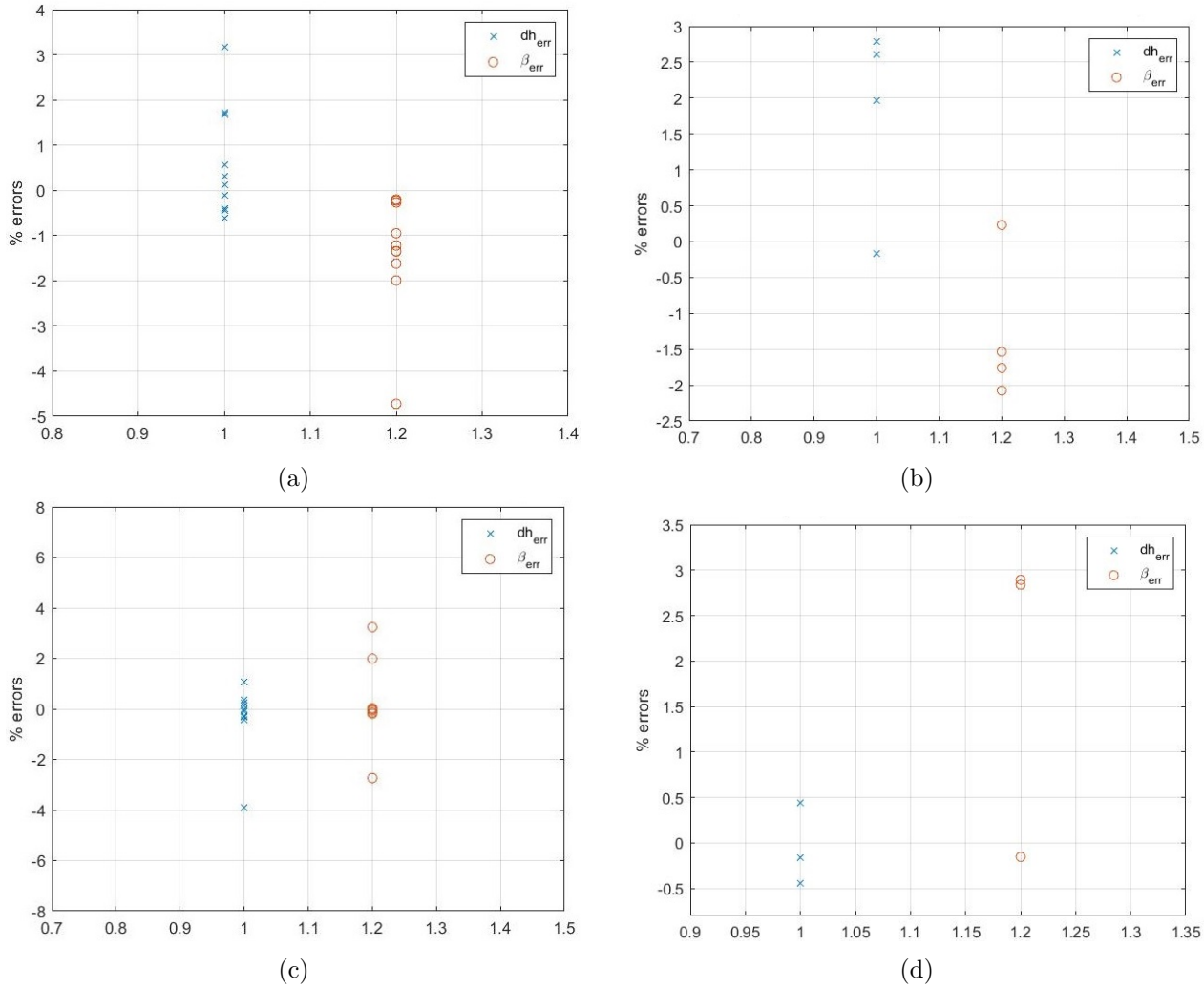

Figure 2.8: Percentages errors of d_{h} and β of present work compared with data of [15] for: (a) Rectangular fins (plain or wavy), (b) Triangular fins (plain or wavy), (c) offset-strip fins, (d) Triangular louvered fins.

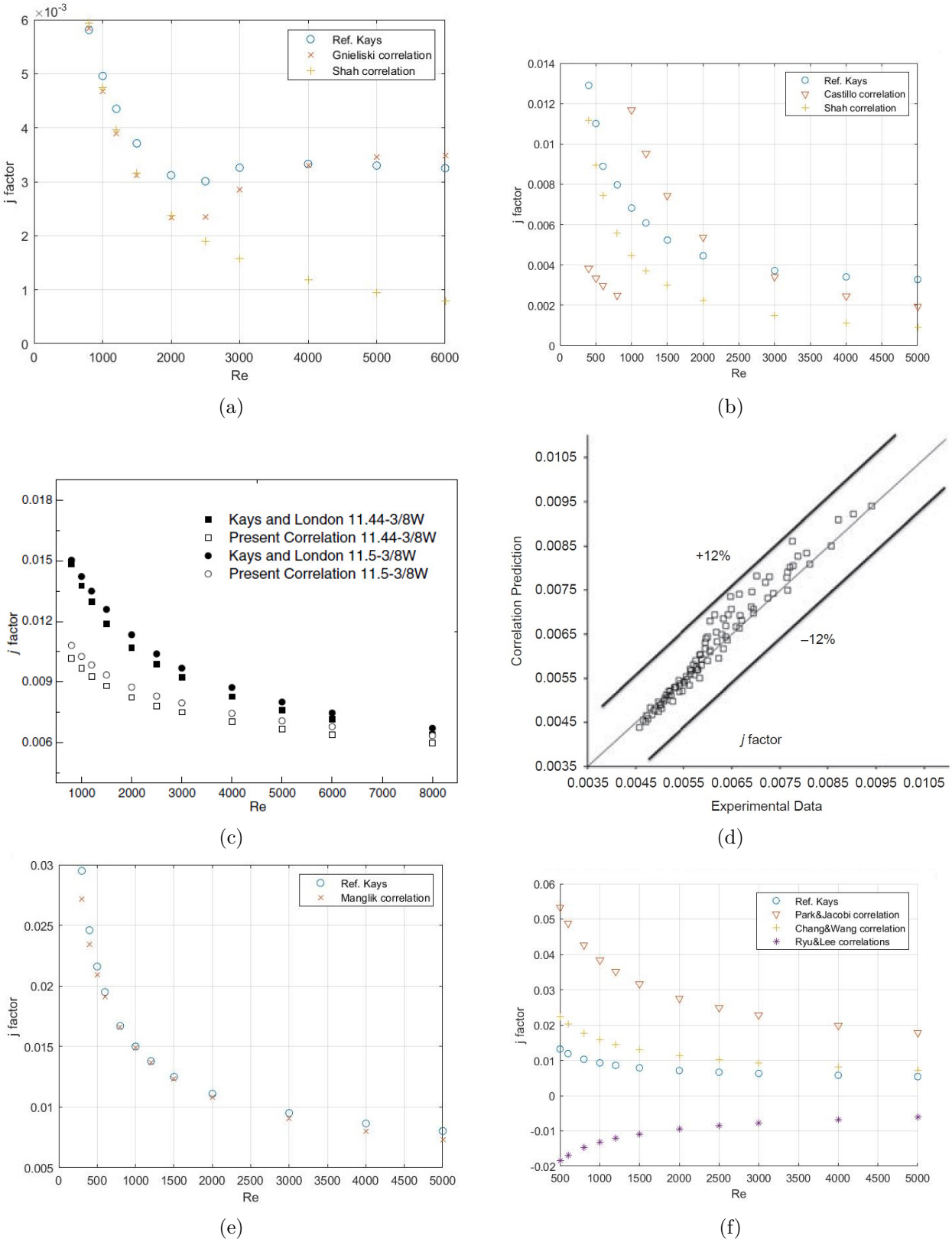

Figure 2.9: Comparison of j correlations with experimental data from [15] for (a) rectangular plain fins, (b) triangular plain fins, (c) triangular wavy fins (taken from [13]), (d) rectangular wavy fins (taken from [1]), (e) offset-strip fins, (f) triangular louvered fins.

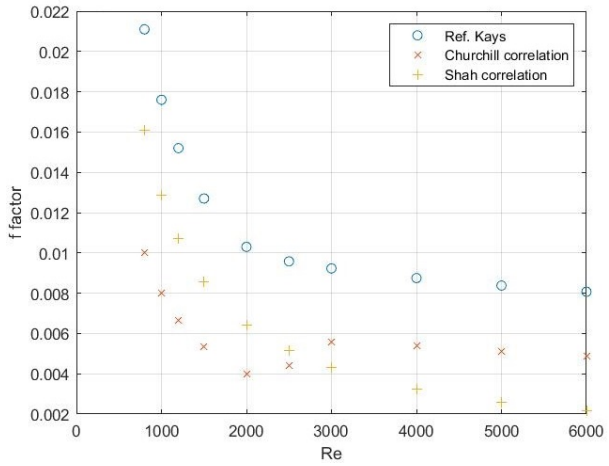

(a)

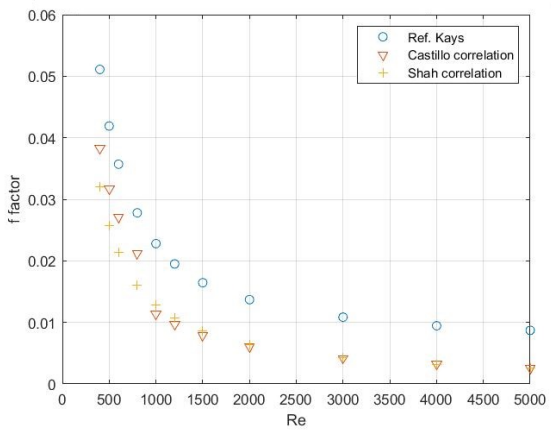

(b)

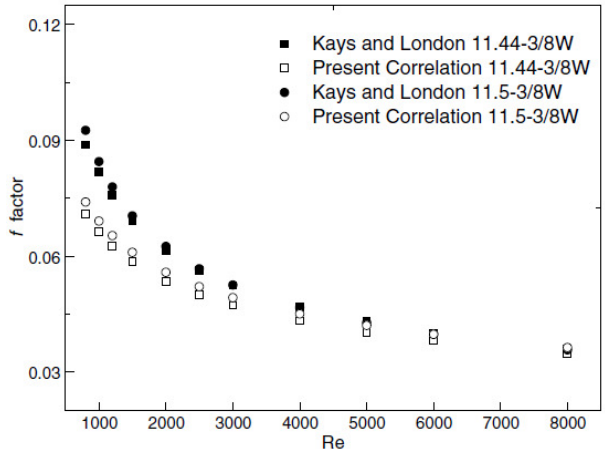

(c)

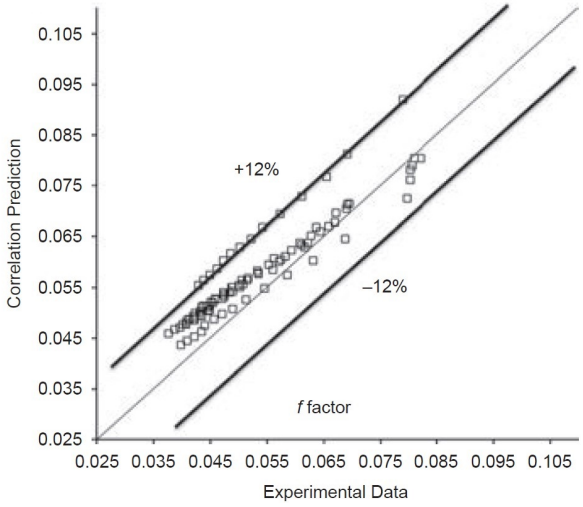

(d)

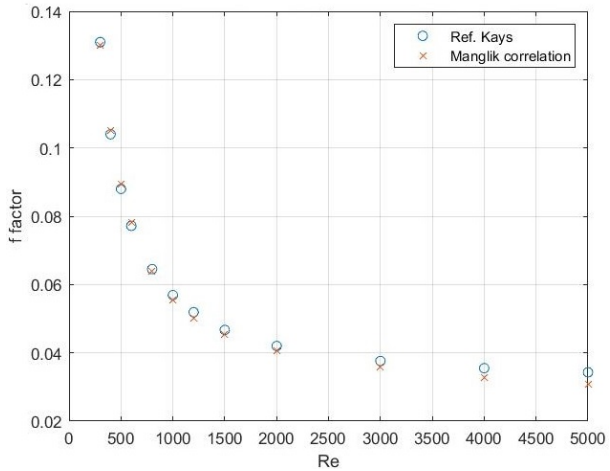

(e)

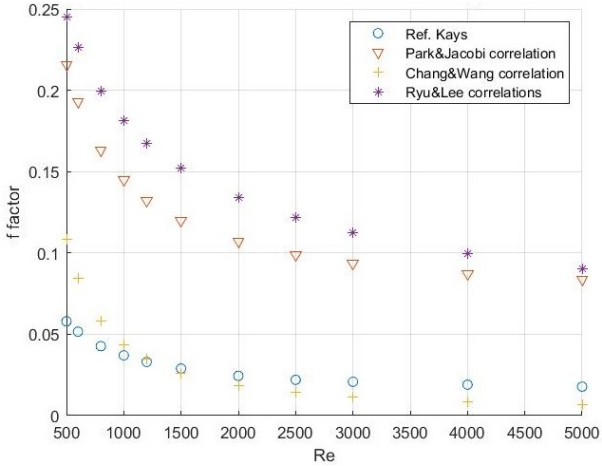

(f)

Figure 2.10: Comparison of f correlations with experimental data from [15] for (a) rectangular plain fins, (b) triangular plain fins, (c) triangular wavy fins (taken from [13]), (d) rectangular wavy fins (taken from [1]), (e) offset-strip fins, (f) triangular louvered fins.

Chapter 3

Overview of the heat transfer problem

The heat exchanger thermal design problem may be of two different types: a rating problem (Ch.4) or a sizing problem (Ch.5).
The aim of the rating problem is the determination of heat transfer rate and pressure drops of an already-sized exchanger. Meanwhile, the sizing problem needs to evaluate sizes (length, width, and height) and pressure drops of heat exchangers, knowing the heat duty.
These heat transfer problems will be analyzed using the following assumptions, introduced by Shah and Sekulić [2003]:

1. The operational conditions are steady-state (independent of time);
2. The heat losses are negligible;
3. There are no thermal energy sources or sinks, electric heating, chemical reaction, or nuclear processes in the heat exchanger;
4. The temperature has a uniform distribution over every cross section in counterflow and parallel flow exchangers;
5. The wall thermal resistance is distributed uniformly in the entire heat exchanger;
6. There is no phase change;
7. Longitudinal heat conduction in the fluids and in the wall is negligible;
8. The individual and overall heat transfer coefficients are constant and independent of temperature, time, and position along the heat exchanger;
9. The specific heat of each fluid is constant throughout the exchanger;
10. The overall extended surface efficiency η_0 for a fin heat transfer area is constant and uniform;
11. The total heat transfer area is distributed uniformly on each fluid side;
12. There is no gross flow maldistribution at the inlet: the velocity and temperature are uniform over the flow cross-section at the entrance of the ducts;
13. The fluid flow rate is uniformly distributed through the exchanger on each fluid side in each duct. The flow is defined by its characteristic in bulk at any cross-section;
14. There are no leakages from one fluid to the other one.

Before describing the rating an sizing problems, it is useful to present the parameters that play important roles in the heat transfer problem and the method on which it is based.
In relation to the extended surface of heat exchangers, it is important to analyze the distribution of temperature on a cross-section of a fin. The temperature distribution is non-uniform, generally

decreasing from the base (primary surface) to the tip when the fin is cooled. Conversely, when the fin is heated, the temperature exhibits an increasing profile from the surface, as illustrated in Fig.3.1. This phenomenon reduces the average temperature difference between the fin and the fluid. To account for this effect, the fin efficiency η_{f} is introduced. The latter is the measure of the thermal performance of a fin and is defined as:

$$\eta_{\mathrm{f}} = \frac{\dot{Q}_0}{\dot{Q}_{\max}}. \tag{3.1}$$

Here, $\dot{Q}_0$ represents the heat transfer rate through the fin base, while $\dot{Q}_{\max}$ denotes the maximum heat duty, defined as

$$\dot{Q}_{\max} = C_{\min}\left(T_{\mathrm{i_h}} - T_{\mathrm{i_c}}\right).$$

The maximum heat transfer rate is defined as the maximum one thermally possible for a "perfect" counter-flow heat exchanger with an infinite surface area, with the same inlet temperatures and mass flow rates of the actual recuperator.

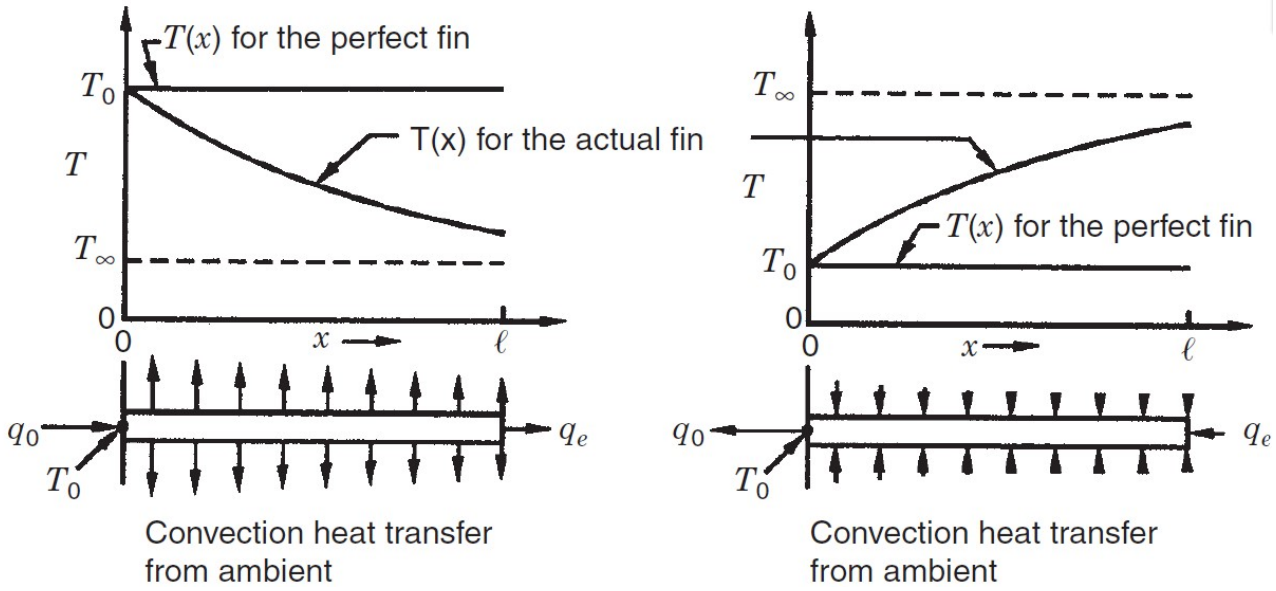

Figure 3.1: Temperature profile for actual thin fins: fin is being cooled (left); fin is being heated (right). Taken from Shah and Webb [1983]

According to Shah and Sekulić [2003], the center of a fin can be treated as adiabatic (no heat transfer through the center), leading to an appropriate formula for fin efficiency:

$$\eta_{\mathrm{f}} = \frac{\tanh(m\ l)}{m\ l}. \tag{3.2}$$

Here, l represents the fin length for heat conduction from the primary surface to the adiabatic plane and is dependent on the cross-section geometry. For fins with rectangular or square channel shapes, l is

$$l = \frac{F_{\mathrm{h}} - t_{\mathrm{f}}}{2}. \tag{3.3}$$

Meanwhile, the fins with triangular cross-section have l defined as follows:

$$l = \frac{1}{2}\left(\sqrt{F_{\mathrm{h}}^2 + F_{\mathrm{p}}^2} - 2t_{\mathrm{f}}\right). \tag{3.4}$$

The m parameter in Eq.3.2 is defined as $m = \left(\frac{h\ P}{k_{\mathrm{f}}\ A_{\mathrm{k}}}\right)^{1/2}$, where P is the perimeter for surface convection, A_{k} is the fin area for heat conduction, and k_{f} is the fin conductivity. This expression of

m can be simplified and written as follows:

$$m = \left(\frac{2\ h}{k_\mathrm{f}\ t_\mathrm{f}} \right)^{1/2}. \tag{3.5}$$

This expression is valid when $t_\mathrm{f} \ll L$. The fin efficiency is also utilized to assess the extended surface efficiency, denoted as η_0, which defines the heat transfer performance of the fins. The extended surface efficiency is defined as:

$$\eta_0 = \frac{\dot{Q}_\mathrm{tot}}{\dot{Q}_\mathrm{max}}, \tag{3.6}$$

where the total and the maximum heat duty can be expressed as

$$\dot{Q}_\mathrm{tot} = h\ A_\mathrm{p}\,(T_0 - T_\infty) + h\ A_\mathrm{f}\ \eta_\mathrm{f}\,(T_0 - T_\infty) \qquad \text{and} \qquad \dot{Q}_\mathrm{max} = h\,(A_\mathrm{p} + A_\mathrm{f})\,(T_0 - T_\infty)\,.$$

Thus, Eq.3.6 can be rewritten as follows:

$$\eta_0 = 1 - \frac{A_\mathrm{f}}{A}\,(1 - \eta_\mathrm{f})\,. \tag{3.7}$$

To facilitate the study of heat transfer problems, it is useful to establish an analogy between heat transfer and electrical conduction. In this analogy, the heat transfer rate and the temperature difference can be seen as the electric current and the potential difference. The overall thermal resistance $R = 1/(UA)$ consists of component resistances in series:

$$R = R_\mathrm{h} + R_\mathrm{h,f} + R_\mathrm{w} + R_\mathrm{c} + R_\mathrm{c,f}, \tag{3.8}$$

where R_w is the thermal resistance of the wall, R_h and R_c represent the thermal resistances given by the surfaces on the two sides, and lastly the components $R_\mathrm{h,f}$ and $R_\mathrm{c,f}$ are the contributes of the fouling film. This last term given by the fouling films can be neglected. For a plate-fin heat exchanger, the wall and fluid side resistances are defined as:

$$R_\mathrm{w} = \frac{t_\mathrm{w}}{k_\mathrm{w}\ A_\mathrm{w}} \tag{3.9}$$

$$R_h = \frac{1}{\eta_{0_\mathrm{h}}\ h_\mathrm{h}\ A_\mathrm{h}} \tag{3.10}$$

$$R_c = \frac{1}{\eta_{0_\mathrm{c}}\ h_\mathrm{c}\ A_\mathrm{c}}. \tag{3.11}$$

Consequently, substituting Eqs.3.9, 3.10, and 3.11 in Eq.3.8, the overall thermal resistance is rewritten as follows:

$$\frac{1}{UA} = \frac{1}{(\eta_0\ h\ A)_h} + \frac{t_\mathrm{w}}{k_\mathrm{w}\ A_\mathrm{w}} + \frac{1}{(\eta_0\ h\ A)_c}. \tag{3.12}$$

The heat exchanger will be analyzed in three different main sections where the properties of the fluid will be assessed: inlet, mean, and outlet section. The variables denoted with subscript 'i' relate to the inlet section, where the thermodynamic parameters are known. The subscript 'm' refers to the mean section of the exchanger, while the variables associated with the outlet section are indicated with the subscript 'o'. Furthermore, the parameters will be defined by the subscripts 'c', for the cold side, and 'h', for the hot side. The subscript's nomenclature used here will be sorted as follows: first, the subscript that indicates the section, and last the subscript which denotes the fluid side. For instance, the outlet temperature on the cold side will be represented by $T_{\mathrm{o_c}}$.
In the present work, the procedure of the rating and sizing problem is based on the $\epsilon - NTU$ method. The heat duty $\dot{Q}$ is defined as

$$\dot{Q} = \epsilon\ C_\mathrm{min}\,(T_{\mathrm{i_h}} - T_{\mathrm{i_c}}) = \epsilon\ C_\mathrm{min}\ \Delta T_\mathrm{max} \tag{3.13}$$

where ϵ represents the heat exchanger effectiveness, denoting its thermal performance, $C_{\min}$ corresponds to the minimum heat capacity between C_h and C_c, while $\Delta T_{\max}$ is the fluid inlet temperature difference, which represents the highest value. The effectiveness ϵ, which represents the ratio of actual heat transfer rate $\dot{Q}$ over the maximum possible $\dot{Q}_{\max}$

$$\epsilon = \frac{\dot{Q}}{\dot{Q}_{\max}}, \tag{3.14}$$

is generally influenced by the number of transfer units $NTU = UA/C_{\min}$, the heat capacity ratio C^*, and the flow arrangement. To proceed with the resolution of the problem, several relationships between the effectiveness and NTU have been established, according to the flow arrangement.
For a cross-flow heat exchanger, the equation for the evaluation of ϵ is dependent on the side of $C_{\min}$ and on the fin type which determines if the flow is mixed or unmixed. In the following, a few epsilon NTU relations for cross-flow arrangement are presented.

Both fluids unmixed

$$\epsilon = 1 - \exp(-NTU) - \exp[-(1+C^*)NTU] \sum_{n-1}^{\infty} C^{*n} P_{\mathrm{n}}(NTU) \tag{3.15}$$

with

$$P_{\mathrm{n}}(y) = \frac{1}{(n+1)!} \sum_{j=1}^{n} \frac{(n+1-j)}{j!} y^{n+1}.$$

The $C_{\min}$ fluid mixed and the C_{max} fluid unmixed

$$\epsilon = 1 - \exp\left\{ -\frac{[1 - \exp(-NTU\ C^*)]}{C^*} \right\} \tag{3.16}$$

The $C_{\min}$ fluid unmixed and the C_{max} fluid mixed

$$\epsilon = \frac{1}{C^*}(1 - \exp\{-C^*[1 - \exp(-NTU)]\}) \tag{3.17}$$

Both fluids mixed

$$\epsilon = \frac{1}{\frac{1}{1-\exp(-NTU)} + \frac{C^*}{1-\exp(-NTU\ C^*)} - \frac{1}{NTU}} \tag{3.18}$$

Since the Eq,3.15 is difficult to implement, the ϵ in cross-flow exchanger with both fluids unmixed is evaluated using a different formula:

$$\epsilon = 1 - \exp\left[\frac{\exp(-C^*\ NTU^{0.78}) - 1}{C^*\ NTU^{-0.22}} \right] \tag{3.19}$$

Eq.3.19 is an empirical formula and its origins are uncertain but it may be attributed to R. M. Drake [Digiovanni and Webb, 1989]. This "formula provides inaccurate results (up to 3.8% uncertainty) when the values of the thermal capacity ratio are large and those of the number of transfer units are small" [Triboix, 2008]. The NTU is iteratively determined from the implicit equation using a gradient-based solver implemented in Python.
Meanwhile, the equations for ϵ evaluation for counter and parallel flow arrangement are respectively:

Counter-flow

$$\epsilon = \frac{1 - \exp[-NTU(1-C^*)]}{1 - C^* \exp[-NTU(1-C^*)]} \tag{3.20}$$

Parallel-flow

$$\epsilon = \frac{1 - \exp[-NTU(1+C^*)]}{1 + C^*}. \tag{3.21}$$

The use of the $\epsilon - NTU$ method for heat transfer problems has many advantages but also some drawbacks. This method allows a good determination of improvements in performance for enhanced surface area, thanks to the relationship between the effectiveness and NTU. The NTU and C^* are not significantly affected by changes in the inlet temperatures and, for this reason, this method can accurately predict the resulting outlet temperatures, even with changes in inlet temperature. On the other hand, the $\epsilon - NTU$ method needs to evaluate the $C_{\min}$ side and lacks its validity with high effectiveness since the thermal longitudinal effects are not negligible anymore. Moreover, this method does not use an equation that relates epsilon and NTU depending on the flow arrangement and even geometry.

Chapter 4

Heat exchanger rating

The rating process primarily concentrates on the evaluation of pressure drops and heat transfer rates for a given heat exchanger. The inputs required for the rating problem are several key factors, including the exchanger sizes (width x, height y, and length z), thermodynamic parameters (such as inlet temperatures, inlet pressures, and mass flow rates), surface geometric parameters (depending on the fin geometries adopted), flow arrangement (cross, counter, or parallel), and specific details regarding the plate structure, including material composition, plate thickness, and roughness.

4.1 Methodology

This section presents the rating method employed in the current work, based on the methodology outlined by Shah and Sekulić [2003]. The fundamental steps of this approach are summarized in the flow chart of Fig.4.1.
The rating process begins with the assessment of geometric parameters for each fluid side of the heat exchanger. This step mainly relies on the fin type employed for each fluid side and makes use of the specific geometric parameters defined in Ch.2. The number of flow passages N_{p}, assumed to be the same for both fluids, and the total volume of flow passages can be determined as follows:

$$N_{\mathrm{p}} = \frac{y - t_{\mathrm{w}}}{F_{\mathrm{h_c}} + F_{\mathrm{h_h}} + 2t_{\mathrm{w}}}, \tag{4.1}$$

$$V_{\mathrm{p_c}} = x\ z\ F_{\mathrm{h_c}}\ N_{\mathrm{p_c}} \qquad\qquad V_{\mathrm{p_h}} = x\ z\ F_{\mathrm{h_h}}\ N_{\mathrm{p_h}}. \tag{4.2}$$

Here, the height of the exchanger y is the no-flow length, x and z represent the flow lengths of the two sides, corresponding to the width and length of the heat exchanger, respectively.
After the estimation of fin geometric parameters, is feasible to evaluate the surface areas of the heat exchanger. For the calculation of the total heat transfer area, the definition of area density β (Eq.2.2) is used:

$$A_{\mathrm{c}} = \beta_c\ V_{\mathrm{p_c}} \qquad\qquad A_{\mathrm{h}} = \beta_h\ V_{\mathrm{p_h}}. \tag{4.3}$$

The minimum free-flow area A_0 is evaluated through the definition of hydraulic diameter d_{h} (Eq.2.1) as:

$$A_{0_{\mathrm{c}}} = \frac{d_{\mathrm{h_c}}\ A_{\mathrm{c}}}{4\ z} \qquad\qquad A_{0_{\mathrm{h}}} = \frac{d_{\mathrm{h_h}}\ A_{\mathrm{h}}}{4\ x}, \tag{4.4}$$

meanwhile, the frontal area A_{fr} can be determined based on its definition:

$$A_{\mathrm{fr_c}} = x\ y \qquad\qquad A_{\mathrm{fr_h}} = z\ y. \tag{4.5}$$

Subsequently, the surface ratio parameters α and σ, defined in Ch.2, can be evaluated. The σ represents the minimum free-flow area over the frontal surface area

$$\sigma_{\mathrm{c}} = \frac{A_{0_{\mathrm{c}}}}{A_{\mathrm{fr_c}}} \qquad\qquad \sigma_{\mathrm{h}} = \frac{A_{0_{\mathrm{h}}}}{A_{\mathrm{fr_h}}}, \tag{4.6}$$

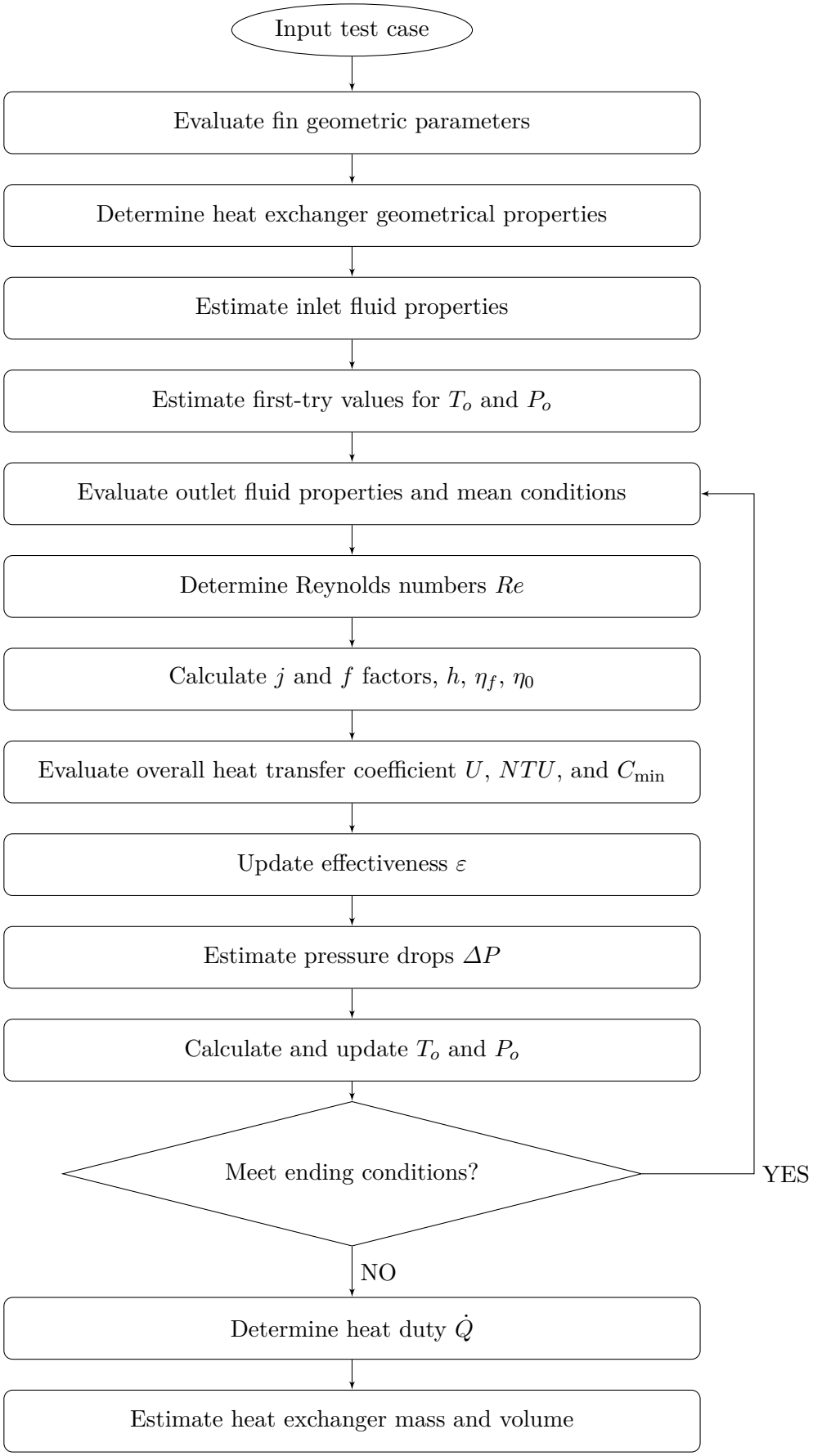

Figure 4.1: Flow chart for heat exchanger rating.

and the compactness α is evaluated following Eq.2.4, which relates α and σ:

$$\alpha_{\mathrm{c}} = \frac{4\sigma_{\mathrm{c}}}{d_{\mathrm{h_c}}} \qquad \alpha_{\mathrm{h}} = \frac{4\sigma_{\mathrm{h}}}{d_{\mathrm{h_h}}}. \tag{4.7}$$

Once the surface geometry has been defined, it needs to evaluate the fluid properties at inlet conditions and, then, it becomes feasible to start with the rating process. The computation of all the fluid properties (c_{p}, μ, ρ, k, and Pr) is accomplished with the Python library CoolProp [Bell et al., 2014], with specific temperatures and pressures for the section under consideration. Then, the bulk fluid properties can be determined using the mean temperatures and mean pressures as

$$T_{\mathrm{m_{c,h}}} = 0.5\left(T_{\mathrm{i_{c,h}}} + T_{\mathrm{o_{c,h}}}\right) \qquad \text{and} \qquad P_{\mathrm{m_{c,h}}} = 0.5\left(P_{\mathrm{i_{c,h}}} + P_{\mathrm{o_{c,h}}}\right).$$

Since the outlet conditions are not given, the first guess outlet pressures are set as the 90% of the inlet pressures. Additionally, the values of outlet temperatures are estimated based on the effectiveness value ϵ and assuming (as an initial approximation) that $c_{\mathrm{p_b}} = c_{\mathrm{p_i}}$. A typical value of effectiveness for single-pass cross-flow exchangers is between 50 and 75% and, in the present work, is assumed $\epsilon = 0.7$. Consequently, the outlet temperatures are calculated according to the following expressions:

$$T_{\mathrm{o,h}} = T_{\mathrm{i,h}} - \epsilon\frac{C_{\mathrm{min}}}{C_h}\left(T_{\mathrm{i,h}} - T_{\mathrm{i,c}}\right) \tag{4.8}$$

$$T_{\mathrm{o,c}} = T_{\mathrm{i,c}} + \epsilon\frac{C_{\mathrm{min}}}{C_c}\left(T_{\mathrm{i,h}} - T_{\mathrm{i,c}}\right) \tag{4.9}$$

where the heat capacities are $C_{\mathrm{h,c}} = \dot{m}_{\mathrm{h,c}}\, c_{\mathrm{p_{h,c}}}$. In order to achieve convergence towards the appropriate outlet temperature values, the following process will be repeated until the ending conditions are met. The convergence loop will terminate when the residual of the outlet temperature ($res_{\mathrm{T_o}}$) or the one of the outlet c_{p} (res_{fp}) exceeds the specified tolerance (tol) or when the number of iterations ($\mathrm{n_{iter}}$) exceeds the maximum number of iterations ($\mathrm{max_{iter}}$). The values for the tolerance and maximum iterations are arbitrarily determined and here are imposed as $tol = 1e-4$ and $\mathrm{max_{iter}} = 10$. Since the outlet conditions have been initially estimated, it is now feasible to proceed with evaluating the fluid properties in the outlet section.
The next step involves estimating the Reynolds numbers Re which are essential for determining the heat transfer parameters, such as j, f, h, η_{f}, and η_0. The Reynolds number based on the hydraulic diameter is defined as $Re = u\ d_{\mathrm{h}}\ \rho/\mu$. By substituting the fluid velocity derived from the mass flow rate equation $\dot{m} = \rho\ u\ A_0$, the Re can be evaluated as follows:

$$Re = \frac{G\ d_{\mathrm{h}}}{\mu}. \tag{4.10}$$

Here, the G represents the fluid mass velocity based on the minimum free-flow area and is given by $G = \dot{m}/A_0$. Knowing the value of Reynolds numbers is possible to evaluate the j and f factors on both sides following the equations specified in the Ch.2, depending on the fin geometry.
Consequently, the j factor is used to evaluate the heat transfer coefficient h as:

$$h = \frac{j\ Re\ Pr^{1/3}\ k}{d_{\mathrm{h}}}. \tag{4.11}$$

Then, knowing the value of the heat transfer coefficient is possible to calculate the fin efficiency η_{f}, and the surface efficiency η_0, following Eq.3.2 and Eq.3.7, respectively.
Next, UA must be calculated using Eq.3.12. It is worth highlighting that the term UA is constant and is equal for the hot side (h), cold side (c), and wall (w) of the heat exchanger,

$$UA = (UA)_{\mathrm{h}} = (UA)_{\mathrm{c}} = (UA)_{\mathrm{w}}\,. \tag{4.12}$$

The plate area A_{w} of Eq.3.12 can be computed as:

$$A_{\mathrm{w}} = x\ z\,(n_{\mathrm{p}} + 1)\,, \tag{4.13}$$

where n_p is the total number of plates and is calculated as

$$n_\mathrm{p} = 2\left(\frac{y}{F_{\mathrm{h_c}} + F_{\mathrm{h_h}}} + 2t_\mathrm{w}\right),$$

rounding it up to the nearest integer.
At this point of the rating process it is possible to update the ϵ value using Eq.3.19, with current values of $NTU = UA/C_\mathrm{min}$ and C^*.
Then, the overall pressure drop across the heat exchanger core is estimated as::

$$\Delta P = \left(\frac{G^2}{2\rho_\mathrm{i}}\right)\left[\left(1-\sigma^2+K_\mathrm{c}\right) + 2\left(\frac{1}{\rho_\mathrm{o}} - \frac{1}{\rho_\mathrm{i}}\right) + \left(\frac{4\ f\ L\ \rho_\mathrm{i}}{d_\mathrm{h}\rho_\mathrm{m}}\right) - \left(\frac{1-\sigma^2-K_\mathrm{e}}{\rho_\mathrm{i}/\rho_\mathrm{o}}\right)\right], \tag{4.14}$$

where ρ_m is the harmonic mean density between inlet and outlet, L is the flow length (x for the hot side, and z for the cold side), K_c is the entrance or contraction pressure loss coefficient and K_e is the exit or expansion loss coefficient.
The coefficient K_c represents the entrance pressure-loss coefficient, which accounts for the abrupt contraction at the entrance of the heat exchanger. K_e, on the other hand, is the exit expansion coefficient, taking into consideration the expansion at the exit. Both coefficients are functions of the channel geometry and Reynolds number. The curves of K_c and K_e as functions of σ, for different Reynolds numbers can be found in Fig.4.2. Consequently, the equations to evaluate these two coefficients have been found interpolating multiple points of the curves with second order polynomials. It should be noted that interrupted and uninterrupted fins have different equations since interrupted fins break the flow and do not reach a fully established velocity profile. In such cases, the K_c and K_e curves for $Re = \infty$ are used:

$$K_\mathrm{c} = \begin{cases} -0.1607\sigma^2 - 0.3082\sigma + 0.4979 & \text{with interrupted channels} \\ -0.4524\sigma^2 + 0.0429\sigma + 0.5738 & \text{with uninterrupted channels} \end{cases} \tag{4.15}$$

$$K_\mathrm{e} = \begin{cases} 0.9167\sigma^2 - 1.9107\sigma + 0.984 & \text{with interrupted channels} \\ 1.3036\sigma^2 - 2.5546\sigma + 1.1101 & \text{with uninterrupted channels} \end{cases} \tag{4.16}$$

If $Re > 2000$, Eq.4.15 for uninterrupted fins is modified to account for the effect of the Reynolds number. This modification consists in multiplying the final coefficient by

$$\left[1 + (Re10^{-9})^2 - (2Re10^{-5}) + 0.0314\right].$$

In Eq.4.14, the first term between square brackets represents the pressure drop at the entrance, while the last term expresses the contribution of the exit. Lastly, the main contributor to the pressure drop is given by the core, represented by the second and third terms in the square brackets. Moreover, it is interesting to note that the Eqs.4.15 and 4.16 refer to square channels but, since curves in Fig.4.2a and Fig.4.2b are very close, in this study the Eqs.4.15 and 4.16 are used with any geometry.
In Eq.4.14 the friction factor f has been corrected for fluid properties variations, following the approach of Shah and Sekulić [2003]. This correction accounts for the ratio of surface temperature (T_w) to the bulk temperature (T_m). The variation of temperature affects the viscosity, the thermal conductivity, and the density of gases, meanwhile, for liquids it influences only the viscosity. This temperature-dependent properties are expressed by the following equations for Nusselt numbers and friction factors:

For gases

$$\frac{Nu}{Nu_\mathrm{cp}} = \left(\frac{T_\mathrm{w}}{T_\mathrm{m}}\right)^n \qquad \frac{f}{f_\mathrm{cp}} = \left(\frac{T_\mathrm{w}}{T_\mathrm{m}}\right)^m \tag{4.17}$$

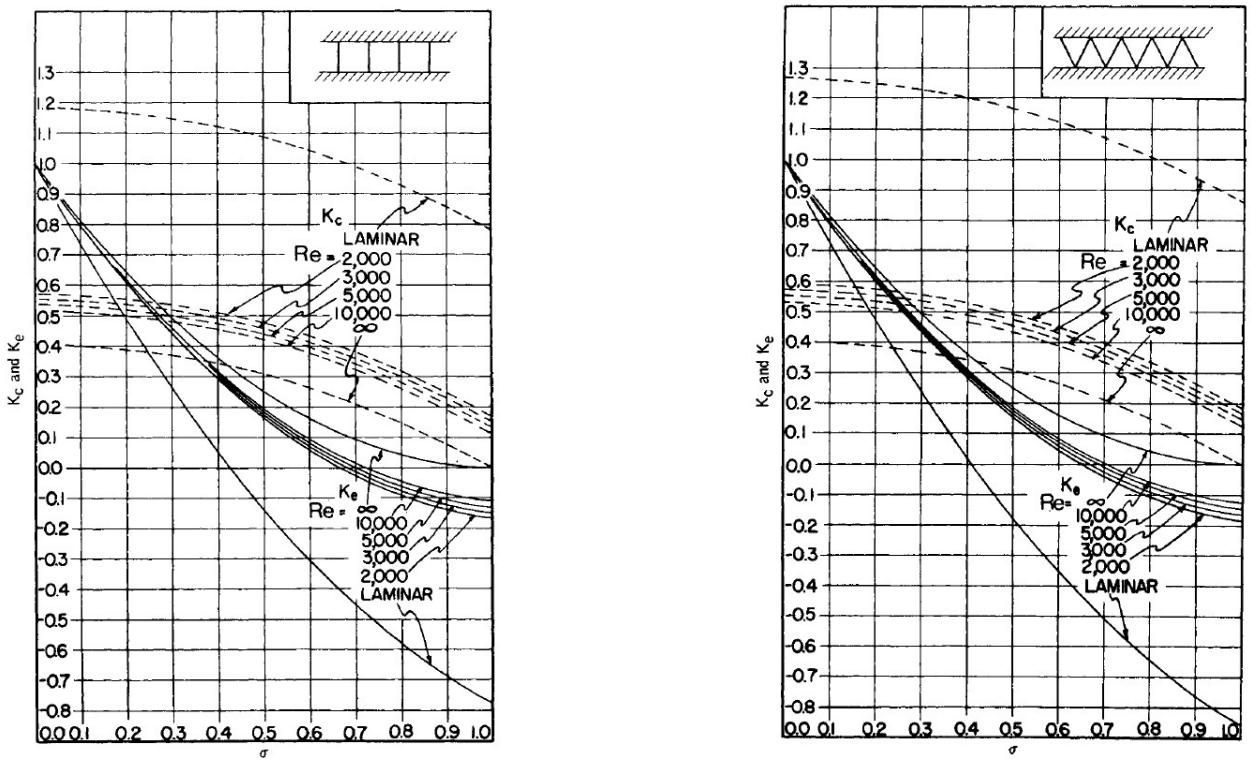

(a) (b)

Figure 4.2: Entrance and exit pressure-loss coefficients for heat exchangers with fin surfaces with (a) square cross-section, (b) triangular cross-section. Taken from [15]

For liquids

$$\frac{Nu}{Nu_{\mathrm{cp}}} = \left(\frac{\mu_{\mathrm{w}}}{\mu_{\mathrm{m}}}\right)^{n} \qquad \frac{f}{f_{\mathrm{cp}}} = \left(\frac{\mu_{\mathrm{w}}}{\mu_{\mathrm{m}}}\right)^{m} \tag{4.18}$$

The subscripts 'cp' in Eqs.4.17 and 4.18 refers to constant properties, and the exponents 'n' and 'm' are defined in Tab.4.1.

Fluid	Heating	Cooling
Gas	n = 0, m = 1	n = 0, m = 0.81
Liquid	n = -0.14, m = 0.58	n = -0.14, m = 0.54

Table 4.1: Exponents of property ratios of Eqs.4.17 and 4.18 for laminar flow [21].

Furthermore, the wall temperature T_{w} can be evaluated following the thermal-circuit approach. Neglecting fouling effects, the wall temperature is determined by the following equation:

$$T_{\mathrm{w}} = \frac{(T_{\mathrm{h,m}}/R_{\mathrm{h}}) + (T_{\mathrm{c,m}}/R_{\mathrm{c}})}{(1/R_{\mathrm{h}}) + (1/R_{\mathrm{c}})}. \tag{4.19}$$

Here, the resistances R_{h} and R_{c} are defined by Eqs.3.9, 3.10, and 3.11.
The determination of the pressure drops ΔP allows to calculate and, consequently, update the outlet pressures. The new outlet pressures and temperatures are evaluated as:

$$P_{\mathrm{o_c}} = P_{\mathrm{i_c}} - \Delta P_{\mathrm{c}}, \qquad P_{\mathrm{o_h}} = P_{\mathrm{i_h}} - \Delta P_{\mathrm{h}}, \tag{4.20}$$

$$T_{\mathrm{o_c}} = T_{\mathrm{i_c}} + \epsilon \left(\frac{C_{\min}}{\dot{m}_{\mathrm{c}} c_{\mathrm{p_c}}}\right)(T_{\mathrm{i_h}} - T_{\mathrm{i_c}}), \qquad T_{\mathrm{o_h}} = T_{\mathrm{i_h}} + \epsilon \left(\frac{C_{\min}}{\dot{m}_{h} c_{\mathrm{p_h}}}\right)(T_{\mathrm{i_h}} - T_{\mathrm{i_c}}). \tag{4.21}$$

With the updated outlet pressures and temperatures, is possible to evaluate the two respective residuals as:

$$res_{\mathrm{P_o}} = \left| \frac{P_{\mathrm{o_h}} - P_{\mathrm{o_{h,iter}}}}{P_{\mathrm{o_{h,iter}}}} \right| + \left| \frac{P_{\mathrm{o_c}} - P_{\mathrm{o_{c,iter}}}}{P_{\mathrm{o_{c,iter}}}} \right| \tag{4.22}$$

$$res_{\mathrm{T_o}} = \left| \frac{T_{\mathrm{o_h}} - T_{\mathrm{o_{h,iter}}}}{T_{\mathrm{o_{h,iter}}}} \right| + \left| \frac{T_{\mathrm{o_c}} - T_{\mathrm{o_{c,iter}}}}{T_{\mathrm{o_{c,iter}}}} \right| \tag{4.23}$$

These residuals express the relative error of the current and previous iteration values of outlet pressures ($P_{\mathrm{o_{h,iter}}}$ and $P_{\mathrm{o_{c,iter}}}$) and temperatures ($T_{\mathrm{o_{h,iter}}}$ and $T_{\mathrm{o_{c,iter}}}$). If the $res_{\mathrm{T_o}}$ is smaller than the tolerance *tol*, the convergence condition is met and the convergence loop is broken. The outlet pressures and temperatures will have the values of the current iteration, denoted with the subscript 'iter'.
With the updated values of thermodynamics parameters and effectiveness, it is possible to evaluate the actual value of the heat duty $\dot{Q}$ following Eq.3.13. Furthermore, the evaluation of velocities and of the Reynolds numbers on both sides is made with the following equations:

$$u_{(\mathrm{i,o})_c} = \frac{G_c}{\rho_{(\mathrm{i,o})_c}} \qquad u_{(\mathrm{i,o})_h} = \frac{G_h}{\rho_{(i,o)_h}}, \tag{4.24}$$

$$Re_{(\mathrm{i,o})_c} = \frac{G_c \; d_{h_c}}{\mu_{(\mathrm{i,o})_c}} \qquad Re_{(\mathrm{i,o})_h} = \frac{G_h \; d_{h_h}}{\mu_{(\mathrm{i,o})_h}}. \tag{4.25}$$

Then, the mean velocity is calculated as:

$$u_{m_c} = \frac{1}{2}\left(u_{i_c} + u_{o_c}\right) \qquad u_{m_h} = \frac{1}{2}\left(u_{i_h} + u_{o_h}\right). \tag{4.26}$$

The last step of the rating process is the estimation of the heat exchanger mass M_{hex}, which consists of the plates mass, core mass, and fluids mass. The plates mass is given by:

$$M_w = \rho_w \left(t_w \; z \; x\right)\left(n_p + 1\right). \tag{4.27}$$

The core mass M_{st} takes into account the structure mass of both sides, which can be calculated using the following equations:

$$M_{\mathrm{st}} = \rho_w \left(n_{\mathrm{p_{couple}}} \; F_h \; x \; z\right)\left(1 - \phi\right), \tag{4.28}$$

where the geometric parameters refer to the side considered. The term $n_{\mathrm{p_{couple}}}$ is the number of the couples of plates, which is half of the total number of plates n_p calculated earlier. Meanwhile, ϕ is the structure porosity, defined as the ratio of the minimum free-flow area over the frontal area:

$$\phi = \frac{A_0}{A_{\mathrm{fr}}}. \tag{4.29}$$

Looking at Eq.4.29, is possible to note that this parameter is strongly dependent on the fin type adopted on the fluid side considered.
The mass of the fluids considers the fluid mass of both sides too. These masses are defined by the following equation, where the geometric parameters refer to the side considered:

$$M_{\mathrm{fluid}} = \rho \; \phi \left(n_{\mathrm{p_{couple}}} \; F_h \; x \; z\right). \tag{4.30}$$

Furthermore, the total mass of the exchanger is evaluated by summing the contributions presented in Eqs.4.27, 4.28, and 4.30:

$$M_{\mathrm{hex}} = M_w + M_{\mathrm{st_c}} + M_{\mathrm{st_h}} + M_{\mathrm{fluid_c}} + M_{\mathrm{fluid_h}}. \tag{4.31}$$

Moreover, the heat exchanger volume V_{hex} is easily evaluated as:

$$V_{\mathrm{hex}} = x \; y \; z \tag{4.32}$$

4.2 Verification

In the previous section, the rating process utilized in this study was delineated. After its implementation in Python code, it is necessary to proceed with its verification. The methodology described in Ch.4.1 necessitates its verification through multiple test cases sourced from scientific literature, thereby ensuring its accurate functionality. However, the heat exchanger rating code will be tested with the parameters of already existing cases. Then, the resultant output values from the current rating will be compared with the corresponding values of the test case under consideration, showing the relative deviations. The verification process may be considered successful if, across multiple test cases from scientific literature, the deviations obtained in the output are negligible and/or attributable to simplifications employed or to different approaches.
The relative deviations are defined as Eq.2.46, where, x represents the generic output variable, the subscript 'cur' denotes the values of the current work, and the subscript 'ref' refers to the reference values. The rating variables considered for the comparison with the reference test cases are the heat duty $\dot{Q}$, the two pressure drops ΔP_{c} and ΔP_{h}, and the two Reynold numbers Re_{c} and Re_{h}. Thus, the relative deviations have been plotted, as points, in rating verification maps, as shown in Fig.4.4. Here, along the horizontal axis have been reported the five output variables, meanwhile, the vertical axis shows the ratio of variables from present work over variables from references $x_{\mathrm{cur}}/x_{\mathrm{ref}}$. This plotting setup allows having a comprehensive view of all points analyzed.

The proposed verification procedure will compare the test cases enumerated in Tab.4.2 with the developed rating tool. In addition, all parameters of all test cases are listed in Tab.4.3.

	Test Case (air-air)	**From**
1.	osf - osf	Shah and Sekulić [2003]
2.	osf - osf	Yousefi et al. [2012]
3.	osf - osf	Yousefi et al. [2012]
4.	osf - osf	Kakac and Liu [2002]
5.	osf - osf	EchTherm software
6.	rwf - rwf	EchTherm software

Table 4.2: References of test cases used for the rating verification

It is worth noting that in Tab.4.2, test cases 2 and 3 share the same reference. Test case number 2 refers to a Yousefi et al. [2012] test case that was optimized using a hybrid GA optimization algorithm, as described in the reference. On the other hand, test case number 3 represents a Yousefi et al. [2012] test case that was optimized using the reference approach.

Some test cases listed in Tab.4.2, adopt different simplifications, rating approaches, or utilize different correlations. The main differences between these cases and the current approach are outlined below:

- Shah and Sekulić [2003] employ experimental values of the j and f factors listed in Kays and London [2018];
- Yousefi et al. [2012] and Kakac and Liu [2002] consider the number of cold passages $N_{\mathrm{p_c}}$ to be one more than those of hot passages $N_{\mathrm{p_h}}$:

$$N_{\mathrm{p_c}} = N_{\mathrm{p_h}} + 1;$$

- in Yousefi et al. [2012] and Kakac and Liu [2002] the thermal resistance of the wall R_w is neglected;

- Yousefi et al. [2012] and Kakac and Liu [2002] use a simplified pressure drop equation that only takes into account the core contribution and assumes a constant density:

$$\Delta P = 2\frac{f\ L\ G^2}{\rho\ d_{\mathrm{h}}};$$

- there is no correction applied to friction factors in Yousefi et al. [2012] and Kakac and Liu [2002].

In addition to these assumptions and simplifications, the deviation between the current results and the reference results is given by the utilization of a different method for evaluating fluid properties. Furthermore, in relation to the test case from Kakac and Liu [2002], it should be noted that the thermal conductivity of the structure (fins and plate), denoted as k_{st}, is not provided. Consequently, it was assumed to be the thermal conductivity of Inconel718, which is 11.4 $W/(mK)$. The structure's thermal conductivity affects the fin efficiency evaluation and its impact on the rating was examined by varying its value. Fig.4.3 illustrates the behavior of the deviations in the considered output variables as the thermal conductivity increases, with k_{st} $= 6,\ 7,\ 8,\ 9,\ 10,\ 11.4\ W/(mK)$.

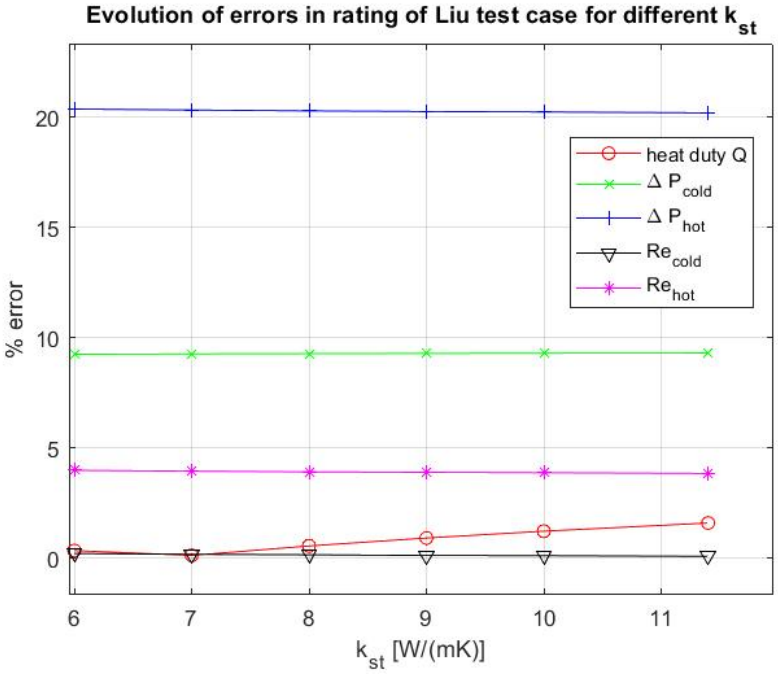

Figure 4.3: Effect of different structure thermal conductivity k_{st} on the deviations of rating verification with Kakac and Liu [2002].

Examining Fig.4.3, it becomes evident that, for the majority of the analyzed output parameters, the percentage error in the rating verification does not exhibit significant variations when the thermal conductivity of the structure k_{st} is modified. Just the error associated with the heat duty $\dot{Q}$ shows a bit increase as the thermal conductivity increases, eventually reaching a value of 1.44%.

The simple verification of the rating tool, presented in Fig.4.4, shows that the discrepancy between the parameters predicted through the current method and their actual values from the references are, in most cases, very low and negligible. Especially, the deviations of the heat duty and of both Reynold numbers do not exceed the 5%. At the same time, the two pressure drops evaluated with this method do not always show full congruence with reference values. In particular, their deviations with respect to cases 2, 3, and 4 of Tab.4.2 reach significant discrepancies of 28.81%, 28.11%, and 20.18% respectively (see Fig.4.4b, 4.4c, and 4.4d). The first two represent the error on the pressure drop of the cold side, and the third one is the error on the pressure losses of the hot

side. The discrepancies between the prediction of the developed rating tool and the reference test cases can be explained by the simplifications adopted by the references listed above, and possibly by the different employed rating methodology or accuracy. Furthermore, in these three cases, the other parameters show very small and tolerable deviations. To conclude, taking into account that the significant discrepancies of the verification can be well justified and that, generally, the verification returned good results, this tool can be adopted for rating exchangers that follow the assumptions of Ch.3.

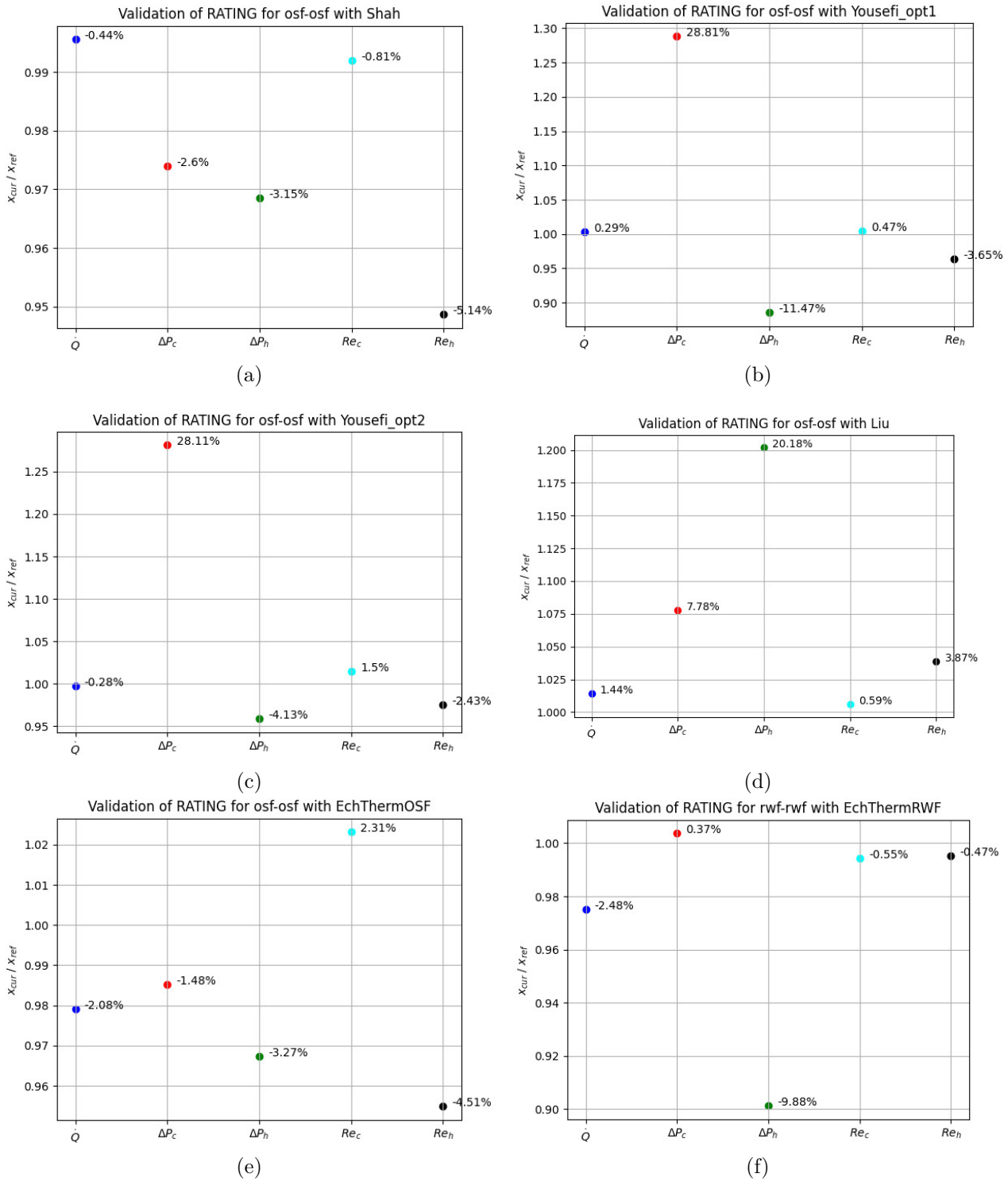

Figure 4.4: Verification maps for current rating compared with test case from: (a) Shah and Sekulić [2003], (b) Yousefi et al. [2012] using a hybrid GA optimization algorithm, (c) Yousefi et al. [2012] using the optimization of reference approach, (d) Kakac and Liu [2002], (e) EchTherm software for a 'osf-osf' heat exchanger, (f) EchTherm software for a 'rwf-rwf' heat exchanger

General heat exchanger parameters								
Test case	x [m]	y [m]	z [m]	$\dot{Q}$ [kW]	ΔP_c [Pa]	ΔP_h [Pa]		
Shah and Sekulić [2003]	0.3	1	0.3	1083.8	8790	9050		
Yousefi et al. [2012]	0.21	1.18	0.23	1069.8	8000	9500		
Yousefi et al. [2012]	0.20	1.26	0.21	1069.8	7960	9440		
Kakac and Liu [2002]	0.9	1.79	1.8	3300	10000	15000		
Greth EchTherm software with *osf* - *osf*	0.25	0.3815	0.25	68.7	6966	5619		
Greth EchTherm software with *rwf* - *rwf*	0.41	0.4055	0.4	64.65	6887	6842		
	Re_c	Re_h	T_{i_c} [K]	T_{i_h} [K]	P_{i_c} [bar]	P_{i_h} [bar]	$\dot{m}_c$ [kg/s]	$\dot{m}_h$ [kg/s]
Shah and Sekulić [2003]	842	589	200	900	2	1.6	2	1.66
Yousefi et al. [2012]	880.5688	565.2938	200	900	2	1.6	2	1.66
Yousefi et al. [2012]	854.7691	572.6588	200	900	2	1.6	2	1.66
Kakac and Liu [2002]	3000	1534	300	460	8.882	0.986	25	25.4
Greth EchTherm software with *osf* - *osf*	5721	6309	15	100	1	2	1.4	1.7
Greth EchTherm software with *rwf* - *rwf*	3221	3569	15	100	1	2	1.4	1.6

Geometrical fins parameters								
	F_p [mm]	F_h [mm]	l_s [mm]	t_f [mm]	λ [mm]	$2A$ [mm]	d_h [mm]	β [1/m]
Shah and Sekulić [2003]	1.1768	2.49	3.18	0.102			1.54	2254
Yousefi et al. [2012]	1	5.49	2.1	0.1			1.49	2379
Yousefi et al. [2012]	1	6.7	1.7	0.1			1.5	2370.1
Kakac and Liu [2002]	2	5.9	6	0.15			2.7	1322.9
Greth EchTherm software with *osf* - *osf*	2	12.1	2.3	0.1			3.345	
Greth EchTherm software *rwf* cold	2.272	8.1		0.1	9	2	3.417	
Greth EchTherm software *rwf* hot	2.1	7.1		0.1	12	3	3.111	

Table 4.3: Geometric and thermodynamic parameters of test cases used in rating and sizing verification.

Chapter 5

Heat exchanger sizing

The sizing process focuses on the evaluation of the heat exchanger size (width x, height y, and length z) given the thermodynamic operating conditions, with a consequent determination of its mass and pressure drops. The required thermodynamic input parameters for the sizing process are the inlet pressures and temperatures for both streams, the mass flow rates, and the heat duty. Additionally, the method requires as input the heat exchanger core geometry, its materials, and the flow arrangement or configuration.
Heat exchanger sizing represents a fundamental step in the design process, mainly in the design of recuperators for aerospace applications: sizes and mass are very important aspects to take into account in the heat exchanger design. Reducing the mass of heat exchangers allows to reduce the cost and the environmental footprint. For these reasons, this work is focused on the optimization of heat exchanger sizing (as depicted in Ch.1), and the sizing approach is following presented.

5.1 Methodology

The heat exchanger sizing method presented here is based on Shah and Sekulić [2003] approach and has been implemented as a routine in Python.
This sizing process is based on a convergence loop which can be set to converge on the outlet pressures or on the mean Reynolds numbers. Furthermore, in order to reach a better convergence to the actual values, there is also the chance to perform a sizing imposing the height of the exchanger. The fundamental steps of this sizing approach are shown in Fig.5.1, and the functioning of the converge loop and of the sizing with imposed height, will be depicted below.

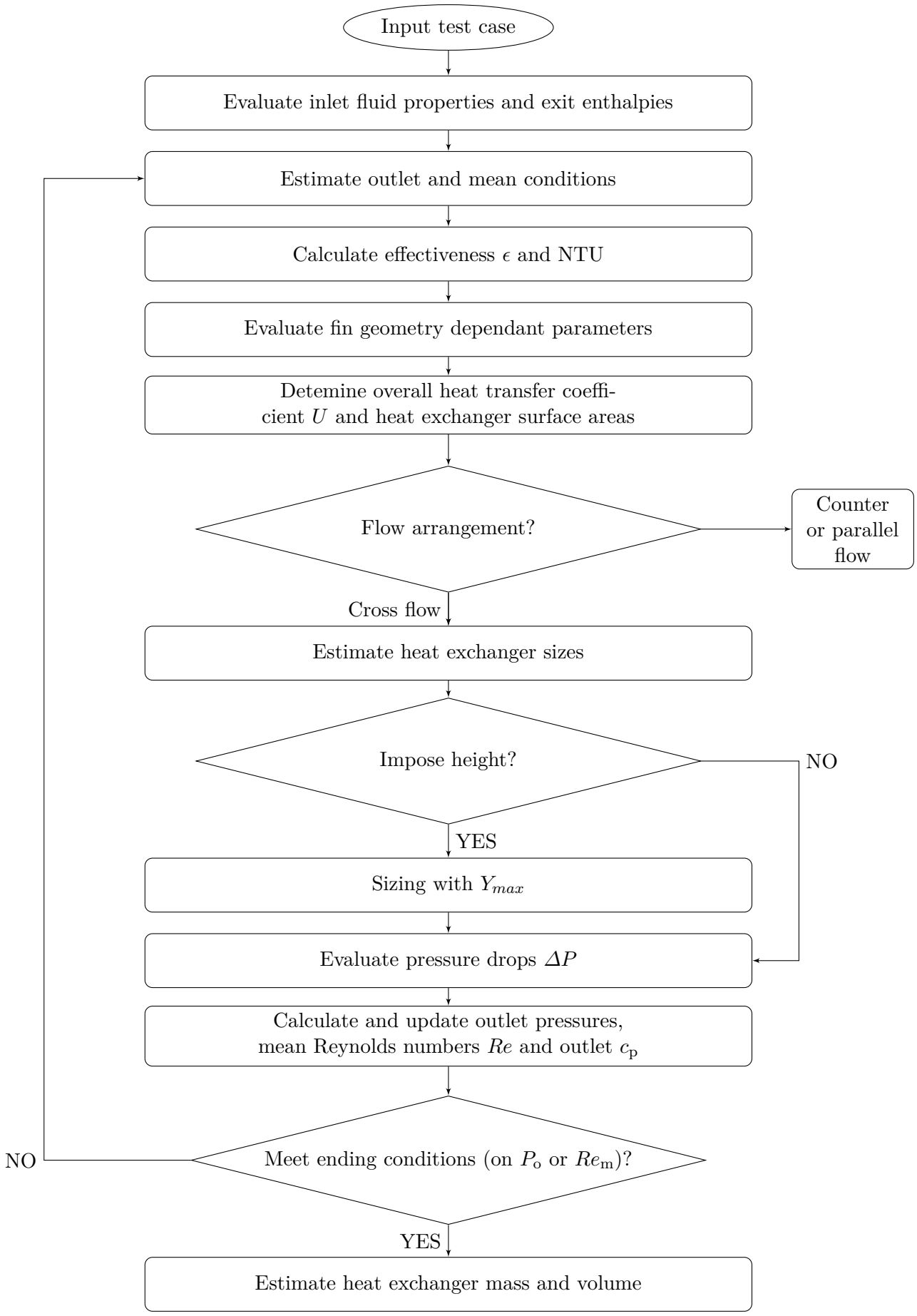

Figure 5.1: Flow chart for heat exchanger sizing.

The sizing process begins with the evaluation of inlet fluid properties for both sides, such as density ρ, thermal conductivity k, dynamic viscosity μ, c_p, and enthalpy H. Then, the exit enthalpies are evaluated as follows:

$$H_{\mathrm{o_c}} = H_{\mathrm{i_c}} + \frac{\dot{Q}}{\dot{m}_\mathrm{c}} \qquad\qquad H_{\mathrm{o_h}} = H_{\mathrm{i_h}} - \frac{\dot{Q}}{\dot{m}_\mathrm{h}} \tag{5.1}$$

The exit enthalpies are calculated to evaluate the outlet fluid properties since the outlet temperatures are unknown.
In order to proceed with the sizing, it is necessary to impose the first guess values of the outlet pressures and the mean Reynolds numbers. In this thesis, the outlet pressures are supposed to be the 90% of the inlet pressures, meanwhile, the mean Reynolds numbers are optimization variables of the design optimizer (see 6). In order to achieve convergence towards the appropriate values, the following process will be repeated until the ending conditions are met. The loop terminates when the residual of the outlet pressures ($res_{\mathrm{P_o}}$) or the residual of the outlet c_p (res_{fp}) exceeds the specified tolerance (tol), or when the number of iterations (n_{iter}) exceeds the maximum number of iterations (max_{iter}). It is also possible to set the convergence toward the Reynolds numbers. In this case, the ending criteria are the same, except for the condition on the outlet pressures is replaced by the one on the Reynolds numbers: the loop terminates if the residual of mean Re (res_{Re}) exceeds the tolerance. Whatever the type of converge loop chosen, both the outlet pressures and the mean Reynolds numbers are updated before restarting another loop. The values of tolerance and of the maximum number of iterations are arbitrarily determined and, for this work, have been imposed as $tol = 1e-4$ and $max_{\mathrm{iter}} = 20$.

In every iteration, the following steps will be followed. Using the current values of enthalpies and pressures, the fluid properties can be evaluated both in the mean and outlet sections. The estimation of mean c_p allows to evaluate the outlet and, thus, mean temperatures using Eq.3.13, specifying it for each fluid side as $\dot{Q} = \dot{m} c_\mathrm{p} \Delta T$, where c_p is the one in the mean section of the fluid side. Therefore, by rewriting this heat duty equation, it is possible to evaluate the outlet temperatures as follows:

$$T_{\mathrm{o_c}} = T_{\mathrm{i_c}} + \frac{\dot{Q}}{\dot{m}_\mathrm{c}\ c_{\mathrm{p_c}}} \qquad\qquad T_{\mathrm{o_h}} = T_{\mathrm{i_h}} - \frac{\dot{Q}}{\dot{m}_\mathrm{h}\ c_{\mathrm{p_h}}} \tag{5.2}$$

Moreover, using the mean c_p is possible to proceed with the determination of the effectiveness ϵ and, consequently, of the number of transfer units NTU. The heat exchanger effectiveness, as depicted in Eq.3.13, is dependent on the minimum heat capacity C_{min}. Moreover, the heat duty $\dot{Q}$ is the same in both the fluid side and its equation is

$$\dot{Q} = C_\mathrm{c}\ \Delta T_\mathrm{c} = C_\mathrm{h}\ \Delta T_\mathrm{h}, \tag{5.3}$$

where the heat capacity is $C = \dot{m}\ c_\mathrm{p}$. Consequently, choosing the fluid side with the minimum heat capacity, the effectiveness is determined by Eq.3.14 as follows:

$$\epsilon = \frac{C_{\mathrm{c,h}}\ \Delta T_{\mathrm{c,h}}}{C_{\mathrm{min}}\ \Delta T_{\mathrm{max}}} = \begin{cases} \frac{T_{\mathrm{o_c}} - T_{\mathrm{i_c}}}{T_{\mathrm{i_h}} - T_{\mathrm{i_c}}}, & \text{if } C_{\mathrm{min}} = C_\mathrm{c} \\ \\ \frac{T_{\mathrm{i_h}} - T_{\mathrm{o_h}}}{T_{\mathrm{i_h}} - T_{\mathrm{i_c}}}, & \text{if } C_{\mathrm{min}} = C_\mathrm{h} \end{cases} \tag{5.4}$$

Then, the number of transfers of units is calculated by solving iteratively Eq.3.19 for NTU. In order to solve this equation, the sizing tool, here depicted, uses the Python function 'fsolve', with a first value $NTU_0 = 1$.
The next steps are dependent on the fin geometries. Firstly, the fin geometric parameters are evaluated, as shown in Ch.2, for both fluid sides. Then, j and f factor are evaluated according to the correlations described in Ch.2. These two factors, then, leads to calculating the heat transfer coefficient h and, thus, the fin and surface efficiency.

The evaluation of the overall heat transfer coefficient U is made by using Eq.3.12. Following this equation, the term $\frac{1}{UA}$ is multiplied for the heat transfer area reaching the following equations:

$$\frac{1}{U_c} = \frac{1}{(\eta_0\ h)_c} + \frac{t_w\ A_c}{k_w\ A_w} + \frac{A_c/A_h}{(\eta_0\ h)_h}, \qquad \frac{1}{U_h} = \frac{1}{(\eta_0\ h)_h} + \frac{t_w\ A_h}{k_w\ A_w} + \frac{A_h/A_c}{(\eta_0\ h)_c}. \tag{5.5}$$

Here, the variables α are the compactness, defined in Eq.2.4, and the ratio of the two compactness is $\alpha_c/\alpha_h = A_c/A_h$.Consequently, since the heat transfer areas are still unknown, the Eqs.5.5 are rewritten as:

$$\frac{1}{U_c} = \frac{1}{(\eta_0\ h)_c} + \frac{t_w\ A_c}{k_w\ A_w} + \frac{\alpha_c/\alpha_h}{(\eta_0\ h)_h}, \qquad \frac{1}{U_h} = \frac{1}{(\eta_0\ h)_h} + \frac{t_w\ A_h}{k_w\ A_w} + \frac{\alpha_h/\alpha_c}{(\eta_0\ h)_c}. \tag{5.6}$$

Once the overall heat transfer coefficient on one fluid side has been evaluated, the U on the other side can be evaluated, following the Eqs.5.6, as

$$\frac{1}{U_c} = \frac{1}{U_h}\ \frac{\alpha_c}{\alpha_h}. \tag{5.7}$$

Knowing the overall heat transfer coefficients is possible to calculate the heat exchanger surface areas, such as the heat transfer area A, the minimum free-flow area A_0, and the frontal area A_{fr}:

$$A = \frac{NTU\ C_{min}}{U} \tag{5.8}$$

$$A_0 = \frac{\dot{m}}{G} \tag{5.9}$$

$$A_{fr} = \frac{A_0}{\sigma} \tag{5.10}$$

Where the term G is calculated with Eq.4.10.
After having evaluated all the geometrical and thermodynamic parameters, it is possible to determine the dimensions of the heat exchanger. This step is dependent on the flow arrangement and, thus, needs a different procedure for each flow arrangement. With a cross-flow configuration, the two flow lengths x and z (width and length of the exchanger respectively) can be easily evaluated by using the definition of hydraulic diameter (see Eq.2.1) as depicted below:

$$x = \frac{d_{h_c} A_c}{4A_{0_c}}, \tag{5.11}$$

$$z = \frac{d_{h_h} A_h}{4A_{0_h}}. \tag{5.12}$$

Consequently, the height of the exchanger is evaluated using the definition of the frontal area A_{fr}:

$$y = \frac{A_{fr_c}}{x} = \frac{A_{fr_h}}{z}. \tag{5.13}$$

It is important to highlight that this sizing has been made not knowing any exchanger dimensions. On the other hand, as depicted above, there is a chance to evaluate the length and the width of the heat exchanger imposing its height.

The basics steps of this sizing are shown in the flow chart of Fig.5.2. If the option of imposed height is chosen, the HX height y is forced to be $y = Y_{max}$, where Y_{max} is the maximum value for the height, different for each test case. Once the height has been imposed, the next fundamental step is to evaluate the two Reynolds numbers that enable to have $y = Y_{max}$. Imposing to have the same height on both sides and starting from Eq.5.13, it is possible to derive the equation that relates the

two Reynolds numbers to the heat exchanger height. Firstly, Eq.5.13 is rewritten using the frontal area A_{fr} definition (Eq.5.10) as

$$y = \frac{A_{\mathrm{fr_h}}}{z} = \frac{A_{0_\mathrm{h}}}{\sigma_h \; z}.$$

Then, through the flow length equations (Eqs.5.11 and 5.12) and the minimum free-flow area A_0 definition (Eq.5.9) the height equation is expressed as

$$y = \frac{A_{0_\mathrm{h}} \; 4 \; A_{0_\mathrm{c}}}{\sigma_h \; d_{\mathrm{h_h}} \; A_h} = \frac{16 \; \dot{m}_\mathrm{h} \; d_{\mathrm{h_h}} \; \dot{m}_\mathrm{c} \; d_{\mathrm{h_c}}}{\sigma_h \; d_{\mathrm{h_h}} \; A_c \; Re_\mathrm{h} \; \mu_\mathrm{h} \; Re_\mathrm{c} \; \mu_\mathrm{c}}.$$

Finally, the definitions of hydraulic diameter d_h (Eq.2.1), of heat transfer area (Eq.5.8), and of compactness α (Eq.2.4), enable to rewrite the equation as

$$y = \frac{16 \; \dot{m}_\mathrm{h} \; \dot{m}_\mathrm{c} \; U_c}{\alpha_\mathrm{h} \; Re_\mathrm{h} \; \mu_\mathrm{h} \; Re_\mathrm{c} \; \mu_\mathrm{c} \; NTU \; C_{\mathrm{min}}}. \tag{5.14}$$

Eq.5.14 can be reword as

$$(y \; Re_\mathrm{c} \; \mu_\mathrm{c} \; Re_\mathrm{h} \; \mu_\mathrm{h} \; NTU \; C_{\mathrm{min}} \; \alpha_\mathrm{h}) - (16 \; \dot{m}_\mathrm{c} \; \dot{m}_\mathrm{h} \; U_\mathrm{c}) = 0, \tag{5.15}$$

which can be solved using a gradient-based method to find the cold side Reynolds number. On the other hand, the Reynold number on the hot side Re_h is evaluated from the Re_c. The ratio of Re_h over Re_c can be expressed as:

$$\frac{Re_\mathrm{h}}{Re_\mathrm{c}} = \frac{\dot{m}_\mathrm{h} \; d_{\mathrm{h_h}} \; A_{0_\mathrm{c}} \; \mu_\mathrm{c}}{\dot{m}_\mathrm{c} \; d_{\mathrm{h_c}} \; A_{0_\mathrm{h}} \; \mu_\mathrm{h}} = \frac{\dot{m}_\mathrm{h} \; 4 \; \sigma_h \; \alpha_\mathrm{c} \; A_{0_\mathrm{c}} \; \mu_\mathrm{c}}{\dot{m}_\mathrm{c} \; 4 \; \sigma_c \; \alpha_\mathrm{h} \; A_{0_\mathrm{h}} \; \mu_\mathrm{h}} \tag{5.16}$$

thus, the hot side Reynolds is evaluated as:

$$Re_\mathrm{h} = Re_\mathrm{c} \frac{\dot{m}_\mathrm{h} \; \sigma_h \; \alpha_\mathrm{c} \; A_{0_\mathrm{c}} \; \mu_\mathrm{c}}{\dot{m}_\mathrm{c} \; \sigma_c \; \alpha_\mathrm{h} \; A_{0_\mathrm{h}} \; \mu_\mathrm{h}}. \tag{5.17}$$

At each iteration to solve Eq.5.15, both the Reynolds numbers and all the parameters dependent on them, are updated. Then, when the convergence is reached, the steps from Eq.5.9 to Eq.5.12 are repeated in order to make the sizing.

After the evaluation of heat exchanger sizes, the following step is the determination of the pressure drops ΔP. In order to evaluate the pressure drops, the same process described in Ch.4.1 is used, with the same equations (see from Eq.4.14 to 4.19).
Lastly, with the pressure drops is possible to evaluate the current outlet pressures as Eq.4.20 and, consequently, the current mean Reynolds numbers as:

$$Re_\mathrm{c} = \frac{u_{\mathrm{m_c}} \; \rho_{\mathrm{m_c}} \; d_{\mathrm{h_c}}}{\mu_{\mathrm{m_c}}}, \qquad Re_\mathrm{h} = \frac{u_{\mathrm{m_h}} \; \rho_{\mathrm{m_h}} \; d_{\mathrm{h_h}}}{\mu_{\mathrm{m_h}}}. \tag{5.18}$$

Then, the residuals on outlet pressures and mean Reynolds numbers are calculated as:

$$res_{\mathrm{P_o}} = \left| \frac{P_{\mathrm{o_h}} - P_{\mathrm{o_{h,iter}}}}{P_{\mathrm{o_{h,iter}}}} \right| + \left| \frac{P_{\mathrm{o_c}} - P_{\mathrm{o_{c,iter}}}}{P_{\mathrm{o_{c,iter}}}} \right| \tag{5.19}$$

$$res_{\mathrm{Re_m}} = \left| \frac{Re_{\mathrm{m_h}} - Re_{\mathrm{m_{h,iter}}}}{Re_{\mathrm{m_{h,iter}}}} \right| + \left| \frac{Re_{\mathrm{m_c}} - Re_{\mathrm{m_{c,iter}}}}{Re_{\mathrm{m_{c,iter}}}} \right| \tag{5.20}$$

These residuals express the relative error of the current and previous iteration values of outlet pressures ($P_{\mathrm{o_{h,iter}}}$ and $P_{\mathrm{o_{c,iter}}}$) and mean Reynolds numbers ($Re_{\mathrm{m_{h,iter}}}$ and $Re_{\mathrm{m_{c,iter}}}$). As for the rating process, the subscript 'iter' refers to the parameters of the current iteration. Then, the outlet pressures and the mean Reynolds numbers are updated.

It is worth noting that if one of the two fluid sides is made of triangular wavy fins, the geometry can be completely defined after the exchanger sizing. The TWF geometry have been defined in Ch.2.2.2 also by the ratio $\zeta = L/\lambda$, where L is the flow length. Consequently, at the end of the sizing process, the fin wavelength λ is evaluated as:

$$\lambda_c = \frac{z}{\zeta_c} \qquad \lambda_h = \frac{x}{\zeta_h} \tag{5.21}$$

Once the convergence loop ends, the evaluation of velocities and of the Reynolds numbers on both sides is made using the Eqs.4.24, 4.25, and 4.26 showed in Ch.4.1. Furthermore, also the evaluation of heat exchanger mass and volume is made using the equations described in the rating process (see from Eq.4.27 to 4.32).

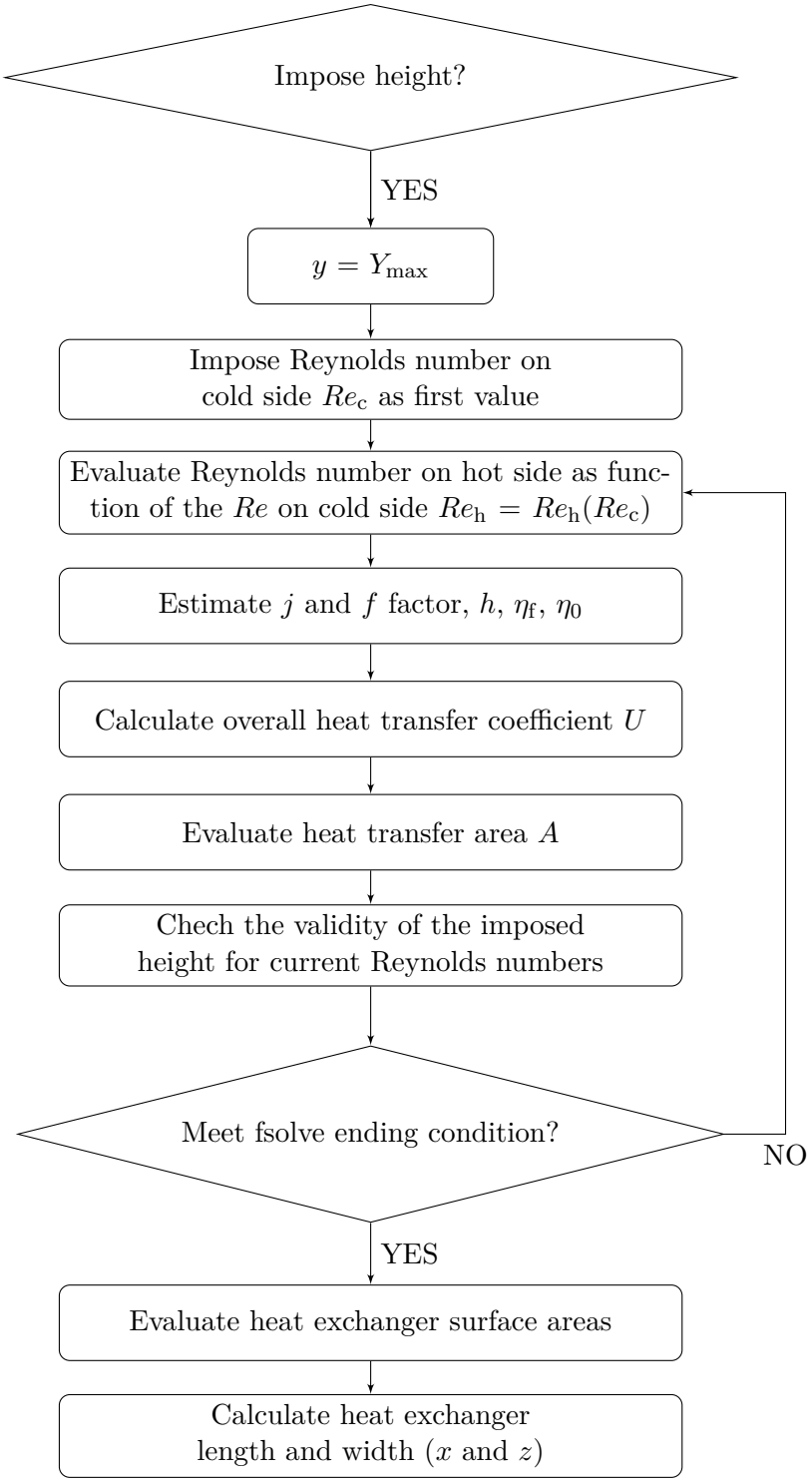

Figure 5.2: Flow chart for heat exchanger sizing imposing the height.

5.2 Verification

As discussed before for the rating, the sizing tool needs to be validated too. The verification process is precisely the same as the one presented in Ch.4.2.
The approach previously described will be used to size already existing cases from the scientific literature. Then, the outputs of this study will be compared with the actual parameters of the considered test cases. Thus, the sizing tool can be considered reliable if the differences between its results and the parameters of the test cases are low and/or can be explained with a different approach or with the employment of some assumptions.
In order to validate this sizing process, the parameters to compare are, obviously, different. Therefore, the verification will focus on comparing the two pressure drops ΔP, the two Reynolds numbers Re, the heat exchanger sizes (x, y, and z), and the exchanger volume V_{hex}. The verification maps in Fig.5.4, show the relative deviations, plotting the ratio of variables from present work over variables from references $x_{\text{cur}}/x_{\text{ref}}$ (along the vertical axis), for the eight parameters (on the x-axis). Fig.5.4 shows the verification of the sizing tool imposing the height and with the convergence loop on the outlet pressures.
The test cases used for this comparison are the same as Ch.4.2 and are listed in Tab.4.2, meanwhile all their parameters are shown in Tab.4.3. Consequently, the assumptions and the differences between these test cases and the present approach, are the same as described before.
It is worth noting that, as in the rating verification, the thermal conductivity of Kakac and Liu [2002] is not known. For this reason, has been studied the influence of thermal conductivity in the sizing process. As shown in Fig.5.3, differently from the rating, for different values of thermal conductivity, the sizing output parameters change significantly[1].

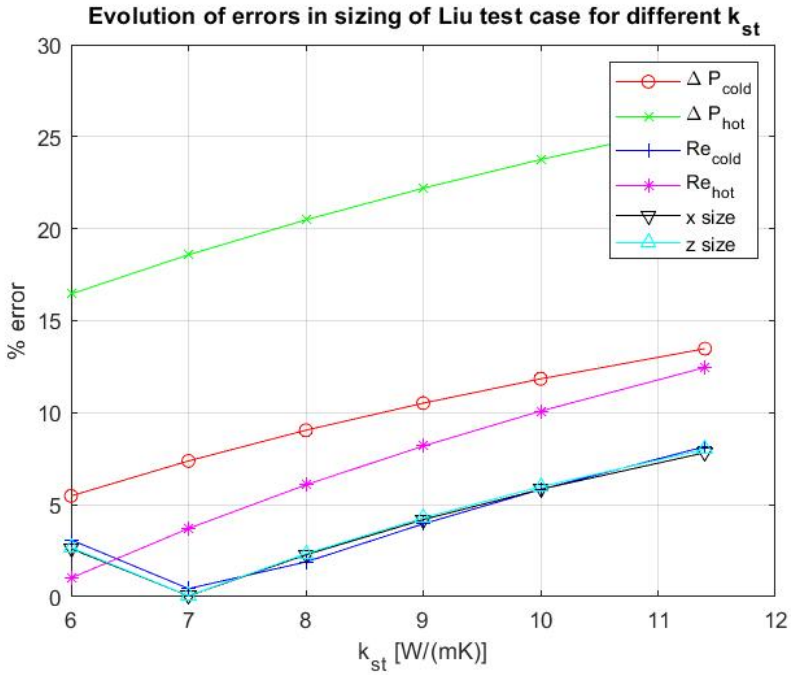

Figure 5.3: Effect of different structure thermal conductivity k_{st} on the relative deviations of sizing verification with Kakac and Liu [2002].

Fig.5.4 shows that the verification of the sizing tool returns good results, since the discrepancies of the sizes evaluated with this method from the values from references are very low, less than about 5%, in most cases. These deviations increase a bit up to about 8% in the verification made with the test case from Kakac and Liu [2002] (see Fig.5.4d). The reason behind these higher deviations is linked to the thermal conductivity whose value has been supposed, as has been previously explained,

[1] This plot shows the absolute value of the relative deviations.

and, probably, the reference uses a material with a different k_{cond}. As Fig.5.3 shows, decreasing the value of thermal conductivity the prediction of exchanger sizes reflects more the actual values. The same considerations can be made about the relative deviations on the two Reynolds numbers which reach about 7% maximum in the majority of cases, except in the Kakac and Liu [2002] test case where the percentages are 8.16% and 12.46%, respectively for Re_{c} and Re_{h}.
Concerning the evaluation of pressure drops, the comparison with Shah and Sekulić [2003] shows deviations less than 5% (see Fig.5.4a). Meanwhile, the verification made with the two test cases from Yousefi et al. [2012] (see Fig.5.4b, 5.4c) returns bigger relative deviations, especially those of the pressure drop on the cold side which are 30.97% and 27.61%. Furthermore, Fig.5.4d shows that also the comparison with Kakac and Liu [2002] returns big deviations for the pressure losses: 13.48% for the ΔP_{c} and 25.72% for the ΔP_{h}. These discrepancies are connected to a different approach of the reference and to its simplifications, already depicted in 4.2. Then, supposing the thermal conductivity for Kakac and Liu [2002], affects also the evaluation of the pressure losses, as depicted in Fig.5.3. To conclude, the developed sizing tool provides valid designs provided that the assumptions of 3 are met. It is also important to highlight that these results have been reached by imposing the height of the heat exchanger.

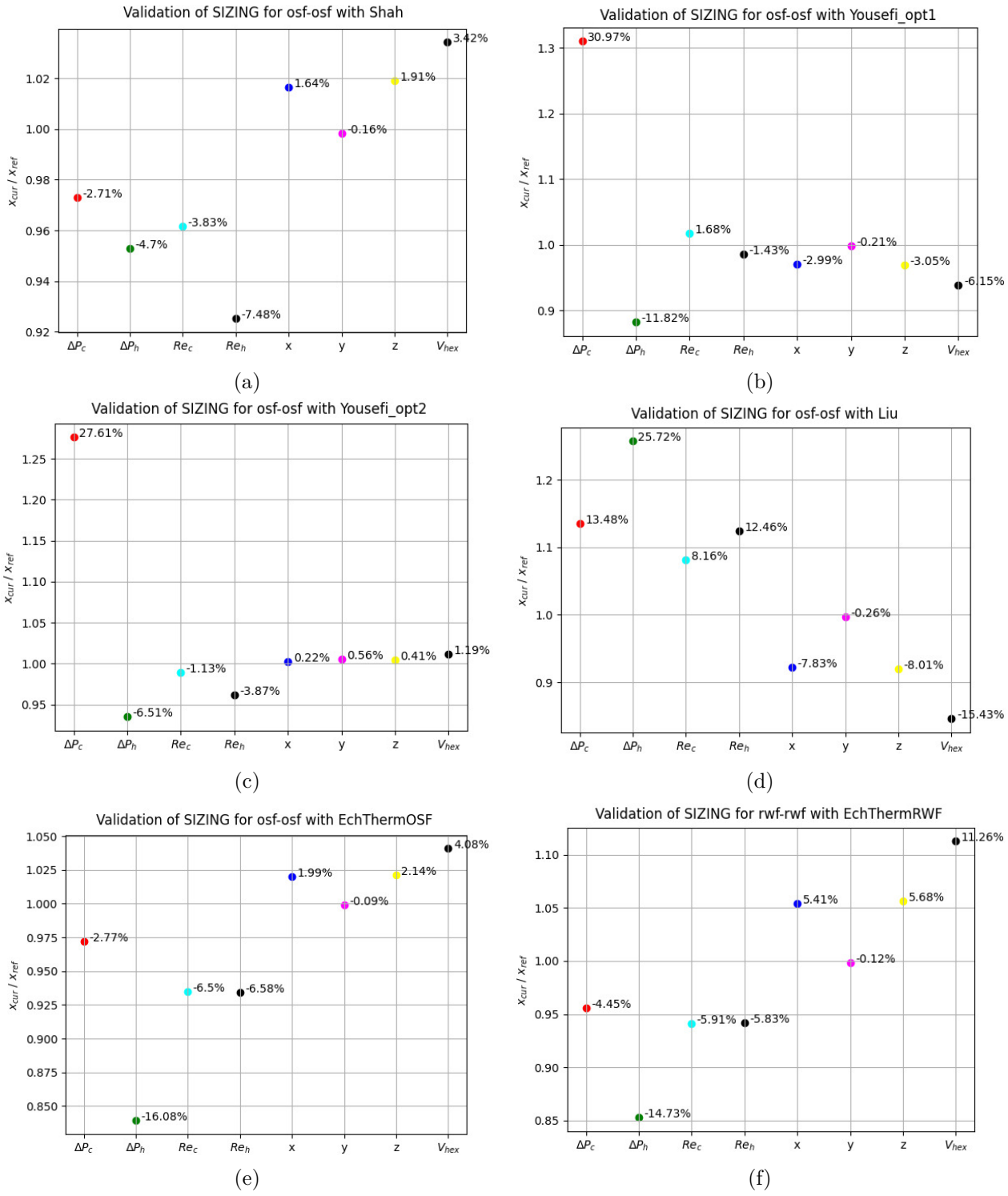

Figure 5.4: Verification maps for current sizing (imposing the height and with the convergence loop on the outlet pressures) compared with test case from: (a) Shah and Sekulić [2003], (b) Yousefi et al. [2012] using a hybrid GA optimization algorithm, (c) Yousefi et al. [2012] using the optimization of reference approach, (d) Kakac and Liu [2002], (e) EchTherm software for a 'osf-osf' heat exchanger, (f) EchTherm software for a 'rwf-rwf' heat exchanger

Chapter 6

Heat exchanger design optimization

The aim of this work is to find a good method that overcomes the limitations of the other methods outlined in Ch.1 for the selection of enhanced surfaces. In order to reach this objective, the work is focused on creating some optimized design maps which relate different performance metrics for multiple combinations of fin geometries on the two fluid sides.

6.1 Optimization algorithms

In order to perform the heat exchanger sizing optimization, a different tool has been implemented in the Python code, with the chance to choose between different optimization algorithms. For this work, the optimization variables are the two Reynolds numbers and the geometric input parameters. These geometric input parameters are different for each fin type (see Tab.6.1) and are the parameters on which is based the modeling of each geometry (see Ch.2). Since they are used as optimization variables, it is necessary to define their own validity bounds, which are listed in Tab.6.1.
The heat exchanger sizing optimization has been performed through different optimization algorithms: two single-objective algorithms (DEA and PSO), one multi-objective algorithm (NSGA-II), and one many-objective algorithm (NSGA-III). Here, the many-objective algorithm refers to optimization algorithms with more than two objective functions.
The single-objective optimization algorithms have just one objective function which, in this case, is to minimize the heat exchanger mass M_{hex}. On the other hand, multi and many-objective optimization algorithms have multiple objective functions. The multi-objective algorithm may minimize both the exchanger mass and the pressure drop on the hot side ΔP_{h}. Meanwhile, the many-objective algorithm has three different objective functions: the minimization of the exchanger mass and of both pressure drops. Below, each algorithm is briefly described.
The Differential Evolution Algorithm (DEA) starts with a target vector from the initial population of size N. At each generation, the mutant vector is created by combining three randomly elements from the population, as follows:

$$V = X_1 + F\,(X_2 - X_3)\,,$$

where F is a multiplier. Then, the crossover operation is applied between the target and the mutant vector, to generate the trial vector. If the trial vector has the best fitness, it will replace the target vector in the next generations (see Fig.6.1).

Fin geometry	Geometric input parameters	Validity bounds [min, max]	Reference
RPF	F_p F_h	[1.279e-3, 12.7e-3] [6.35e-3, 20.9e-3]	[15]
TPF	F_p F_h	[0.5468e-3, 2.4732e-3] [2.54e-3, 13.82e-3]	[15]
RWF	F_p F_h λ $2A$	[1.5e-3, 3.5e-3] [6e-3, 10e-3] [7e-3, 11e-3] [0.5e-3, 2.5e-3]	[15] and [1]
TWF	F_p F_h ζ $2A$	[0.71e-3, 1.75e-3] [6e-3, 10.5e-3] [3.9815, 9] [0.5e-3, 2.5e-3]	[15], [1], and [20]
OSF	α δ γ	[0.134, 0.997] [0.012, 0.048] [0.041, 0.121]	[18]
LF	L_α N_LB $F_\mathrm{l}/L_\mathrm{p}$ $F_\mathrm{d}/F_\mathrm{p}$ $L_\mathrm{h}/F_\mathrm{l}$ $t_\mathrm{f}/L_\mathrm{p}$ $F_\mathrm{p}/L_\mathrm{p}$	[8.4, 35.9] [1, 4] [2.6, 16] [5, 40] [0.63, 0.96] [0.025, 0.155] [0.45, 4.44]	[20]

Table 6.1: Geometric input parameters and their validity bounds for different fin types.

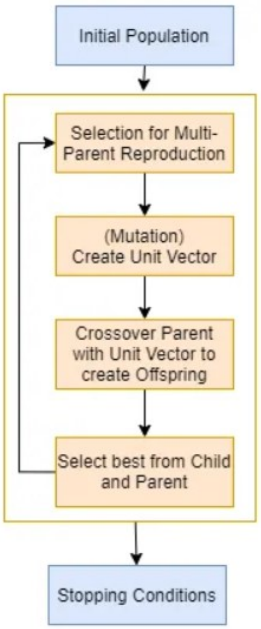

Figure 6.1: Flowchart of the Differential Evolution Algorithm DEA. Taken from [19]

The Particle Swarm Optimization (PSO) algorithm has been developed to simulate the behaviour of flocks of birds. Thus, the algorithm defines randomly an initial swarm of optimization variables of N size. Here, every set of optimal variables is called a particle and represents a potential solution of the optimized problem. Each individual is assigned randomly a position x_{i} and a velocity v_{i} that, in each generation, are updated with the following equations, in order to find the optimal values [Wang et al., 2017]:

$$v_{\mathrm{i,t+1}} = \omega \; v_{\mathrm{i,t}} + c_1 \; rand(p_{\mathrm{i,t}} - x_{\mathrm{i,t}}) + c_2 \; rand(p_{\mathrm{g,t}} - x_{\mathrm{i,t}}) \tag{6.1}$$

$$x_{\mathrm{i,t+1}} = x_{\mathrm{i,t}} + v_{\mathrm{i,t+1}} \tag{6.2}$$

Here ω is the inertia weight, p_{i} refers to the individual's optimal position, *rand* denotes a random number in [0,1], and p_{g} represents the swarm's optimal position. The entire process is outlined in the flowchart of Fig.6.2.

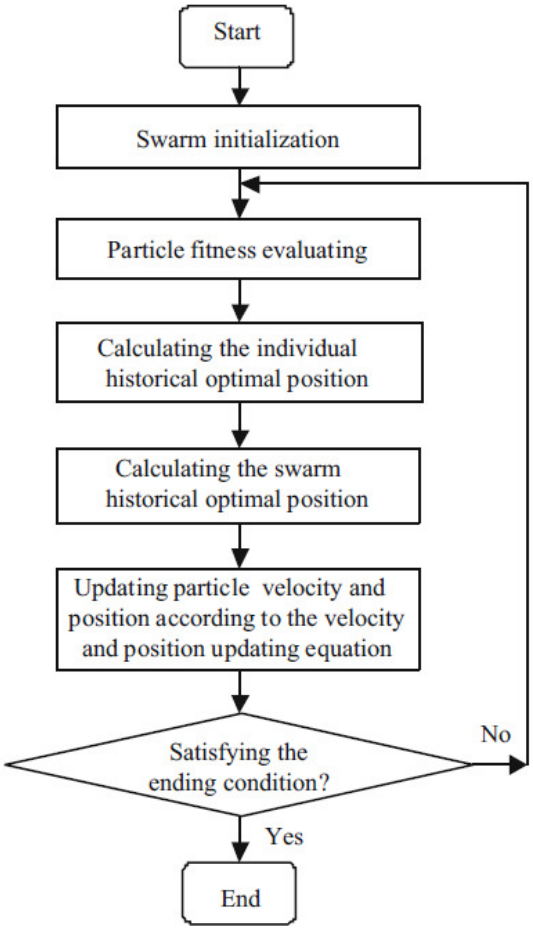

Figure 6.2: Flowchart of the Particle Swarm Optimization PSO algorithm. Taken from [26]

Analyzing Eq.6.1 it is possible to highlight that the first part is the contribution of the particle's previous velocity, the second term is the cognitive item and represents the distance between the particle's current position and its own optimal position, the third part is the distance between the particle's current position and the global optimal position and is known as social term.
In the Non-Sorted Genetic Algorithm II (NSGA-II), in order to satisfy multiple objectives, it is necessary to find a set of non-dominated optimal solutions, called Pareto Front. Following Deb [2002], the NSGA-II process is here described. Firstly, an initial population P_0 of size N is randomly created and is sorted based on the nondomination. A solution x_1 dominates another solution x_2 if it respects the following conditions:

- the $f_j(x_1)$ is better than $f_j(x_2)$ for all $j \in 1, 2, ..., M$, where f_j is the j^{th} objective function and M is the number of objectives;
- the solution $f_j(x_1)$ is strictly better than $f_j(x_2)$ in at least one objective.

Then, the initial population P_0 is modified through tournament selection, recombination, and mutation. Thus, the offspring population Q_0 of size N is defined.
Now, to ensure elitism [1], a combined population $R_t = P_t \cup Q_t$ of the generic iteration t is created, with $2N$ size. Then, the R_t population is sorted using the nondomination criteria. The set F_1 includes the best nondominated solutions of R_t and all elements of F_1 are used in the population of the next generation P_{t+1}. If the F_1 size is less than N, the remaining elements are chosen from the subsequent set. However, the selection, crossover, and mutation are applied on P_{t+1} to create the new population Q_{t+1}. Here, the selection is performed with a binary tournament selection based on the crowded-comparison operator. This process is outlined in Fig.6.3

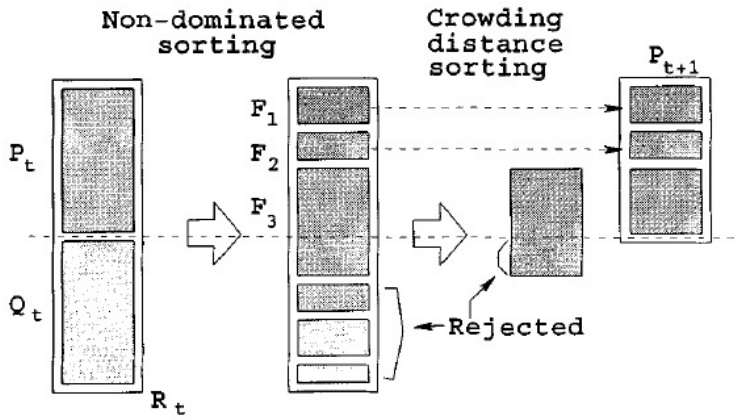

Figure 6.3: Process of the Non-Dominated Sorted Genetic Algorithm II. Taken from [7]

The base process of the Non-Sorted Genetic Algorithm III (NSGA-III) is the same as the NSGA-II but adapted for a many-objective algorithm and, in this case, the set of solutions is a 3D Pareto Front. The flowchart of Fig.6.4 shows the main steps of this algorithm. The main difference between NSGA-III and NSGA-II is the creation of P_{t+1} and it is outlined below, following Deb [2014].
The NSGA-III is based on the concept of reference points which, in the objective space, define the reference directions along which to search the solutions, ensuring diversity. In this work, the identification of reference points is performed with Das and Dennis's approach, which places points on a normalized hyper-plane equally inclined to all objective axes. The number of reference points is evaluated as

$$H = \binom{M + p - 1}{p}, \tag{6.3}$$

where M is the number of objective functions, and p is the number of partitions each objective is divided into. In this work, the H value is calculated with 'comb' function of scipy library. The next step is the association of each population member to a reference point, considering that the reference lines are defined by joining reference points with the origin. Thus, the reference point whose line is closest to a population member is associated with that member. Lastly, the new population P_{t+1} is created through the niche-preservation operation [Deb, 2014].
The optimization algorithms considered here have been implemented in the Python code using two different libraries. The two single-objective algorithms (DEA and PSO) and the multi-objective algorithm (NSGA-II) use the 'inspyred' library, meanwhile, the many-objective algorithm (NSGA-III) adopts the 'pymoo' library.
The inspyred library is based on three different functions, necessary to evaluate the fitness:

[1] This strategy enables to ensure the presence of the best chromosomes of a generation in the next one.

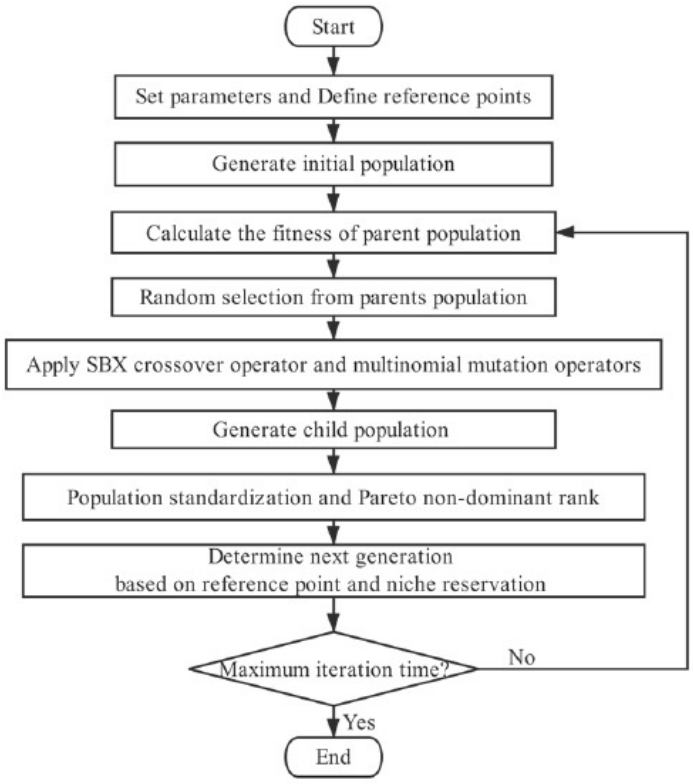

Figure 6.4: Flowchart of the Non-Dominated Sorted Genetic Algorithm III. Taken from Chen et al. [2019]

- The 'generator' is used to generate the initial population of the optimization process randomly, choosing the optimal variables within their own bounds;
- The 'bounder' ensures that candidate solutions respect the parameter bounds;
- The 'evaluator' function uses the sizing tool with the candidates of the population as input parameters and, then, evaluates the fitness vector.

On the other hand, the pymoo library works through a class called 'MyProblem'. This class has the '__init__' function which defines the optimization variable bounds, and the _evaluate function which uses the sizing process to evaluate the fitness vector of the problem.

The only objective function of the single-objective algorithms is the minimization of the exchanger mass. This could lead the optimization algorithm to find solutions with pressure drops too high. In order to avoid these solutions that are not convenient or repeatable, the two pressure drops are bounded. Moreover, another constraint is imposed over the exchanger height, to limit exchanger dimensions. Therefore, the sizing solutions that do not respect these constraints may not be considered in the optimization process and, in order to be sure to respect these bounds, a penalization method is applied.
The penalization process is shown in Fig.6.5 and will be described here. Each member of the population (the optimization variables) is used as input to make the heat exchanger sizing. Then, the sizing output parameters may be checked and the fitness of the problem is penalized if the output parameters do not respect the constraints. Firstly, the size constraint factor r_y is evaluated as

$$r_y = \frac{y}{Y_{max}}, \tag{6.4}$$

meanwhile, the dimensionless pressure drops are defined as

$$r_{\mathrm{c}} = \frac{\Delta P_{\mathrm{c}}}{\Delta P_{\mathrm{c_{max}}}} \qquad r_{\mathrm{h}} = \frac{\Delta P_{\mathrm{h}}}{\Delta P_{\mathrm{h_{max}}}}. \tag{6.5}$$

If the dimensionless pressure drops are bigger than 1, this means that the pressure drops are higher than the constraints and a penalizer is evaluated as follows:

$$penalizer_{\mathrm{c}} = r_{\mathrm{c}}^{p_{\mathrm{c}}} \qquad penalizer_{\mathrm{h}} = r_{\mathrm{h}}^{p_{\mathrm{h}}}. \tag{6.6}$$

The terms r_{c} and r_{h} have been already defined in Eq.6.5, instead, the terms p_{c} and p_{h} represent the strength of the penalization and, for this study, have been set $r_{\mathrm{c}} = 5$ and $r_{\mathrm{h}} = 5$.
Moreover, if the pressure drops evaluated in the sizing are too large and their dimensionless parameters are bigger than 2, another penalizer is calculated as:

$$f_{0_{\mathrm{c}}} = 8 + r_{\mathrm{c}} \qquad f_{0_{\mathrm{h}}} = 8 + r_{\mathrm{h}}. \tag{6.7}$$

On the other hand, the constraint imposed on the exchanger height y is more restrictive. Thus, if the r_{y} is bigger than 1, the solution is invalidated imposing the fitness as $f = 1e10$. Consequently, this solution is not considered in the optimization process, since the algorithms search for the minimum fitness. This condition is also applied if the sizing does not work successfully, or the sizing loop does not converge. This last case is expressed by the parameter $WARNING$ which is bigger than one if the sizing process does not reach the convergence.
Finally, the fitness can be evaluated as follows, to keep into account the effect of every penalizer:

$$f = (f_{0_{\mathrm{c}}} + f_{0_{\mathrm{h}}} + M_{\mathrm{hex}})\ penalizer_{\mathrm{h}}\ penalizer_{\mathrm{c}}. \tag{6.8}$$

Applying this method, even if the solution does not respect the pressure drops constraints, it can be still considered as a solution for the optimization process, since its fitness has been just penalized and not invalidated. This is because if a pressure drop does not exceed significantly its constraint, that solution can be still a valid solution.

The two objective functions of the multi-objective algorithm are the minimization of the exchanger mass and of the pressure drop on the hot side, consequently, just the height and the pressure drop on the cold side are constrained. If these two parameters have values over their own bounds, that solution is invalidated by assigning it the value Inf. Also if the sizing process does not work properly or if the converge loop ends without success, the current fitness value is set equal to infinity.
On the other hand, the many-objective algorithm evaluates the exchanger mass and the two pressure drops as fitness values, and, for this reason, the optimization bounds just the exchanger height.

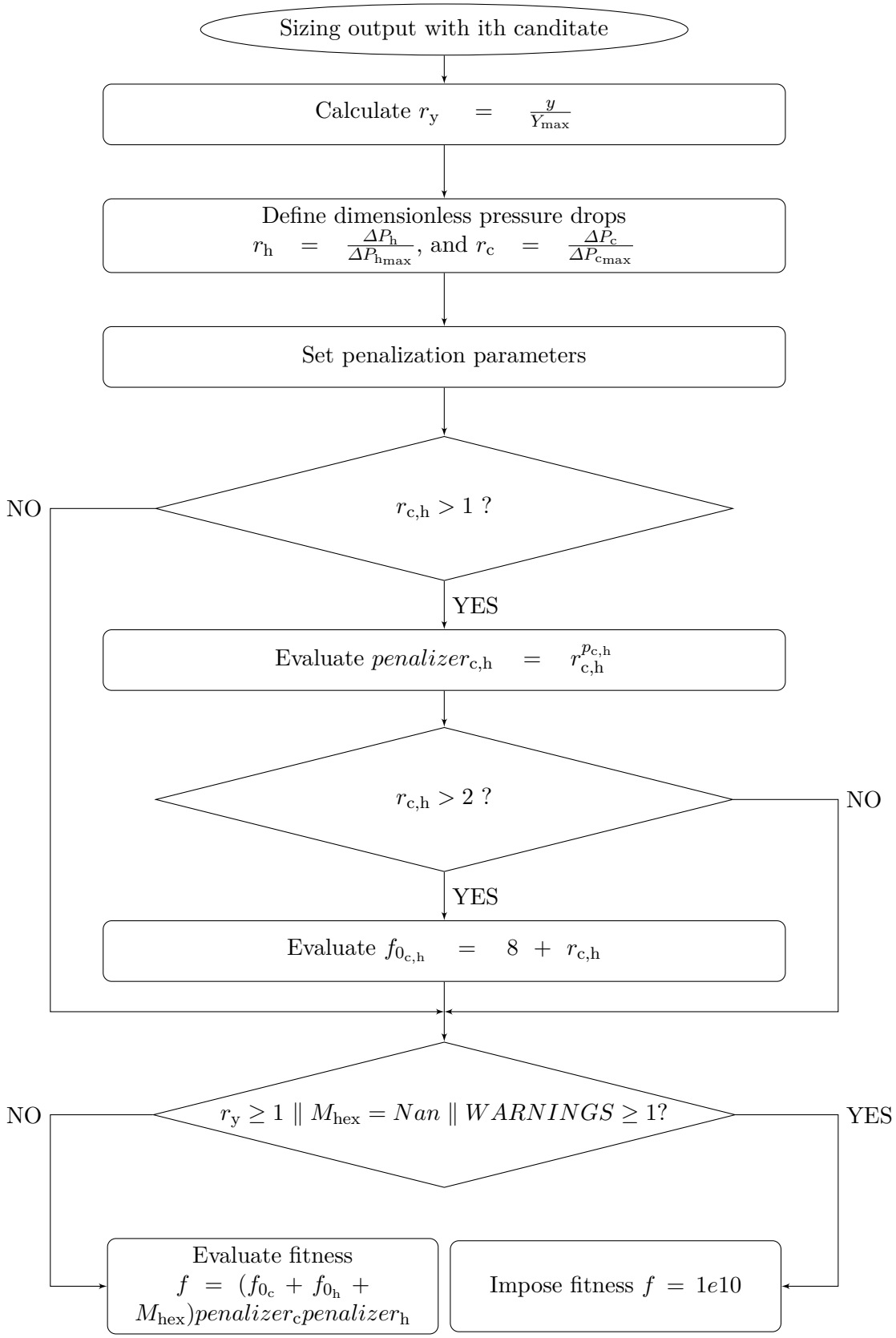

Figure 6.5: Flow chart for penalization method applied in single-objective optimizations.

6.2 Investigation of algorithm parameters

Before proceeding with the optimization analyses it is necessary to set all the algorithm parameters. Therefore, these parameters have been investigated in order to tune them to better values that help to improve the algorithm convergence. This step is fundamental to setting high algorithm searching performances: the optimization may be performed in less time than possible and have to reach the best convergence possible, finding the global optimum points.
The main parameters that have been investigated are the population size (pop_{size}) and the number of maximum generations (n_{gen}). Since the number of optimization variables (nv) changes for each fin case analyzed (depending on the geometric input parameters) and since the number of optimization variables is linked to these parameters, they have been normalized as follows:

$$\frac{pop_{\text{size}}}{nv},$$

$$\frac{n_{\text{gen}}}{nv}.$$

May be noted that, just for the NSGA-III, the parameter $\frac{pop_{\text{size}}}{nv}$ is replaced by the number of partitions p. Then, the population size can be evaluated assuming that it is equal to the number of reference points and, thus, using Eq.6.3.
Besides the population size and the number of maximum generations, also other parameters have been investigated, such as the inertia, the social rate, and the cognitive rate for the PSO; the crossover rate (CR) and the mutation rate (MR) for the DEA and the NSGA-II; the crossover rate for the NSGA-III.
The tuning process adopted for this thesis is here described:

1. the optimization is performed varying the values of pop_{size} and n_{gen} and keeping the default values for the other parameters;
2. the execution time and the optimal solutions are saved;
3. steps 1 and 2 are repeated 5 times in order to avoid the random effect introduced by the algorithms;
4. the output of step 2 are compared to find the parameters that give the minimum working time and the best optimal solution;
5. the values selected are set for further analyses where pop_{size} and n_{gen} are kept constant, meanwhile the other investigated parameters change;
6. step 2 is repeated;
7. steps 5 and 2 are repeated 5 times;
8. the output of the 5 optimizations performed are compared to find the parameters that give the minimum working time and the best optimal solution.

The process outlined above has been followed for each optimization algorithm considered and Tab.6.2 shows a resume of the optimization parameters analyzed, of their range considered, and of the selected values.
The parameters selected have been chosen keeping into account that high values of $\frac{pop_{\text{size}}}{nv}$ and $\frac{n_{\text{gen}}}{nv}$ take to long working time but, also, to a better convergence to the optimal solutions. Consequently, a trade-off between these two algorithm performances has been made, noting that with different values of pop_{size} and n_{gen} the optimal solutions do not change significantly.

Algorithm	Investigated optimization parameters	Selected values
DEA	$\frac{pop_{\text{size}}}{nv} = [10, 15, 20, 25, 30]$	$\frac{pop_{\text{size}}}{nv} = 15$
	$\frac{n_{\text{gen}}}{nv} = [3, 4, 5, 6]$	$\frac{n_{\text{gen}}}{nv} = 4$
	CR = [0.1, 0.25, 0.5, 0.75, 1]	CR = 0.75
	MR = [0.1, 0.25, 0.5, 0.75, 1]	MR = 0.1
PSO	$\frac{pop_{\text{size}}}{nv} = [10, 15, 20, 25, 30]$	$\frac{pop_{\text{size}}}{nv} = 15$
	$\frac{n_{\text{gen}}}{nv} = [3, 4, 5, 6]$	$\frac{n_{\text{gen}}}{nv} = 4$
	inertia = [0.4, 0.5, 0.65, 0.8]	inertia = 0.45
	social rate = [1.4, 1.6, 1.8, 2.1, 2.3]	social rate = 1.4
	cognitive rate = [1.4, 1.6, 1.8, 2.1, 2.3]	cognitive rate = 1.4
NSGA-II	$\frac{pop_{\text{size}}}{nv} = [10, 15, 20, 25, 30]$	$\frac{pop_{\text{size}}}{nv} = 10$
	$\frac{n_{\text{gen}}}{nv} = [3, 4, 5, 6]$	$\frac{n_{\text{gen}}}{nv} = 4$
	CR = [0.1, 0.25, 0. 5, 0.75, 1]	CR = 0.75
	MR = [0.1, 0.25, 0.5, 0.75, 1]	MR = 0.25
NSGA-III	$p = [12, 14, 16, 18, 20]$	$p = 12$
	$\frac{n_{\text{gen}}}{nv} = [3, 4, 5, 6]$	$\frac{n_{\text{gen}}}{nv} = 4$
	CR = [0.1, 0.25, 0. 5, 0.75, 1]	CR = 1

Table 6.2: Resume of tuning of optimization parameters.

6.3 Optimized design maps

For the optimizations proposed here, the behaviours of the different fin types have been analyzed through the comparison of the following performance metrics: the mass-specific power $MSP = \frac{\dot{Q}}{M_{\text{hex}}}$, the two pressure drops ΔP_{h} and ΔP_{c}, the two Bejan number Bej_{c} and Bej_{h}. The Bejan number is defined as

$$Bej = \Delta P \frac{L^2}{\rho \nu^2} \tag{6.9}$$

and represents a dimensionless pressure drop, where L is the flow length.

Here, for the design optimizations has been selected a test case from Shah and Sekulić [2003] with an air-air single pass heat exchanger with a cross-flow arrangement. The heat exchanger has been made balanced ($C^* = 1$) and the parameters used are listed in Fig.6.3. The heat exchanger uses the same geometry on both fluid sides and its design optimization has been performed with three different fin types, in order to compare their own performances: offset-strip fins, louvered fins, and triangular wavy fins. The validity bounds of the geometric parameters are the same as listed in Tab.6.1, meanwhile, the Reynolds numbers vary within $Re = 200$ and $Re = 2000$, except for

the analyses with triangular wavy fins, for which the lower bound of the correlation proposed in Ch.2.2.2 is $Re = 800$.

Characteristics of test case for design optimizations	
$\dot{Q}$ [kW]	1083.8
$P_{\mathrm{i_c}}$ [bar]	2
$P_{\mathrm{i_h}}$ [bar]	2
$T_{\mathrm{i_c}}$ [K]	200
$T_{\mathrm{i_h}}$ [K]	900
$\dot{m}_{\mathrm{c}}$ [kg/s]	2
$\dot{m}_{\mathrm{h}}$ [kg/s]	2.0913
t_{f} [mm]	0.102
t_{w} [mm]	0.5

Table 6.3: Thermodynamic and structure parameters of the test case for design optimizations. The values of $P_{\mathrm{i_h}}$ and $\dot{m}_{\mathrm{h}}$ in the table are different from the reference [21] since they have been modified to have $C^* = 1$.

Since the DEA and the PSO algorithm have just one objective function, their output is made of just one solution which represents the optimal point and, thus, it is not possible to have different comparable trends. Consequently, the optimization problem has been performed with some varying input parameters which take to a set of solutions. Particularly, two different analyses have been performed. The first one has been made for a given heat duty $\dot{Q}$ value varying the value of the constraint on ΔP_{h}. Meanwhile, the second optimization considers different values of heat duty $\dot{Q}$, keeping constant the value of the constraint on ΔP_{h}.
On the other hand, the output of NSGA-II and NSGA-III is a set of solutions and the design maps show the trend of these solutions for several performance metrics.

6.3.1 Single objective optimizations varying the constraint on ΔP_{h} with DEA and PSO

The first optimization with single objective algorithms has been made by varying just the constraint on the pressure drop on the hot side $\Delta P_{\mathrm{h_{max}}}$. With this analysis it is possible to plot a set of solutions and, in this study, has been chosen to perform the optimization for ten points. Consequently, ten different increasing values of the constraint on ΔP_{h} have been selected: ten evenly spaced values from $\Delta P_{\mathrm{h_{min}}} = 8kPa$ to $\Delta P_{\mathrm{h_{max}}} = 15kPa$.

Firstly, the solutions obtained with the DEA are shown. Fig.6.6 show the optimized design maps that relate the MSP with the pressure drop on the cold and the hot side respectively. Looking at these plots it is important to note that every solution respects the constraints imposed on both pressure drops, here represented by vertical dotted lines. Furthermore, it is interesting to highlight that the performances of the different fins vary within some spots in the graph. Varying the constraint of ΔP_{h}, the TWF solutions maintain more or less the same MSP and assume different values of both pressure drops. On the other hand, the OSF and the LF points do not maintain the same MSP, even if it does not reach big fluctuations. Generally, the pressure drop on the hot side evolves in a big range, since its values follow the variations of its own constraint. Meanwhile, the pressure drop on the cold side maintains similar values for each solution, near the imposed constraint. Then, relating the MSP with the Bejan numbers (see Figs.6.7), it is possible to see that each fin type works in a specific zone of the plot and this trend is mainly influenced by the flow length which has a quadratic effect on the Bejan number $Bej = \Delta P \frac{L^2}{\rho \nu^2}$. In this condition, the triangular wavy fins give the worst performances: maintain low values of MSP and work at high Bejan numbers. This

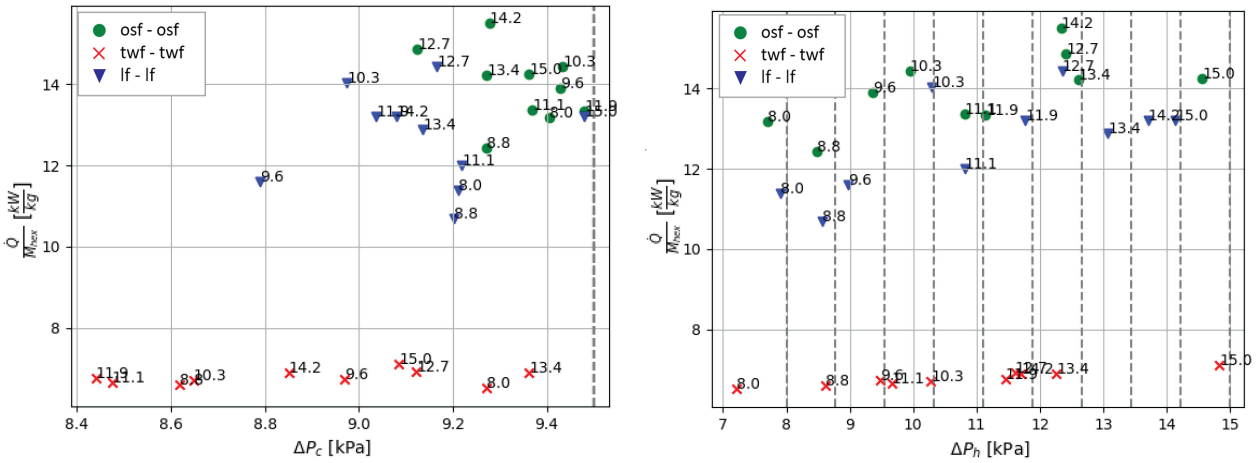

(a) (b)

Figure 6.6: Optimized design maps for single objective optimization with DEA varying the constraint on ΔP_{h}, plotting the MSP as a function of a) pressure drop on the cold side ΔP_{c}, b) pressure drop on the hot side ΔP_{h}.

means that using this fin type the exchanger reaches big mass and high frontal areas, compared to the other two surfaces. Meanwhile, the offset-strip fins and the louvered fins have very similar performances, even if the OSF overcome the LF, both in terms of mass and sizes. Now, the same

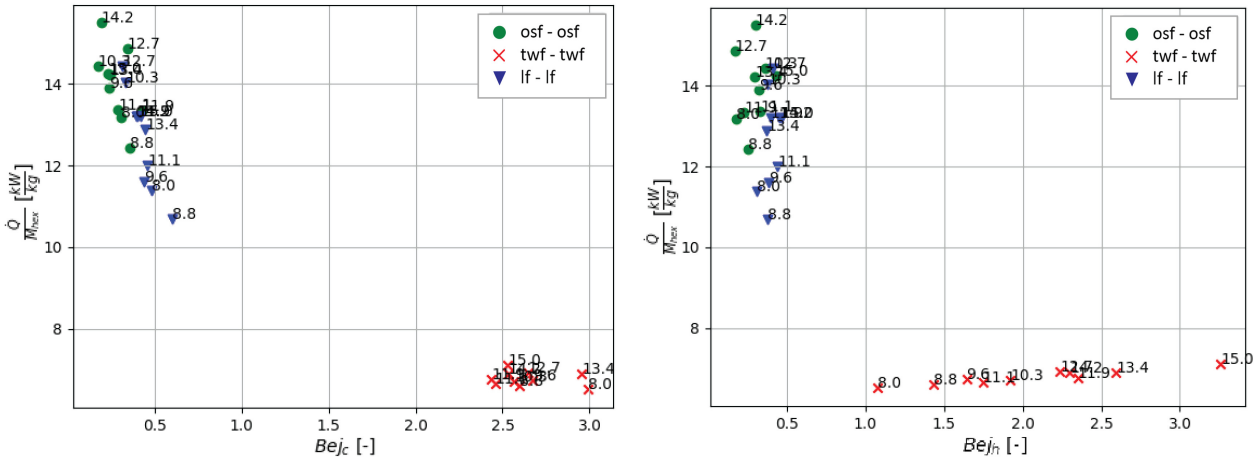

(a) (b)

Figure 6.7: Optimized design maps for single objective optimization with DEA varying the constraint on ΔP_{h}, plotting the MSP as a function of a) Bejan number on the cold side Bej_{c}, b) Bejan number on the hot side Bej_{h}.

optimized design maps obtained with the PSO algorithm are presented. Analyzing the maps in Fig.6.8, it is possible to see well-defined clusters of points, such as for the maps of Figs.6.6 and 6.7. Even if the trends of the fins are very close to those obtained through the optimization with DEA, it is possible to note that the design optimization with the PSO achieves better results. The offset-strip fins and the louvered fins reach higher MSP values than those of Figs.6.6 and 6.7, the MSP has smaller fluctuations and, furthermore, the pressure drops are closer to their constraints. Then, the main difference to underline is that in these optimized design maps, the louvered fins overcome the offset-strip fins, differently to the optimized maps with DEA. These discrepancies can be linked to the optimization process of these two algorithms. The process of the DEA is based on a target vector from the initial population and this could lead the algorithm to find a local optimum, meanwhile the PSO reach the global optimum. According to these considerations, the results with

the PSO have to be considered more accurate.

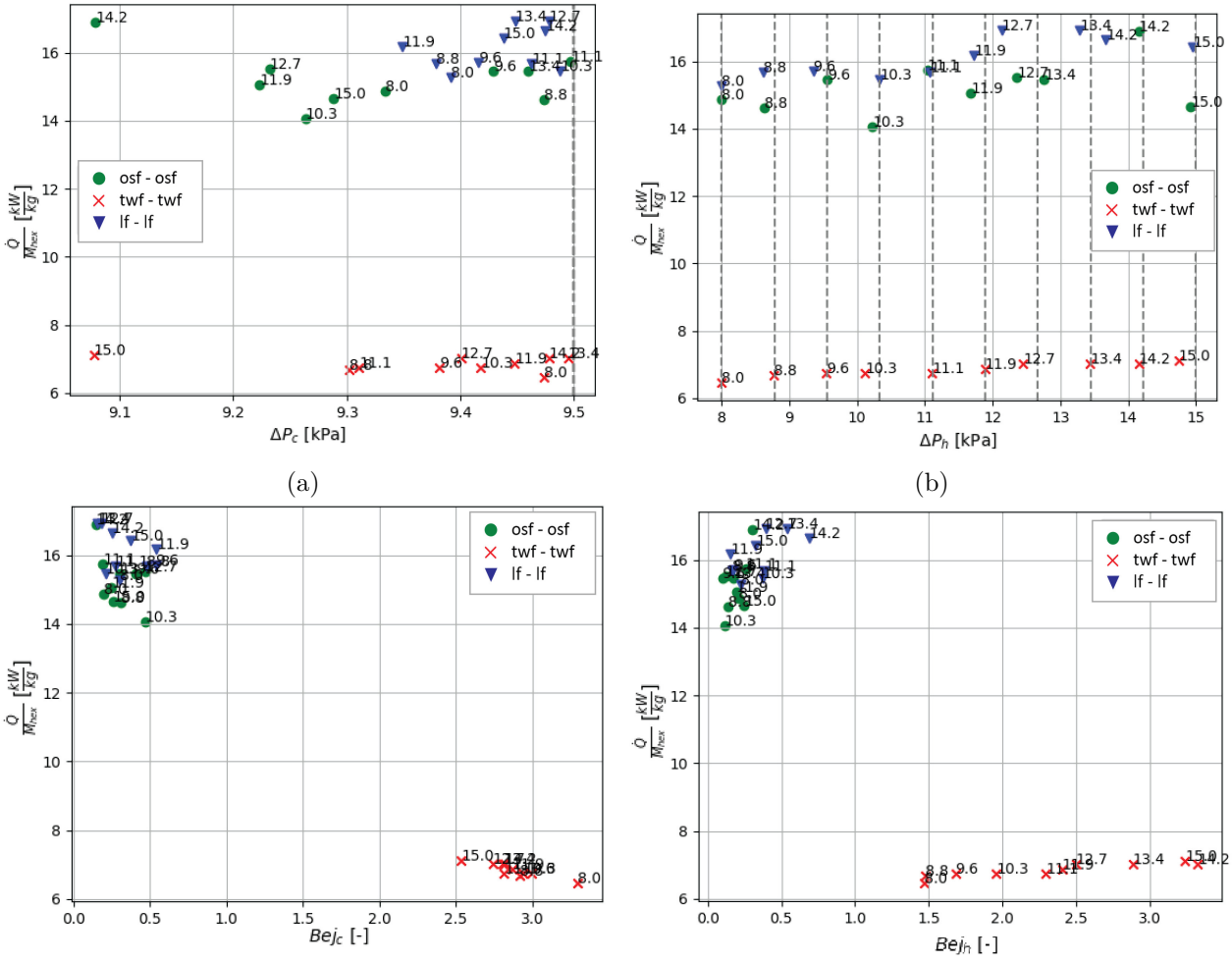

Figure 6.8: Optimized design maps for single objective optimization with PSO varying the constraint on ΔP_{h}, plotting the MSP as a function of a) pressure drop on the cold side ΔP_{c}, b) pressure drop on the hot side ΔP_{h} c) Bejan number on the cold side Bej_{c}, d) Bejan number on the hot side Bej_{h}.

6.3.2 Single objective optimizations varying heat duty $\dot{Q}$ with DEA and PSO

This section shows the optimized design maps obtained with the single objective optimizations varying the heat duty $\dot{Q}$ and keeping constant the other parameters. Such as for the previous single objective optimization, this analysis has been performed for ten points. In this case, the ten values of heat duty have been calculated starting from an array of different values of effectiveness: ten evenly spaced values from $\epsilon_{\mathrm{min}} = 0.5$ to $\epsilon_{\mathrm{max}} = 0.85$. Then, the heat duty's values can be estimated as

$$\dot{Q}_{\mathrm{i}} = \epsilon_{\mathrm{i}}\ \dot{m}_{\mathrm{c}}\ c_{\mathrm{p_{in}}}\ \Delta T_{\mathrm{max}}. \tag{6.10}$$

Here, instead of mean c_{p} has been used the inlet c_{p} since the value of $c_{\mathrm{p_m}}$ is unknown. For this analysis, the optimized design maps obtained with the DEA in Fig.6.9 show the relationship of the MSP with the two pressure drops for each solution. Looking at these plots, every solution respects the bounds on the pressure drops but it is impossible to define a trend for the several fin types. Consequently, other design maps have been plotted, relating the MSP with the two Bejan numbers Bej. The optimized design maps with the Bejan numbers, shown in Fig.6.10, outlines a clear trend of the fins' behaviour. Here, it is possible to see that by increasing the effectiveness value, the MSP

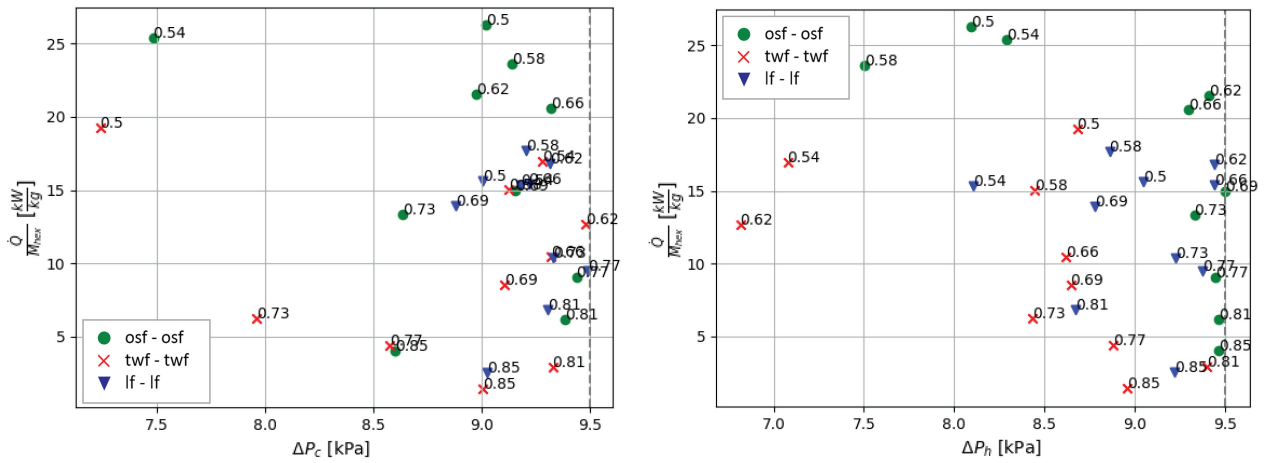

(a) (b)

Figure 6.9: Optimized design maps for single objective optimization with DEA varying the heat duty $\dot{Q}$, plotting the MSP as a function of a) pressure drop on the cold side ΔP_c, b) pressure drop on the hot side ΔP_h.

decreases following a $1/x^n$ trend and, consequently, the exchanger mass increases. Meanwhile, for high ϵ the solutions reach higher Bejan numbers. This trend can be explained by looking at the definition of the effectiveness $\epsilon = \frac{\dot{Q}}{\dot{Q}_{\max}}$. Therefore, increasing the effectiveness, the heat duty goes up too but, on the other hand, the ϵ is directly proportioned to the flow lengths. This means that, if the effectiveness rises, the flow lengths and, consequently, the exchanger mass increase too. It is thus clear that the heat exchanger mass grows more than the heat duty does, and as such the mass-specific power decreases. Since the flow length has a quadratic effect on the Bejan number $Bej = \Delta P \frac{L^2}{\rho \nu^2}$, this parameter grows with the effectiveness. The optimized design maps obtained

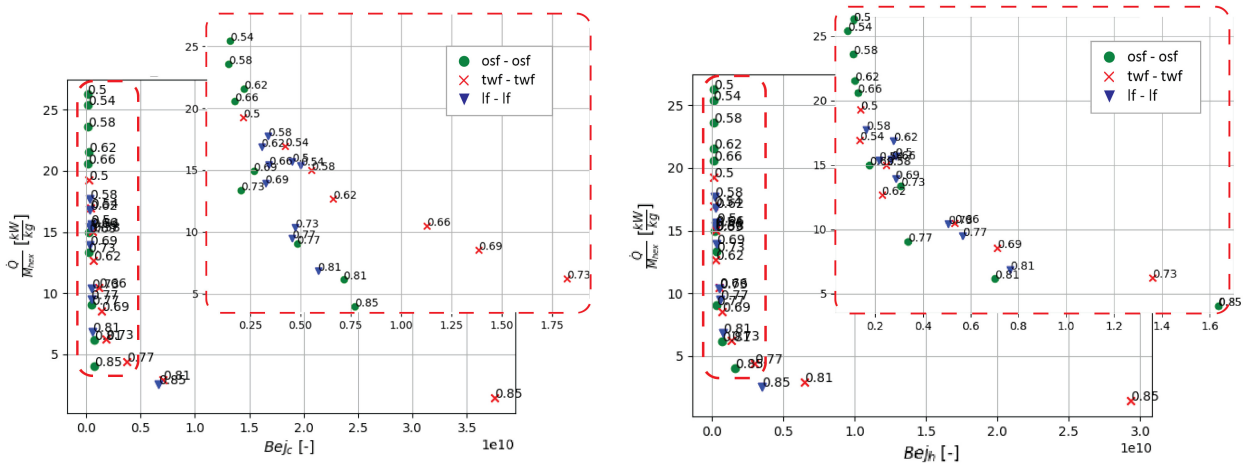

(a) (b)

Figure 6.10: Optimized design maps for single objective optimization with DEA varying the heat duty $\dot{Q}$, plotting the MSP as a function of a) Bejan number on the cold side Bej_c, b) Bejan number on the hot side Bej_h. Both images show a close-up at low Bejan numbers.

with the PSO show more or less the same results, as shown in Fig.6.11. As for the optimization in section 6.3.1, the optimization with the PSO algorithm yields a higher level of convergence in the mass-specific power vs Bejan plot. As a result, the PSO-based optimization reaches lower mass values, with pressure losses closer to the constraints. Then, looking at Figs.6.11c and 6.11d, it is interesting to compare the trend of the different fin types. The offset-strip fins and the louvered fins

have performances very comparable, even if the OSF reach better results than the LF. On the other hand, the triangular wavy fins have the worst performances of the three fin geometries considered in this analysis.

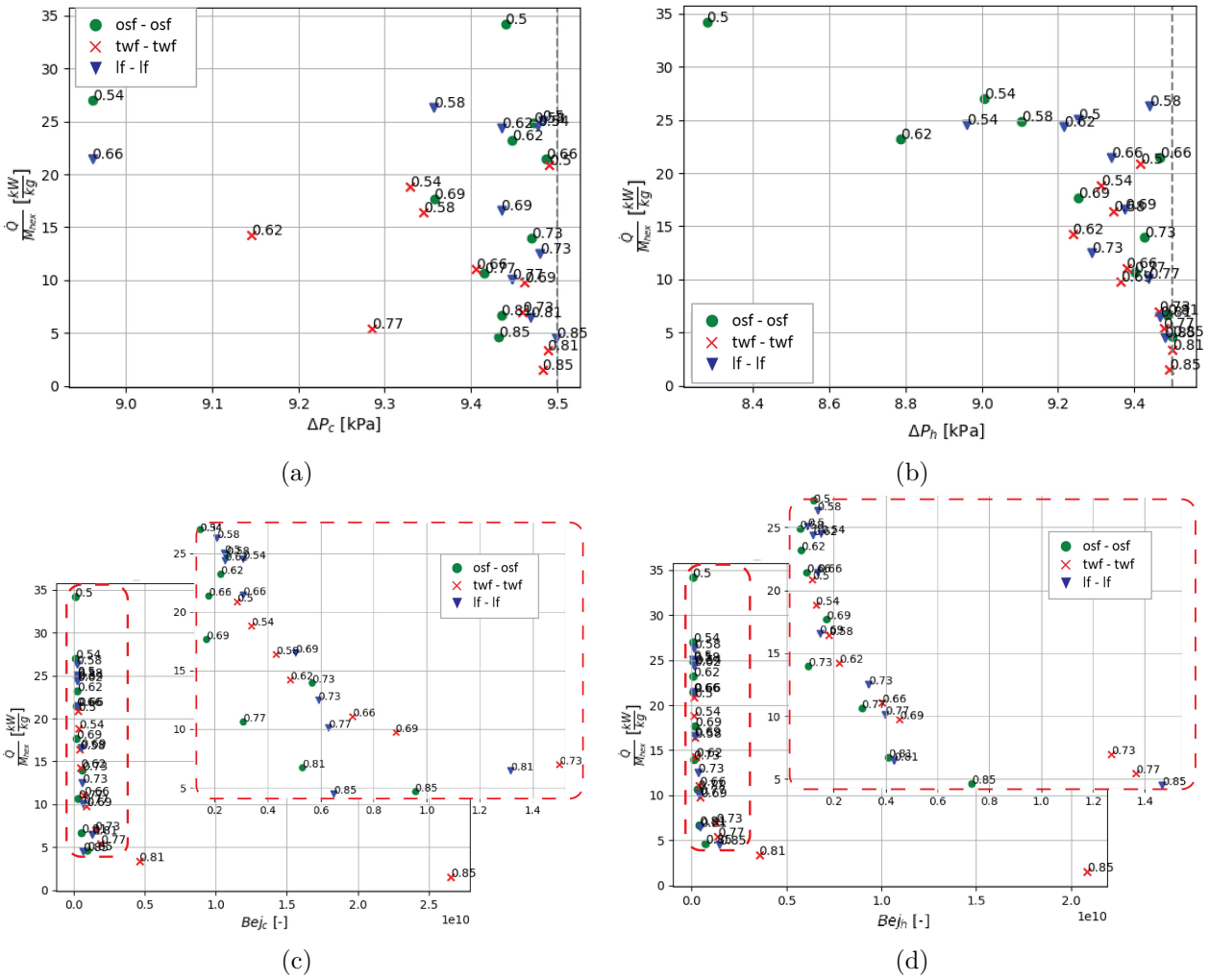

Figure 6.11: Optimized design maps for single objective optimization with DEA varying the heat duty $\dot{Q}$, plotting the MSP as a function of a) pressure drop on the cold side ΔP_c, b) pressure drop on the hot side ΔP_h, c) Bejan number on the cold side Bej_c, d) Bejan number on the hot side Bej_h. Images c) and d) show a close-up at low Bejan numbers.

The differences between PSO and DEA, as expressed in the preceding analysis, can potentially be attributed to the behavior of the DEA. This algorithm, such as previously described in Ch.6.1, works by defining a target vector that limits the search space and this may take the algorithm to find local minimums, differently than the PSO. However, according to these considerations, it is possible to say that the PSO is the best choice for this analysis, even if it needs more working time than the DEA to reach the convergence.

6.3.3 Multi-objective optimizations with NSGA-II

The Pareto Front of this optimization is shown in Fig,6.12 and it represents the relationship between the two objective functions: the exchanger mass, included in the mass-specific power MSP, and the pressure drop on the hot side. Differently from the single objective optimizations, this map with the pressure losses on the hot side ΔP_h gives a clear and hyperbolic trend for each fin since the pressure drop is one of the objective functions. This Pareto Front depicts the expected behaviour of the fins' performances: increasing the exchanger mass (low MSP values), the pressure losses go

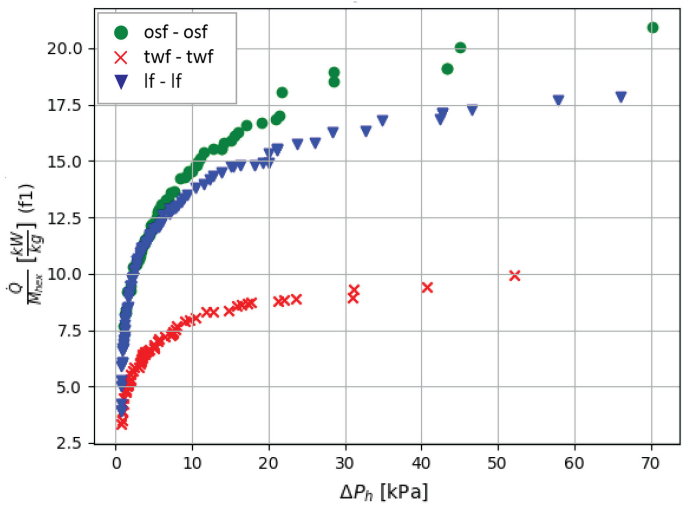

Figure 6.12: Pareto front obtained with the NSGA-II multi-objective optimization algorithm.

down. Furthermore, this graph enables a good surface selection: the trend of triangular wavy fins confirms that they have the worst performance for this test case, meanwhile the performance metrics reflect a behaviour of the offset-strip fins very close to that one of the louvered fins. Especially, the TWF take the exchanger to have a high mass, since they reach low values of mass-specific power, on the other hand, the other two fin types take more advantages with low mass and the ΔP_{h}, very comparable with those obtained with the TWF. Lastly, even if the OSF and the LF are very similar, the offset-strip fins reach better results.
Then, looking at the plot which shows the relationship between MSP and the pressure drop on the

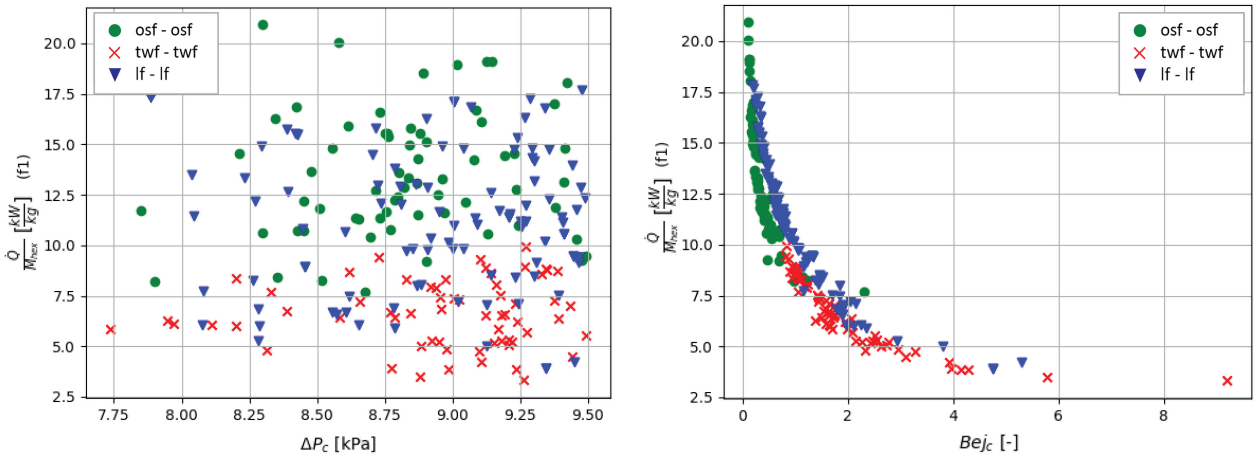

(a) (b)

Figure 6.13: Optimized design maps for multi-objective optimization with NSGA-II, plotting the MSP as a function of a) pressure drop on the cold side ΔP_{c}, b) Bejan number on the cold side Bej_{c}.

cold side (see Fig.6.13), it is possible to see that there is no trend and all the solutions are scattered in the plot. The pressure drop on the cold side ΔP_{c} is not optimized but is constrained, so the points do not make a clear trend but respect the imposed bound and stay in a small range close to the constraint (about 18% maximum). In order to link the heat exchanger mass with the pressure losses on the cold side, a map with the Bejan number has been plotted. The Fig.6.13b shows a fascinating behaviour of the fins. In this map, the two performance metrics (MSP and Bej_{c}) are strongly related following a $1/x^{\mathrm{n}}$ trend, and making a sort of Pareto Front, even if the pressure drop on this fluid side is not an objective function. This behaviour of the Bejan number is mainly given

by the effect of the flow length which has a quadratic influence and, here, the three fin types have very close trends. Consequently, the Figs. 6.12 and 6.13b can help in the heat exchanger design since enable linking the behaviour on both fluid sides, bounding the losses on one side.
Finally, to sum up the behaviour of each fin, it is possible to use the colormaps in Fig.6.14. Each of these maps relates the three performance parameters (MSP, Bej_{c}, Bej_{h}) for each fin type considered, underlining their hyperbolic trend. Especially, the mass-specific power has a different behavoiur related to the Bej on the two fluid sides. The MSP reaches its maximum when the Bej on the optimized side is high but the Bej on the constrained side decreases. This means that if the HX design is focused on minimizing its mass, the two flow lengths must be short, meanwhile, the optimized side must have high pressure losses. On the other hand, it is not feasible to define exactly the pressure losses on the other side but it is possible to limit them with a constraint.

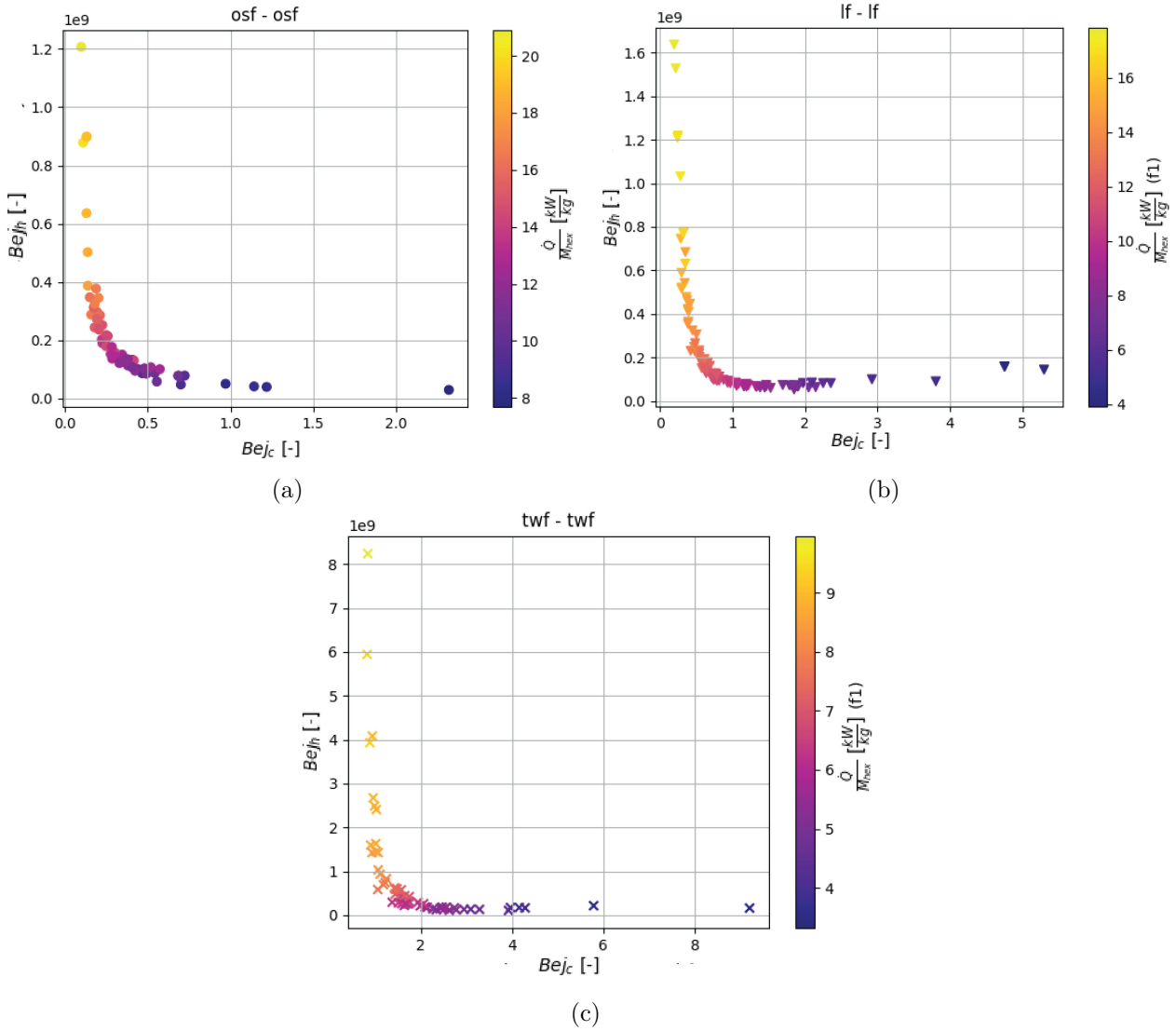

Figure 6.14: Optimized design colormaps for multi-objective optimization with NSGA-II. These maps show the relationship between MSP, Bej_{c}, and Bej_{h} for a heat exchanger with a) offset-strip fins, b) louvered fins, c) triangular wavy fins.

6.3.4 Many objective optimizations with NSGA-III

The last design optimization has been performed with the NSGA-III for three objective functions: the exchanger mass and the two pressure drops. The maps obtained with this analysis are shown in Fig.6.15. The points in these graphs represent the relationship between the mass-specific power,

the pressure drop on the cold side, and the pressure drop on the hot side for each surface geometry considered in this test case. How it was expected, high values of exchanger mass take to low pressure losses on both fluid sides.
It is interesting to note that from the mass point of view, it is better to select the offset-strip fins since they reach the highest mass-specific power, meanwhile, the triangular wavy fins have the lowest mass-specific power. On the other hand, using the triangular wavy fins, the heat exchanger has small pressure losses on the cold side but to have small pressure losses on the hot side, it is a bit better to choose the louvered fins. Hence, the surface with the minimum mass may not give the lowest pressure losses. Consequently, the selection of the optimal fin surface changes depending on which are the main constraints and objectives of the design. Specifically for this case, if the main goal is to obtain a light exchanger, the designer will choose the offset-strip fins. On the contrary, he or she will choose the triangular wavy fins to have smaller pressure losses along the channels.

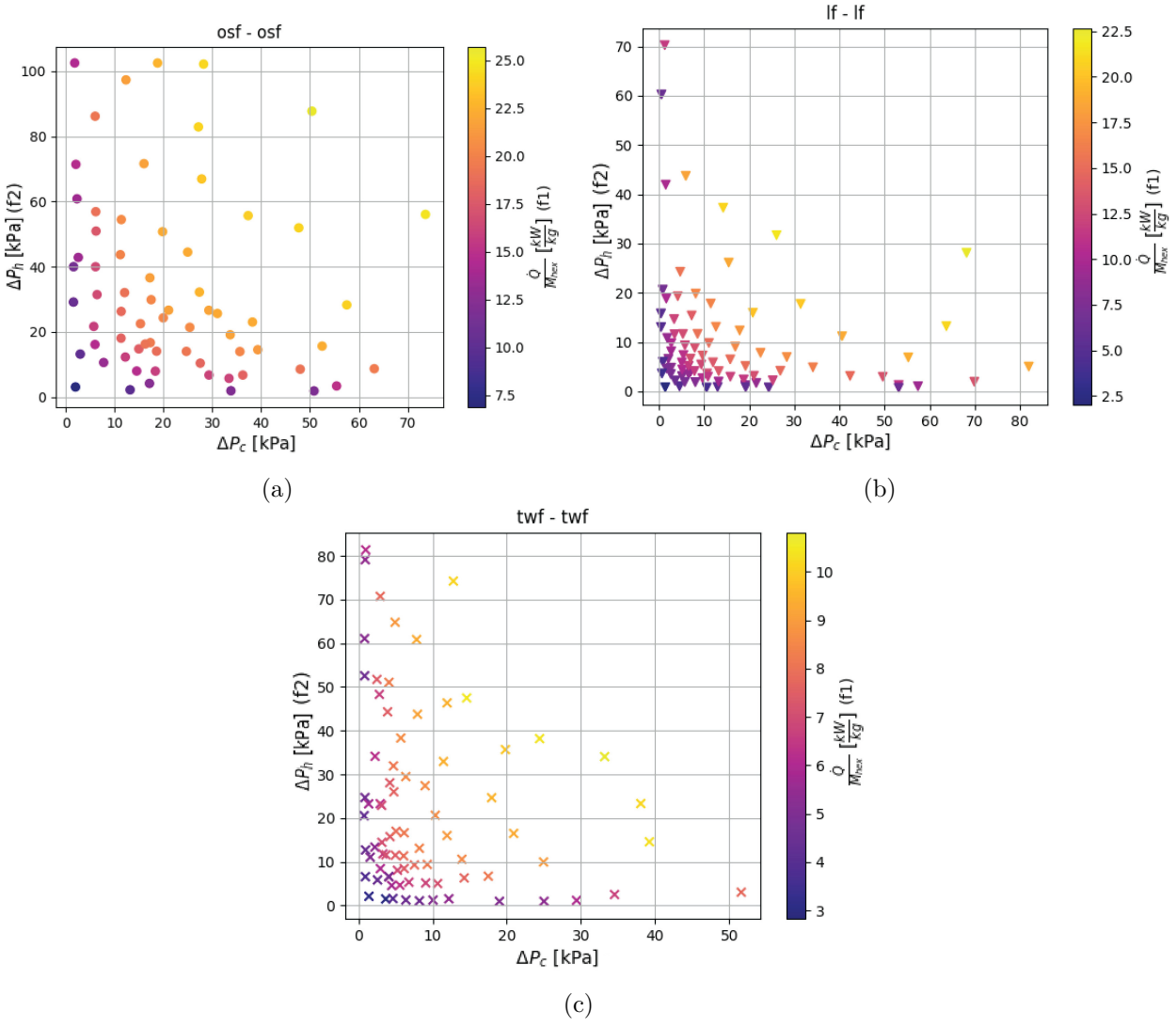

(a) (b)

(c)

Figure 6.15: Optimized design colormaps for multi-objective optimization with NSGA-III. These maps show the relationship between MSP, ΔP_c, and ΔP_h for a heat exchanger with a) offset-strip fins, b) louvered fins, c) triangular wavy fins.

Chapter 7

Conclusions

The selection of a specific fin type for each fluid side of a compact plate-fin heat exchanger depends on the thermodynamic specifications and geometrical constraints, and is a fundamental step in the preliminary design of compact heat exchangers for aerospace applications. The choice of the optimal enhanced surfaces has, typically, been pursued by some experts in the field driven by their own experience. The main scope of this thesis is to provide a good surface selection method that overcomes the limitations of the previous, and that can give useful information on the maximum mass-specific performance of these components. This method helps the designer of an airborne thermal system at a preliminary design stage, choose the best compact heat exchanger topology, and assess what is the weight and the pressure drop performance of such components. The method itself is a comparison of optimized HX geometries in terms of mass-specific power and Bejan numbers, at varying constraints on the pressure drops.
The present work was motivated by the following research questions:

- How can we develop a heat exchanger sizing approach to evaluate the pressure losses and the exchanger mass, converging on the mean Reynolds numbers?
- Which performance metrics allow a good comparison between the behaviour of different fin geometries?
- How can we ensure a good surface selection for each fluid side?

To formulate a first answer these questions, the following objectives have been achieved:

1. modelling of different fin geometries and their thermal performance using j and f correlations;
2. verification of the geometric equations obtained and of the correlations taken from scientific literature;
3. implementation of a compact plate-fin heat exchanger preliminary design tool in Python language;
4. development of a compact plate-fin heat exchanger rating tool in Python language;
5. verification of the sizing and rating tools by comparing the generated outputs with data of similar test cases from scientific literature and from the commercial software *EchTherm*;
6. application of different optimization algorithms (single, multi, and many objectives) to the design problem of a heat exchanger, and comparison of the results;
7. selection of appropriate performance metrics to compare the mass-specific performance of different plate-fin topologies;
8. application of the performance comparison method through the generation of different optimized design maps for an air-air first test case, obtained through multiple optimization algorithms;

9. analysis of the optimized design performance trends of each tested fin type.

In particular, in Chapter 2, six different fin types have been modeled defining their own geometric equations and showing their own j and f correlations. The fin geometries presented here are the rectangular and triangular plain fins, the rectangular and triangular wavy fins, the offset-strip fins, and the louvered fins. Once all the geometric characteristics have been defined, the fin modeling has been verified by analyzing the deviations of d_{h} and β evaluated in this thesis by those given by Kays and London [2018]. It is possible to note that, for all the geometries analyzed, the equations defined here reach reliable results.
Therefore, the j and f correlations have been verified by comparing the values of j and f factors of the experimental correlations presented in Chapter 2, with the experimental values of Kays and London [2018]. The verification maps show the trend of Colburn and friction factors against the Reynolds number. These comparisons show that the plain fins correlations reach results that differ significantly from the experimental data, as a result these correlations are not used in this work. On the other hand, the verification of other geometries' correlations shows good results. The correlations proposed for wavy fins (both rectangular and triangular) can be considered good for the analyses of this thesis since they give results very close to experimental ones. The correlations used for the offset-strip fins have been proven to be quite accurate when compared to experimental data. The implemented Colburn and friction factor correlations for the louvered fins seem to predict values that tend to differ from one another. In particular, the correlations proposed by Chang and Wang [1997] are the ones with the lowest deviation from the experimental data. It is important to note that all the correlations proposed in Ch.2.4 have been developed for louvered fins with flat tubes, while the data used for the comparison refers only to the louvered fin channels. Consequently, some of the parameters required in the correlations are not defined in the reference and had to be assumed. This discrepancy justifies the differences in the prediction of thermal performance between correlations and experimental data. Nevertheless, the results predicted by the correlation of Chang and Wang [1997] are considered suitable for this work.

Chapters 4 and 5 describe the developed rating and sizing tools. The verification of the models has been performed by comparing the parameters evaluated in the current work with those from several test cases taken from the scientific literature. Generally, can be noted that, for the sizing, the best results are reached by imposing the height and setting the convergence loop to the outlet pressures. These comparisons highlight that, in some cases, the parameters obtained with the tools developed for the current study do not differ too much from the parameters of the test cases. On the other hand, some verifications show huge deviations from the test case's data, and this discrepancy is explained by the assumptions adopted by the different approaches of the references. Consequently, these two tools can be used for heat exchanger design.

Finally, the optimization algorithms presented in Chapter 6 have been used to perform the design of the heat exchanger of a balanced air-air test case, considering three different fin types (the same for each fluid side). The fin geometries used are the triangular wavy fins, the offset-strip fins, and the louvered fins.
The single objective optimization algorithms (DEA and PSO) have been applied for two different analyses: a) use different values of the constraint of the ΔP_{h} with a constant heat duty; b) vary the heat duty, keeping the constraint of the pressure drop on the hot side constant. In the first case, the maps of MSP versus the Bej show that all the solutions are grouped in clusters. These maps highlight that each fin geometry operates optimally in a well-defined Bej range. It is worth noting that the results reached with the PSO differ from those given by the DEA. The PSO takes to optimal MSP more or less constant, meanwhile, the optimal values reached by the DEA cover a bigger MSP range. However, the main difference is that using the PSO, the LF reach the best performance, meanwhile, with the DEA, the OSF have the best behaviour. This discrepancy can be linked to the approach of the DEA which starts from a target vector and this can take the algorithm to find a local minimum. Thus, even if the PSO is slower than the DEA, it remains the best choice

since it reaches better results: lower exchanger mass and optimal solutions closer to the constraints. On the other hand, varying the effectiveness and keeping constant the constraints on both pressure drops, the maps of MSP versus the pressure drops do not clearly represent the fins' behaviour. Meanwhile, the optimal MSP show a clear trend if they are plotted as a function of the Bej numbers. In this case, it is possible to see that the exchanger mass decreases with decreasing effectiveness following the $1/x^n$ trend. High values of ϵ take to big flow lengths which influence the M_{hex} and the Bej number, increasing them. The heat duty also grows up with the ϵ, but the effect of the increasing effectiveness is stronger on the exchanger mass. Consequently, the MSP decrease with rising ϵ. This analysis shows that the OSF reach the best performance with both algorithms, even if the PSO still takes to better results. Lastly, the TWF cover the worst performance in both analyses performed.
The multi-objective optimization, performed through the NSGA-II, takes to a clear trend of the Pareto front, which shows the relationship between the MSP and the ΔP_{h}. These two performance parameters represent the two objective functions of the problem and are directly related following a hyperbolic trend: the MSP increases with increasing ΔP_{h}. On the other hand, the map of mass-specific power versus the pressure drop on the cold side does not exhibit a well-defined trend, and all the optimal solutions are scattered. On the contrary, the behaviour of the cold side can be studied on the MSP-Bej_{c} map. Here, it is interesting to note a clear relationship, that follows a $1/x^n$ trend, between the mass-specific power and the Bej_{c}. Differently from the other fluid side, the ΔP_{c} is not an objective function but is constrained, and the trend of its Bejan number is mainly given by the influence of its flow length. Then, studying the relationship between the three performance metrics, it is interesting to note that the two Bejan numbers have opposite behaviour related to the MSP. When the exchanger mass goes down, the Bej number on the cold side increases, meanwhile, the Bej number on the hot side rises, following the trend of its pressure drop. Generally, in order to have a lighter exchanger the designer has to accept significant losses on the optimized fluid side. Meanwhile, even if it is not feasible to establish the losses on the other side, it is possible to limit them. Concerning the test case analyzed in this work, the offset-strip fins reach the best performances, even if they are very close to the louvered fins. Meanwhile, the triangular wavy fins remain the worst choice for this design problem.
Lastly, the three-objective optimization returns the design maps that relate the two pressure drops to the mass-specific power. These maps exhibit a 3D Pareto front of the problem, which highlights that, as expected, the two pressure drops increase for high MSP. Analyzing these design maps, it is worth noting that there is not a single fin type that always overcomes the others. The offset-strip fins give the lower weight, but on the other hand, have higher pressure losses than the triangular wavy fins. Thus. this last analysis shows how important it is to make a trade-off between the different geometries.

7.1 Recommendations and future work

This section presents a summary of different recommendations and suggestions on how to apply and improve upon the present work.
The design approach presented in this work is based on the assumptions outlined in Ch.3 and needs to be extended in order to be applicable to conditions that differ from the ones highlighted in the present work. The optimized design maps in Ch.6.3, show the trends of different performance metrics and the relationships between them just for the test case analyzed in this work. The heat exchanger studied works with air on both fluid sides and is balanced. Furthermore, the design maps present the behaviour of just three fin combinations: osf-osf, lf-lf, twf-twf. Consequently, the final considerations made in this chapter about the fins' behaviour are specific to this case and are not valid to design other exchangers. The results reached by this selection method are different for each test case and future works could focus on applying this approach to heat exchangers with different operating conditions. More specifically, it could be interesting to study design maps for cases with:

- different fluids on the two sides;
- other fin combinations, such osf-lf;
- fluids not balanced on the two sides ($C^* \neq 1$).

Lastly, one of these assumptions of Ch.3 says that the fluids must remain in a single phase throughout the exchanger channels. This means that the fluids must not vary significantly in their own fluid properties along the ducts. When dealing with multi-phase flows, certain sections exhibit differences in the trend of fluid properties, making the process described in this thesis ineffective. Consequently, the current method could be enhanced to work with fluids that undergo a phase change too. A multi-cell heat exchanger sizing approach, which consists of dividing the fluid sides into multiple cells, is recommended for such a task.

The approach developed in this thesis returns valuable results that help the designer in the fin topology selection, with the goal of minimizing the exchanger mass. The design maps obtained with the single objective algorithms must be used to find the optimal fins for an exchanger with both pressure losses constrained. Meanwhile, the NSGA-II returns valuable guidelines for the design of a heat exchanger having a hard constraint on the pressure drop on one side. The performance of the different fin combinations and topologies is well represented and compared. It is important to note that this comparison method should be used for a preliminary heat exchanger design. The design maps also provide information about the exchanger size when the MSP is related to the Bej number, as the flow length has a quadratic influence on the latter. Generally, low Bejan numbers do not necessarily correlate to low pressure drops, but knowing the pressure drop, the Bejan number can be used to estimate the heat exchanger size.

To conclude, the designer can use the optimized design maps to select the optimal fins to obtain the lightest designs at given pressure drops, or the smallest pressure drops at given size constraints. To do so, both design maps correlating the mass-specific power to the Bejan and pressure drops are necessary. The optimized design maps obtained through the NSGA-III, on the other hand, return useful information on how the three performance metrics, namely the mass-specific power and pressure drops, change with respect to one another for each explored heat exchanger topology. These charts can help the designer choose the better topology for a given application, exploring a wide range of pressure drops on both sides.
Taking into account all the recommendations and limitations outlined so far, this approach can still be considered a valid method for a preliminary heat exchanger design.

Bibliography

M.K. Aliabadi, F. Hormozi, and E.H. Rad. New correlations for wavy plate-fin heat exchangers: different working fluids. *International Journal of Numerical Methods for Heat & Fluid Flow © Emerald Group Publishing Limited 0961-5539*, 24:1086–1108, 2014. doi: 10.1108/HFF-09-2012-0195.

F. Ascione, A. Conrozier, and A. Sakly. Aerothermal characterization of a compact heat exchanger elemnt by additive manufacturing. *AerospaceEurope Conference 2020*, 2020.

Ian H. Bell, Jorrit Wronski, Sylvain Quoilin, and Vincent Lemort. Pure and pseudo-pure fluid thermophysical property evaluation and the open-source thermophysical property library coolprop. *Industrial & Engineering Chemistry Research*, 53(6):2498–2508, 2014. doi: 10.1021/ie4033999. URL `http://pubs.acs.org/doi/abs/10.1021/ie4033999`.

Y. Chang and C. Wang. A generalized heat transfer correlation for louver fin geometry. *Int. J. Heat Mass Transfer*, 40:533–544, 1997.

M. Chen, Z. Dong, W. Jia, X. Ni, and H. Yao. Multi-objective joint optimal operation of reservoir system and analysis of objectives competition mechanism: A case study in the upper reach of the yangtze river. *Water*, 2019. doi: 10.3390/w11122542.

S.W. Churchill. Friction factor equation spans all fluid flow regimes. *Chem. Eng.*, 84:91–92, 1977.

K. Deb. A fast and elitist multiobjective genetic algorithm: Nsga-ii. *IEEE TRANSACTIONS ON EVOLUTIONARY COMPUTATION*, 6, 2002.

K. Deb. An evolutionary many-objective optimization algorithm using reference-point-based nondominated sorting approach, part i: Solving problems with box constraints. *IEEE TRANSACTIONS ON EVOLUTIONARY COMPUTATION*, 18, 2014.

Mark A. Digiovanni and Ralph L. Webb. Uncertainty in effectiveness-ntu calculations for crossflow heat exchangers. *Heat Transfer Engineering*, 10(3):61–70, 1989. doi: 10.1080/01457638908939709.

H. Fugmann, E. Laurenz, and L. Schnabel. Multi-dimensional performance evaluation of heat exchanger surface enhancements. *energies*, 2019.

J. García-Castillo and M. Picón-Núñez. Physical dimensions as a design objective in heat transfer equipment: The case of plate and fin heat exchangers. *Energies 2021, 14, 2318. https://doi.org/10.3390/en14082318*, 2021.

Gnielinski. V. g1 heat transfer in pipe flow. in vdi heat atlas, 2nd ed. *Springer: Berlin/Heidelberg*, page pp. 691–700, 2010.

D. Junqi, C. Jiangping, and C. Zhijiu. Heat transfer and pressure drop correlations for the wavy fin and flat tube heat exchangers. *Applied Thermal Engineering 27 (2007) 2066–2073*, 2007.

S. Kakac and H. Liu. Heat exchanger selection rating and thermal design. *CRC Press LLC, Florida*, 2002.

W.M. Kays and A.L. London. *Compact Heat Exchangers.* Medtech a division of Scientific International Pvt. Ltd., 2018.

T.A. Khan and W. Li. Optimal design of plate-fin heat exchanger by combining multi-objective algorithms. *International Journal of Heat and Mass Transfer*, 2017.

P.G. LaHaye, F.J. Neugebauer, and R.K. Sakhuja. A generalized prediction of heat transfer surfaces. *Journal of Heat Transfer*, 1974.

R.M. Manglik and A.E. Bergles. Heat transfer and pressure drop correlations for the rectangular offset strip fin compact heat exchanger. *Experimental Thermal and Fluid Science 1995; 10:171-180 © Elsevier Science Inc., 1995*, 1995.

Brandon Morgan. Towards data science - unit 7) differential evolution — automated machine learning. `https://towardsdatascience.com/unit-7-differential-evolution-automated-machine-learning-eb22014e592e`, 2021.

Y. Park and A. M. Jacobi. Air-side heat transfer and friction correlations for flat-tube louver-fin heat exchangers. *Journal of Heat Transfer, 021801-9*, 131, 2009.

R.K. Shah and D.P. Sekulić. *Fundementals of Heat exchanger design.* John Wiley and sons, inc., 2003.

R.K. Shah and R.L. Webb. *Compact and enhanced heat exchangers, in Heat Exchangers: Theory and Practice,.* Hemisphere Publishing/McGraw-Hill, Washington, DC, 1983.

J.G. Soland. *Performance Ranking of Plate-Finned Heat Exchanger Surfaces.* PhD thesis, MIT, 1975.

K.M. Stone. Review of literature on heat transfer enhancement in compact heat exchangers. Technical report, Air Conditioning and Refrigeration Center, 1996.

A. Triboix. Exact and approximate formulas for cross flow heat exchangers with unmixed fluids. *International Communications in Heat and Mass Transfer*, 2008.

D. Wang, D. Tan, and L. Liu. Particle swarm optimization algorithm: an overview. *Soft Computing*, 2017.

R.L. Webb. Performance evaluation criteria for use of enhanced heat transfer surfaces in heat exchanger design. *Int. Journal of Heat and Mass Transfer*, 1981.

R.L. Webb and N.-H. Kim. Principles of enhanced heat transfer, 2nd ed. *Taylor amp; Francis, New York.*, 2005.

M Yousefi, R. Enayatifar, A.N. Darus, and A.H. Abdullah. Optimization of plate-fin heat exchangers by an improved harmony search algorithm. *Applied Thermal Engineering*, 2012.